This is to certify that the

dissertation entitled

I. DEVELOPMENT OF A MICROWAVE MODULATED INFRARED SIDEBAND LASER IN THE CARBON MONOXIDE LASER REGION

II. LINEAR AND NONLINEAR SPECTROSCOPIC APPLICATIONS OF THE MICROWAVE MODULATED INFRARED SIDEBAND LASER IN THE CO LASER REGION

presented by

SHIN-CHU HSU

has been accepted towards fulfillment
of the requirements for

Ph.D. degree in CHEMISTRY

R. E. Schwendeman
Major professor

Date NOV. 17, 1988

I. DEVELOPMENT OF A MICROWAVE MODULATED INFRARED SIDEBAND LASER IN THE CARBON MONOXIDE LASER REGION

II. LINEAR AND NONLINEAR SPECTROSCOPIC APPLICATIONS OF THE MICROWAVE MODULATED INFRARED SIDEBAND LASER IN THE CO LASER REGION

By

Shin-Chu Hsu

A DISSERTATION

submitted to

Michigan State University

in partial fulfillment of the requirement

for the degree of

DOCTOR OF PHILOSOPHY

Department of Chemistry

1988

ABSTRACT

I. DEVELOPMENT OF A MICROWAVE MODULATED INFRARED SIDEBAND LASER IN THE CARBON MONOXIDE LASER REGION

II. LINEAR AND NONLINEAR SPECTROSCOPIC APPLICATIONS OF THE MICROWAVE MODULATED INFRARED SIDEBAND LASER IN THE CO LASER REGION

By

Shin-Chu Hsu

The method of infrared microwave sideband laser spectroscopy developed by Magerl et al. (IEEE J. Quantum Electron., QE-18, 1214-1220 (1982)) for application in the 9-11 μm region with a CO_2 laser has been extended to applicaiton in the 5-6 μm region with a homebuilt CO gas laser. The theory for the laser sideband generation, crystal modulator design, experimental details, performance of the system, and typical spectra are described. Frequency measurements of spectra in the $01^11 \leftarrow 00^00$ band of N_2O and the $20^00 \leftarrow 00^00$ band of OCS are compared to the results of previous precise measurements by heterodyne techniques to show that the absolute frequency accuracy is limited by the

knowledge of the CO transition frequenies. With the present laser stabilization scheme adopted, the reproducibility is mainly limited by resettability of the CO laser gain curve.

For linear spectroscopic application, this new tunable IR laser system, in traveling wave mode operation, has been employed to measure spectra in the ν_2 band of D_2CO. Approximately 150 transitions with $J \leq 36$ and $K_a \leq 11$ have been assigned. The data have been combined with the frequencies of microwave transitions determined previously for the ground and ν_2 excited vibrational states and then fit to a simple asymmetric rotor Hamiltonian includes quatic and sextic centrifugal distortion coefficients. The frequencies for $K_a < 9$ show noevidence of strong coupling to other bands, but for higher K_a the frequencies of high J transitions show deviations from calculated frequencies that are many times the experimental uncertainties. Improved parameters for the $v_2 = 1$ state are reported.

For nonlinear spectroscopic application, both IR-RF and IR-MW double resonance methods are used to measure the frequencies of asymmetry doublet transitions of H_2CO and D_2CO. Experimental results and Observed frequencies are compared with the prediction of double resonance theory and the best calculated results. The main purpose of this study is to demonstrate that this new tunable laser source has sufficient power, when operated in the resonant cavity mode, to perform saturation spectroscopy.

To Life

ACKNOWLEDGMENTS

I would like to give my full respect and thanks to my adviser, Professor Richard H. Schwendeman. Not only as my advisor, but also like my prarent he kindly tolerated my stubbornness and gave me the freedom to grow up both in academic field and in real life. From him I realize what a scientist should be and what a professor should like.

Deeply from my heart I would like to say thanks to my parents and my girl friend, without their love I won't have the strength to finish this degree.

The financial support of the National Science Foundation is gratefully acknowledged.

Finally, I acknowledge Mr. Martin Rabb, my friends and all the members in this group for the wonderful friendships, because of this, I strongly believe, the world becomes colorful and warm.

TABLE OF CONTENTS

LIST OF TABLES

--- PART I ---

--- PART II ---

TABLE OF FIGURES

-- PART I --

-- PART II --

PART I

DEVELOPMENT OF A MICROWAVE MODULATED INFRARED SIDEBAND LASER IN THE CARBON MONOXIDE LASER REGION

CHAPTER 1

Introduction

The impact of lasers on spectroscopy can hardly be imagined since the introduction of the laser in ~1960. As an intense light source with spectral energy density which exceeds that of incoherent sources by several orders of magnitude and with an extremely small bandwidth, single-mode lasers possess an extremely high sensitivity and spectral resolution which far exceeds that of conventional light sources. Many experiments that could not be done prior to the introduction of lasers because of lack of intensity or insufficient resolution are now readily performed.

In the area of high resolution spectroscopy, how good the laser system you have is just like how well armed you are in the battlefield. After more than two decades' development of various types of laser systems, with varying tunability, spectralpurity, intensity, wavelength measurement, and sensitivity, etc., only a few kinds of laser systems are in widespread use in the IR region.

Laser development in the infrared region began with the advent of a few gas lasers, including the CO_2, N_2O, and CO lasers, covering the 5 to 10 μm region; the HCN, DCN, H_2O, and D_2O lasers in the far infrared; and the He-Ne and He-Xe lasers in the 3 μm region. Most of these lasers are of high gain and deliver very high quality output. However, because

these lasers oscillate in transitions between atomic or molecular levels, the outputs are of fixed frequency. Since the gain profiles of infrared transitions in low pressure gas lasers are essentially determined by Doppler broadening, the continuous tuning range of single-mode lasers is limited to the spectral interval $\delta\nu_D$ within the Doppler width, which amounts to about $\pm$ 0.002 cm^{-1} at ν = 1000 cm^{-1} (λ = 10 μm). In order to have greater tunability, the tuning range of a gas laser may be significantly increased by two methods. The first method uses the Zeeman shift of laser transitions in atoms in an external magnetic field [1] and the second uses the pressure broadening effect to increase the pressure-broadened linewidth by having a large pressure. The first type is called the Zeeman-tuned gas laser and the second is called the waveguide laser [2]. Although both methods can achieve a substantial tunable region, it is necessary to compromise with the difficulty of identifying the absolute wavelength. Therefore, their applications to molecular spectroscopy are still somewhat limited in number.

Alternatively, the tunability of a gas laser for spectroscopic purposes could be achieved by applying either an electric or magnetic field to tune the molecular transition to meet the fixed laser frequency. When an eletric field is employed, the method is referred to as laser Stark spectroscopy, whereas in the magnetic field

case, it is called laser magnetic resonance spectroscopy (LMR). These two methods have been very widely used. A comparison of infrared spectroscopic methods in the IR region given by Hirota in 1985 [3] is shown in Table I. The most commonly used spectroscopic measurements are listed. In addition to laser Stark spectroscopy and LMR, the other tunable laser systems, the diode laser, the color center laser, and the difference frequency laser, are characterized. The main concern in this dissertation is in the region of 900 to 2000 cm^{-1}, which is covered by laser Stark, LMR, and the diode laser. From Table I we see that the advantage of the diode laser is the wide tunability, whereas the disadvantages are the shortage of power, which is seldom sufficient for saturation spectroscopy [4], the need for a reference molecule for the wavelength measurement, and relatively low spectropurity (~10 MHz).

The advantages of the laser Stark and laser magnetic resonance methods are that they have sufficient power to do saturation spectroscopy and it is not necessary to calibrate the spectrometer for wavelength measurement. The disadvantages of laser Stark and LMR spectroscopy are, first of all, that there are limits to the strength of an external field that can be applied to the system, which limit the tunability; and second, that the Stark or Zeeman spectra are so complex that usually only low J transitions can be resolved and even then the field effects must be analyzed to

Table I.

Comparison of Infrared Spectroscopic Methods

	IR-MW Sideband	CO_2,N_2O,CO (Stark, LMR)	Diode	Color Center	Difference Frequency
WAVELENGTH (cm^{-1})	900~2000	900~2000	380~3500	3200~4550	2380~4550
SOURCE	Tunable	Fixed	Tunable	Tunable	Tunable
WAVELENGTH MEASUREMENT	Unnecess.	Unnecess.	Necessary	Necessary	Necessary
SCANNING	Microwave	External field	Current, Temperature	Etalon	Etalon (dye laser)
POWER	100 μW~2 mW	1 mW~1 W	0.1 mW	3~30 mW	1~20 μW
SATURATION	Possible	Possible	Difficult	Possible	Impossible
SENSITIVITY[a]	10^8~10^{10}	10^8	10^8~10^{10}	10^9~10^{11}	10^9~10^{11}

a. Minimum detectable number of molecules in 1 cm^3.

obtain the zero field frequencies.

In the same IR region, in addition to the techniques just mentioned, we have to recognize the recent remarkable progress that has been made in Fourier transform (FT) spectroscopy [5]. As a representative of the IR laser spectroscopic methods, diode laser spectroscopy is compared with FT spectroscopy in Table II. As it is shown, diode laser spectroscopy is more sensitive than FT spectroscopy because the brightness of the former source is much greater than that of the latter. The largest advantage of FT spectroscopy lies in the wide wavelength coverage, but it is attainable with a lower resolution; although the precision of the wavenumber measurement of each absorption or emission line has been much improved by use of a He-Ne laser as a reference, reference molecules are still necessary. On the other hand, in addition to much higher sensitivity, it is easy to introduce several modulation schemes in diode laser spectroscopy that are routine in microwave or radiofrequency spectroscopy. Real time observation of absorption spectra is another advantage of diode laser spectroscoy, which makes it possible to apply this method to a number of monitoring purposes.

The microwave modulated infrared laser sideband system is also characterized in Table II. This system has many of the advantages of the diode laser, laser Stark, and laser magnetic resonance methods and relatively few disadvantages.

Table II.

Comparison of IR-MW Sideband Laser, IR Diode Laser and FTIR

	IR-MW Sideband Laser	IR Diode Laser	Fourier Transform Spec.
SENSITIVITY	High	High	Low
WAVELENGTH COVERAGE	Narrow	Narrow	Wide
MODULATION	Possible	Possible	Difficult
RECORDING	Real time	Real time	Fourier Transform
RESOLUTION	10^{-6} cm^{-1}	10^{-6} cm^{-1}	10^{-3} cm^{-1}
STABILITY	~100 kHz[a]	< 10 MHz	----

a. Stability depends on the stability of the infrared gas laser.

It has the absolute frequency of a gas laser (no need for a reference molecule), moderate tunability (8-18 GHz on both sides of each gas laser line); spectropurity better than 100 kHz (for the CO_2 laser system), moderate power (a few mW) when operated in the cavity mode, sufficient to do saturation spectroscopy with sub-Doppler resolution; and real time recording with various kinds of modulation schemes.

The first spectroscopic application of tunable laser sideband radiation was made by Corcoran et al. in 1973 [6] to measure CO_2 gain profiles by using a GaAs single crystal loaded inside the waveguide as a modulator. Since that time the tunability and the conversion efficiency of CO_2 laser sidebands have been developed for the purpose of molecular spectroscopy. In 1982 this technique was revised by Magerl et al. at the Technical University of Vienna [7] to the present convenient level for spectroscopy. In recent years it has been used in both conventional spectroscopy [8 - 10] and in nonlinear spectroscopy, such as Lamb dip measurements [11 - 13] and infrared radio frequency double resonance measurements [14,15].

For infrared microwave sideband laser spectroscopy a CdTe electrooptic crystal mounted in a matched waveguide microwave circuit is simultaneouly irradiated by an infrared laser at frequency ν_ℓ and high-power microwaves at frequency ν_m. Infrared microwave sidebands at frequencies $\nu_\ell \pm \nu_m$ are

generated by the frequency modulation in the crystal [Figure 1]. After partial separation of the infrared carrier by means of a polarizer, the sidebands are used for conventional linear or non-linear spectroscopy. Because of the velocity matching required in the microwave circuit, individual applications of the sideband technique are limited to spectroscopy in windows that are the width of a matched microwave circuit on either side of each of the possible infrared laser frequencies. In our laboratory, the microwave tunable range is from 8 to 18 GHz.

Until now, all the applications of this technique were carried out in the 9-11 μm region with a CO_2 gas laser as the infrared laser source. By using various possible isotopic species of CO_2 as the lasing medium, most of the 9-11 μm band can be covered. Since this technique has shown its widespread usefulness, we decided to try to extend it to the 5-6 μm region with a home-built CO semisealed gas laser. This extension turned out to be relatively straightforward. Since CdTe has essentially the same optical characteristics, including transmission and index of refraction, in both CO laser and CO_2 laser regions [16], and the microwave circuit and mounting is independent of the laser frequency, it was only necessary to use an anti-reflection coating on the crystal that is satisfactory for the 5-6 μm region and to assemble a CO semisealed gas laser. Although a typical grating-controlled CO laser operates at lower power than a

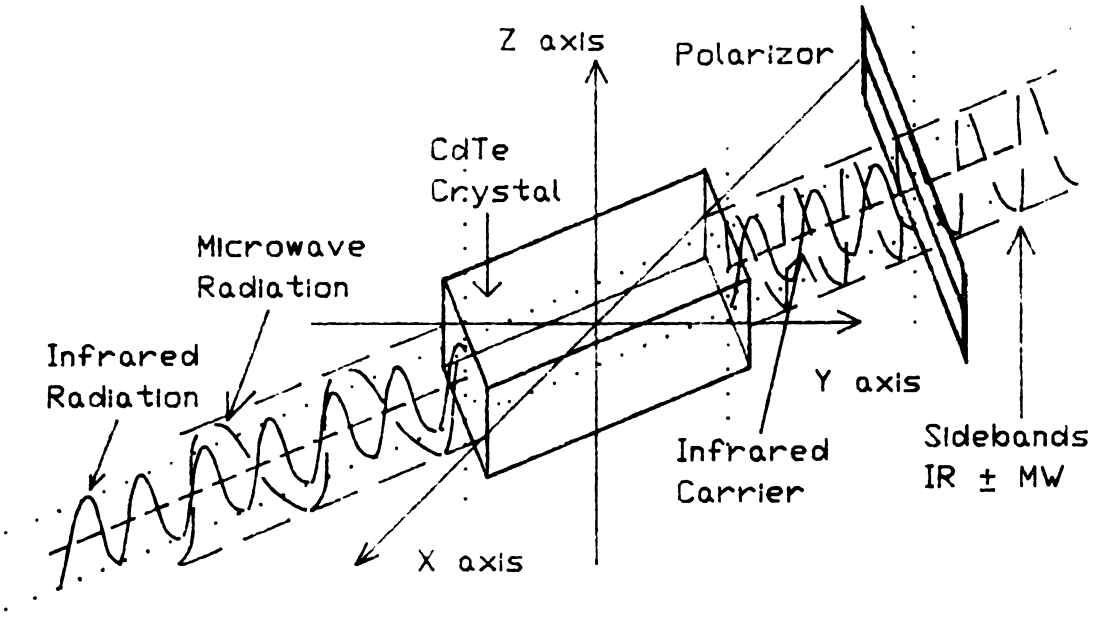

Figure 1. An electric field diagram showing the relationship between polarizations of incoming infrared and microwave radiations and the polarization of outgoing laser sidebands generated by the crystal modulator.

CO_2 laser, the infrared power required for a usable sideband signal is not large and the efficiency of sideband generation increases with the square of the optical frequency, so that it is roughly a factor of four larger in the CO laser region than in the CO_2 laser region [7]. Furthermore, CO lasers have been made to operate at lower frequencies than our laser, so that with a change in laser design, it should be possible to extend the wavelength coverage to well beyond 6 μm.

For demonstration and testing purposes for the new sideband system, we first chose known spectra in the $01^11 \leftarrow 00^00$ combination band of N_2O and $20^00 \leftarrow 00^00$ overtone band of OCS. In the subsequent chapters theory of laser sideband generation, crystal modulator design, and the experimental apparatus will be described and the frequencies measured from experimental spectra will be compared to precise frequencies measured by a beat-frequency technique based on CO_2 laser frequencies. It will be seen that the frequency accuracy, even for the Doppler limited spectra reported here, is primarily dependent on the resettability of the CO laser frequency.

CHAPTER 2

Theory of Laser Sideband Generation and the Design of the CdTe Modulator

In this chapter, the basic theory of the electrooptical phase modulation effect will be described to explain how the laser sidebands are generated and how the design parameters of the CdTe modulator are chosen for optimization of the sideband laser power. Finally, the experimental adjustment of the modulator to obtain the best coupling effect for both traveling wave and cavity mode operations will be discussed and the sideband laser power of this crystal will be estimated.

2.1 Theory of Electrooptic Phase Modulation

The basic idea of sideband laser generation is to utilize the electrooptical property of the CdTe crystal. The applied microwave radiation acts as a modulating electric field which causes the isotropic CdTe crystal to show a birefringent property. The crystal is cut and oriented such that given a selected propagating direction and an electric polarization direction of the incident infrared radiation, after phase modulation and polarization discrimination, only the $\nu_\ell \pm \nu_m$ sidebands [17] can pass through a polarizer that is oriented perpendicular to the

polarization plane of the incoming infrared radiation. The details are discussed below.

2.1.1 Wave Propagation in a Crystal

The distinguishing basic feature of the crystalline state, as far as optical properties are concerned, is the fact that crystals are generally electrically anisotropic. A simple classical picture to explain this anisotropic property [18] is that a bound electron in the crystal acts just like it is attracted to a set of fictitious elastic springs [Figure 2].

The springs have different stiffnesses for different directions of the electron's displacement from its equilibrium position within the crystal lattice. Consequentely, the polarization produced in the crystal by a given electric field is not just a simple scalar constant times the field, but varies in a manner that depends on the direction of the applied field relative to the crystal lattice. It can be shown that

$$\begin{bmatrix} P_1 \\ P_2 \\ P_3 \end{bmatrix} = \varepsilon_o \begin{bmatrix} \chi_{11} & \chi_{12} & \chi_{13} \\ \chi_{21} & \chi_{22} & \chi_{23} \\ \chi_{31} & \chi_{32} & \chi_{33} \end{bmatrix} \begin{bmatrix} E_1 \\ E_2 \\ E_3 \end{bmatrix}$$

where P_i ($i = 1, 2, 3$) is the electric field induced

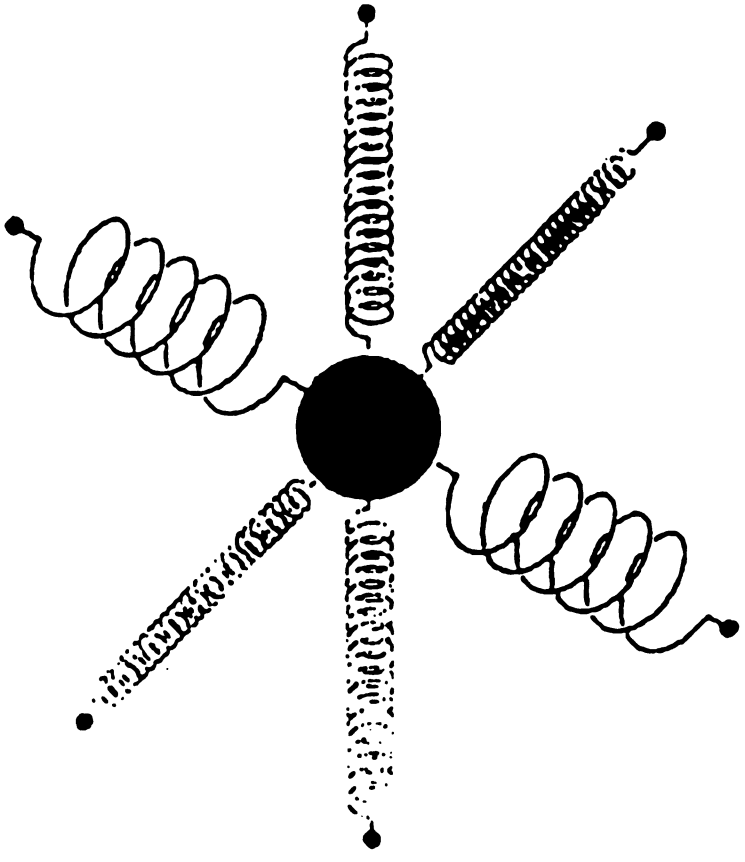

Figure 2. A classical modal to show anisotropic binding of an electron in a crystal. This diagram is from Ref. 18.

polarization, ε_o is the electric permittivity, χ_{ij} (i,j = 1, 2, 3) is an element of the susceptibility tensor, and E_i is the component of the electric field of the incoming radiation in the i^{th} direction.

For ordinary nonabsorbing crystals, the χ tensor is symmetric, so there always exists a set of coordinate axes, called principal axes, such that the χ tensor is diagonal,

$$\chi = \begin{bmatrix} \chi_{11} & 0 & 0 \\ 0 & \chi_{22} & 0 \\ 0 & 0 & \chi_{33} \end{bmatrix} .$$

If $\chi_{11} = \chi_{22} = \chi_{33} = a$, the crystal is isotropic and the index of refraction $n = \sqrt{1 + a}$. If $\chi_{11} = \chi_{22} = a$ and $\chi_{33} = b$, then there are two possible principal indices, $n_o = \sqrt{1 + a}$, and $n_e = \sqrt{1 + b}$; the crystal is said to be uniaxial. If $\chi_{11} = a$, $\chi_{22} = b$, and $\chi_{33} = c$, then $n_1 = \sqrt{1 + a}$, $n_2 = \sqrt{1 + b}$ and $n_3 = \sqrt{1 + c}$ and the crystal is biaxial.

One of the consequences of the anisotropic property is that the speed of propagation of a light wave in a crystal is a function of the direction of propagation and the polarization of the light. It turns out that there are often two possible values of the phase velocity for a given direction of propagation. These two values are associated with mutually orthogonal polarizations of the light waves. Such crystals are said to be doubly refracting or

birefringent [18].

Once the propagating direction for a wave in an anisotropic crystal is given, there will be two different phase velocities associated with each direction of polarization. There is a convenient way to determine the relation between phase velocity and polarization by using the so-called index ellipsoid:

$$\frac{x^2}{n_x^2} + \frac{y^2}{n_y^2} + \frac{z^2}{n_z^2} = 1 \quad ;$$

$$n_x^2 = \frac{\varepsilon_{xx}}{\varepsilon_o} \quad , \quad n_y^2 = \frac{\varepsilon_{yy}}{\varepsilon_o} \quad , \quad n_z^2 = \frac{\varepsilon_{zz}}{\varepsilon_o} \quad .$$

This is the equation of a general ellipsoid with principal axes parallel to the x, y, z principal axis directions, whose respective lengths are $2n_x$, $2n_y$, $2n_z$. The index ellipsoid is used mainly to determine the two indices of refraction and the two corresponding directions of electric displacement associated with the two independent plane waves that can propagate along an arbitrary direction $\hat{s}$ in a crystal. This can be done by means of following procedure [Figure 3].

Begin by finding the intersection ellipse between the index ellipsoid and a plane through the origin that is normal to the direction of propagation. Then, the two axes of the intersection ellipse are equal in length to $2n_1$ and $2n_2$ where n_1 and n_2 are the two indices of refraction.

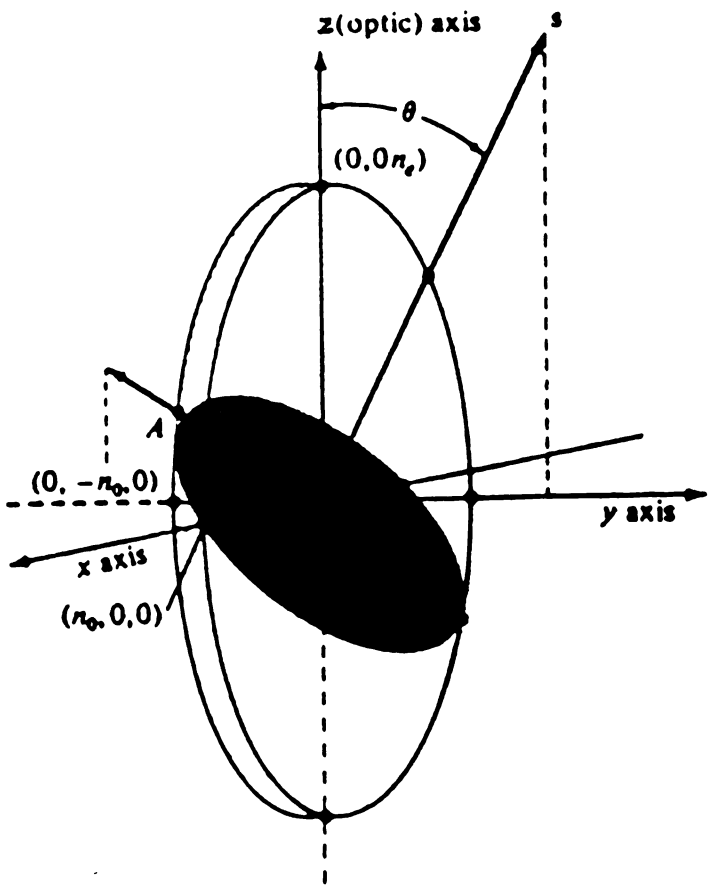

Figure 3. Construction for finding indices of refraction and allowed polarization for a given direction of propagation $\hat{s}$. The figure shown is for a uniaxial crystal with $n_x = n_y = n_o$. This diagram is from Ref. 20.

These axes are parallel to the direction of the D_{ii} vectors of the allowed solutions [19].

2.1.2 Electrooptic Effect

The index ellipsoid describes the anisotropic property (susceptibity tensor) of the crystal. If we place a certain kind of crystal in an electric field, it is possible to effect changes in the indices of refraction that are proportional to the field. These are referred to electrooptic effects.

For arbitrary coordinates x, y, z in a crystal, the index ellipsoid equation can be written as

$$\left[\frac{1}{n^2}\right]_1 x^2 + \left[\frac{1}{n^2}\right]_2 y^2 + \left[\frac{1}{n^2}\right]_3 z^2 + 2\left[\frac{1}{n^2}\right]_4 yz + 2\left[\frac{1}{n^2}\right]_5 xz + 2\left[\frac{1}{n^2}\right]_6 xy = 1 \quad .$$

We have used the convention, 1 = xx, 2 = yy, 3 = zz, 4 = yz, 5 = xz, 6 = xy, associated with the chosen coordinate system. If we choose x, y, and z to be x', y', z' which are parallel to the principal dielectric axes of the crystal, then with zero applied electric field, the above equation must reduce to

$$\left[\frac{1}{n^2}\right]_1 x'^2 + \left[\frac{1}{n^2}\right]_2 y'^2 + \left[\frac{1}{n^2}\right]_3 z'^2 = 1 \quad .$$

If we apply an electric field E in a arbitrary direction, then $E = (E_x, E_y, E_z)$ and the change in the coefficient $\left[\frac{1}{n^2} \right]_i$, $i = 1, 2, \ldots, 6$ will be given by $\Delta \left[\frac{1}{n^2} \right]_i = \sum_{j=1}^{3} r_{ij} E_j$ or in matrix language,

$$\begin{vmatrix} \Delta \left(\frac{1}{n^2}\right)_1 \\ \Delta \left(\frac{1}{n^2}\right)_2 \\ \Delta \left(\frac{1}{n^2}\right)_3 \\ \Delta \left(\frac{1}{n^2}\right)_4 \\ \Delta \left(\frac{1}{n^2}\right)_5 \\ \Delta \left(\frac{1}{n^2}\right)_6 \end{vmatrix} = \begin{vmatrix} r_{11} & r_{12} & r_{13} \\ r_{21} & r_{22} & r_{23} \\ r_{31} & r_{32} & r_{33} \\ r_{41} & r_{42} & r_{43} \\ r_{51} & r_{52} & r_{53} \\ r_{61} & r_{62} & r_{63} \end{vmatrix} \begin{vmatrix} E_1 \\ E_2 \\ E_3 \end{vmatrix} .$$

The 6 x 3 matrix with elements r_{ij} is called the electrooptic tensor. For the cubic crystal CdTe, the electrooptic tensor is as follows:

$$r_{ij} = \begin{vmatrix} 0 & 0 & 0 \\ 0 & 0 & 0 \\ 0 & 0 & 0 \\ r_{41} & 0 & 0 \\ 0 & r_{52} & 0 \\ 0 & 0 & r_{63} \end{vmatrix} \qquad i = 1,2,\ldots 6 \quad j = 1,2,3$$

$r_{41} = r_{52} = r_{63} = a$ [20].

In general, the principal axes of the ellipsoid in the presence of the field do not coicide with (x', y', z'); we thus need to find the direction and magnitude of the new principal axes. The procedure is the familiar one of principal axis transformation of quadratic forms.

Since CdTe is an isotropic cubic crystal, when there is no applied electric field and x', y', z' are the principal axes of the crystal, then $n_1 = n_2 = n_3 = n_o$ and

$$\frac{1}{n_o^2} x'^2 + \frac{1}{n_o^2} y'^2 + \frac{1}{n_o^2} z'^2 = 1 \quad .$$

If the electric field is applied along the (1,1,0) direction, then $\hat{E}_m = (\frac{1}{\sqrt{2}} E_m , \frac{1}{\sqrt{2}} E_m , 0)$ and

$$\frac{1}{n_o^2} x'^2 + \frac{1}{n_o^2} y'^2 + \frac{1}{n_o^2} z'^2 + \sqrt{2}\, r_{41} E_m (y'z' + z'x') = 1 \; .$$

In matrix language, in the presence of the electric field $\hat{E}_m$ the index ellipsoid is

$$\begin{vmatrix} \frac{1}{n_o^2} & 0 & \frac{aE_m}{\sqrt{2}} \\ 0 & \frac{1}{n_o^2} & \frac{aE_m}{\sqrt{2}} \\ \frac{aE_m}{\sqrt{2}} & \frac{aE_m}{\sqrt{2}} & \frac{1}{n_o^2} \end{vmatrix} \; .$$

After diagonalization, this is

$$\begin{vmatrix} \frac{1}{n_o^2} - aE_m & 0 & 0 \\ 0 & \frac{1}{n_o^2} + aE_m & 0 \\ 0 & 0 & \frac{1}{n_o^2} \end{vmatrix} ,$$

and the diagonalizing transformation matrix is

$$\begin{vmatrix} \frac{1}{2} & \frac{1}{2} & \frac{1}{\sqrt{2}} \\ \frac{1}{2} & \frac{1}{2} & -\frac{1}{\sqrt{2}} \\ -\frac{1}{\sqrt{2}} & \frac{1}{\sqrt{2}} & 0 \end{vmatrix} .$$

Therefore, the new axes x", y", z" are [Figure 4]

$$z" = \frac{1}{\sqrt{2}} (x' - y') ,$$

$$x" = \frac{1}{2} (x' + y') - \frac{1}{\sqrt{2}} z' ,$$

$$y" = \frac{1}{2} (x' + y') + \frac{1}{\sqrt{2}} z' ,$$

and the new index ellipsoid [21] is

$$(\frac{1}{n_o^2} - r_{41}E_m) x"^2 + (\frac{1}{n_o^2} + r_{41}E_m) y"^2 + \frac{1}{n_o^2} z"^2 = 1 .$$

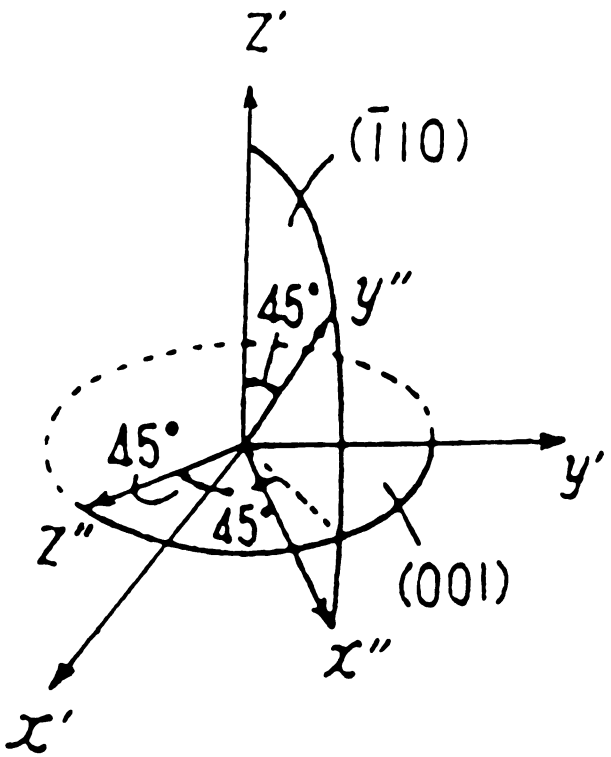

Figure 4. Electro-optical properties of the CdTe crystal. The applied electric field $\hat{E}_m$, E_x, = E_y, = $E_m/\sqrt{2}$, E_z, = 0. The new principal axes are x", y", z". This diagram is from Ref. 21.

Apparently, $\frac{1}{n_{x''}^2} = \frac{1}{n_o^2} - r_{41}E_m$,

$$\frac{1}{n_{y''}^2} = \frac{1}{n_o^2} + r_{41}E_m \text{ , and } \frac{1}{n_{z''}^2} = \frac{1}{n_o^2} \text{ .}$$

Since for CdTe, $r_{41} \approx 10^{-12}$ m/V and $n_o \approx 2.6$, $r_{41}E_m << n_o^{-2}$ for practical E_m. Therefore, to high approximation

$$n_{x''} = n_o + \frac{n_o^3}{2} r_{41}E_m \text{ ,}$$

$$n_{y''} = n_o - \frac{n_o^3}{2} r_{41}E_m, \quad \text{and} \quad n_{z''} = n_o \text{ .} \qquad [\ 21\ ]$$

If the incoming laser radiation is traveling in the + z" direction with its electric field parallel to the z' axis, then the $\hat{E}_\ell$ in the x', y', z' frame has components $\hat{E}_\ell = (\ 0,\ 0,\ E_\ell\ )$. In the x", y", z" frame the vector $\hat{E}_\ell = (\ E_{x''},\ E_{y''},\ 0\ )$. At the output of the crystal (z" = L),

$$E_{x''} = \frac{-1}{\sqrt{2}} E_\ell \cos\left(\omega t - \left(\frac{\omega}{c}\right) \left[n_o + \left(\frac{n_o^3}{2} \right) r_{41}E_m\right] L \right) \text{ ,}$$

and

$$E_{y''} = \frac{1}{\sqrt{2}} E_\ell \cos\left(\omega t - \left(\frac{\omega}{c}\right) \left[n_o - \left(\frac{n_o^3}{2} \right) r_{41}E_m\right] L \right) \text{ .}$$

The phase difference at the output plane z" = L between the two components is called the single pass retardation

$$\Gamma = \phi_{x''} - \phi_{y''} = \frac{\omega}{c} n_o^3 r_{41} E_m L \quad .$$

In this case in which the applied electric field E_m is perpendicular to the propagating direction of E_ℓ, the effect is called the "transverse electrooptic effect". If E_m is a constant, we find that the phase velocity is different for the two orthogonal planes of polarization; except when $\Gamma = n \times \pi$, this will lead to a radiation with a slowly rotating plane of polarization in the output surface ($z'' = L$).

2.1.3 Phase Modulation

If the electric field E_m in the previous section is a sine function instead of a constant, then for $E_m = E_m \sin(\omega_m t)$, we have

$$E_{x''} = \frac{-1}{\sqrt{2}} E_\ell \cos(\omega t - (\frac{\omega}{c})[n_o + (\frac{n_o^3}{2}) r_{41} E_m \sin(\omega_m t)] L) \quad ,$$

and

$$E_{y''} = \frac{1}{\sqrt{2}} E_\ell \cos(\omega t - (\frac{\omega}{c})[n_o - (\frac{n_o^3}{2}) r_{41} E_m \sin(\omega_m t)] L) \quad .$$

Since both equations have the same phase constant $(\frac{\omega}{c})n_o L$, we can drop it without any trouble. Then,

$$E_{x''} = \frac{-1}{\sqrt{2}} E_\ell \cos(\omega t - \delta \sin(\omega_m t)) \quad , \quad \text{and}$$

$$E_{y''} = \frac{1}{\sqrt{2}} E_\ell \cos(\omega t + \delta \sin(\omega_m t)) \quad ,$$

where

$$\delta = \frac{\omega}{c} \frac{n_o^3}{2} r_{41} E_m L = \frac{\pi n_o^3 r_{41} E_m L}{\lambda} = \frac{1}{2} \Gamma \quad .$$

In this case $\delta << 1$, so we can write

$$\cos(\omega t - \delta \sin\omega_m t) = \cos\omega t \cos(\delta \sin\omega_m t) + \sin\omega t (\delta \sin\omega_m t)$$

$$\cong \cos\omega t + \delta \sin\omega t \sin\omega_m t$$

$$= \cos\omega t + \frac{\delta}{2}[\cos(\omega-\omega_m)t - \cos(\omega+\omega_m)t] \quad .$$

Similarly,

$$\cos(\omega t + \delta \sin\omega_m t) \cong \cos\omega t - \frac{\delta}{2}[\cos(\omega-\omega_m)t - \cos(\omega+\omega_m)t] \quad .$$

Therefore, the components of the laser radiation leaving the crystal modulator are

$$E_{x''} = \frac{-1}{\sqrt{2}} E_\ell \{ \cos(\omega t) + \frac{\delta}{2} [\cos(\omega-\omega_m)t - \cos(\omega+\omega_m)t]\} \quad ,$$

$$E_{y''} = \frac{1}{\sqrt{2}} E_\ell \{ \cos(\omega t) - \frac{\delta}{2} [\cos(\omega-\omega_m)t - \cos(\omega+\omega_m)t]\} \quad .$$

Each component consists of a carrier wave at angular frequency ω and sidebands at angular frequency $\omega - \omega_m$ and $\omega + \omega_m$. The outgoing radiation

$$\hat{E}_\ell = \hat{E}_{x''} + \hat{E}_{y''} = E_\ell \cos(\omega t)\left(\frac{-1}{\sqrt{2}}\hat{x}'' + \frac{1}{\sqrt{2}}\hat{y}''\right)$$

$$- \frac{\delta}{2} E_\ell \cos(\omega-\omega_m)\left(\frac{1}{\sqrt{2}}\hat{x}'' + \frac{1}{\sqrt{2}}\hat{y}''\right)$$

$$+ \frac{\delta}{2} E_\ell \cos(\omega-\omega_m)\left(\frac{1}{\sqrt{2}}\hat{x}'' + \frac{1}{\sqrt{2}}\hat{y}''\right)$$

$$= E_\ell \cos(\omega t)\,\hat{z}'$$

$$- \frac{\delta}{2} E_\ell \cos(\omega-\omega_m)\left(\frac{1}{\sqrt{2}}\hat{x}' + \frac{1}{\sqrt{2}}\hat{y}'\right)$$

$$+ \frac{\delta}{2} E_\ell \cos(\omega-\omega_m)\left(\frac{1}{\sqrt{2}}\hat{x}' + \frac{1}{\sqrt{2}}\hat{y}'\right) .$$

The laser carrier is still polarized in the z',z" plane traveling in the z" direction, whereas the sidebands are polarized in the $\hat{E}_m$, z" plane, perpendicular to the plane of the laser carrier. The fact that the planes of polarization of sidebands and carrier are perpendicular to each other allows the partial separation of carrier from sidebands by means of a polarizer. The ratio of the amplitude of each sideband to that of the carrier is given by $\delta/2$, which is estimated in the next section.

2.2 Electrooptic Modulator Design

The electrooptic modulator used in the work described in this dissertation was designed by Gottfield Magerl,

following the principles given in Ref. 7, and will be described below. The modulator is a CdTe crystal cut for optimum transverse amplitude modulation. For incident laser carrier power P_ℓ, one of the positive or negative sidebands contains a power of approximately [22,23]

$$P_{SB} = P_\ell \Gamma^2/16 \quad , \qquad (1)$$

where the single-pass retardation Γ induced by the transverse electrooptic effect can be written as

$$\Gamma = (2\pi/\lambda_\ell) n_o^3 r_{41} E_m L \, \mathrm{sinc}(\omega_m L/2w) \quad . \qquad (2)$$

In the equation above λ_ℓ is the free-space wavelength of the infrared laser, E_m denotes the peak microwave electric field strength within the modulator crystal, n_o is the refractive index, r_{41} is the electrooptic coefficient, and L is the length of the modulator crystal. The abbreviation sinc(x) is used for (sinx)/x, ω_m stands for the angular frequency of the modulating signal, and 1/w characterizes the mismatch of microwave phase velocity (v_m) and of laser group velocity (v_ℓ) within the modulator;

$$\frac{1}{w} = \frac{1}{v_m} - \frac{1}{v_\ell} \quad .$$

The difference between the Γ above and the Γ in the previous section is the sinc($\omega_m L/w$), the phase velocity mismatch term. For collinear propagations of three

radiations, infrared $k(\omega_\ell)$, microwave $k(\omega_m)$, and sidebands $k(\omega_\ell \pm \omega_m)$, a phase-match condition can be written as

$$k(\omega_\ell \pm \omega_m) = k(\omega_\ell) \pm k(\omega_m) \quad ,$$

which may be interpreted as momentum conservation for the three photons participating in the mixing process. Since $c/n = \omega/k$, $\omega_s = \omega_\ell \pm \omega_m$, and $\hat{k}_\ell$, $\hat{k}_m$, and $\hat{k}_s$ are collinear, then

$$n_s\omega_s = n_\ell\omega_\ell \pm n_m\omega_m \quad .$$

The microscopic contributions generated by atoms of different positions in the crystal medium can only add up to a macroscopic wave with appreciable intensity if the phase velocity of the incident inducing waves and polarization waves are properly matched [24].

The modulator is designed to obtain appropriate power under considerations of several factors; infrared laser power (P_ℓ), velocity match (1/w), appropriate tunable range (sinc($\omega_m L/w$)), microwave electric field strength (E_m), etc.. These factors are directly related to the crystal surface treatment, the length, width, and height of the crystal, the microwave housing, the waveguide design, etc..

In order to insure the highest possible infrared radiation power with CO_2 as well as CO lasers, the ends of the crystal were given a broad band (5-11 μm)

antireflection coating to avoid loss from the reflection of infrared radiation.

Since the approximate sideband power is proportional to the square of

$$\sin\left(\frac{\omega_m L}{2w}\right) \Big/ \frac{\omega_m L}{2w} \quad , \qquad (3)$$

for optimum electrooptic interaction we have to provide velocity match (1/w = 0) between the infrared and microwave radiations. It turns out that the refractive index of modulator materials such as CdTe in the IR region is appreciably smaller than the square root of the microwave dielectric constant. Therefore, we have to accelerate the microwave signal. The easiest way to do this is to put the modulator crystal inside a closely fitting rectangular waveguide [25]. Velocity match of the IR laser and microwave radiations is achieved at the microwave wavelength λ_o when the broader dimension of the modulator (a_m) satisfies the equation [25],

$$a_m = \frac{\lambda_o}{\sqrt{\varepsilon_{eff} - n_o^2}} \quad . \qquad (4)$$

Here, n_o and ε_{eff} are the refractive index for infrared radiation and the effective dielectric constant for microwaves respectively. The effective dielectric constant

is related to the dielectric constant (ε_r) of the crystalline material by the equation

$$\varepsilon_{eff} = \frac{\varepsilon_r}{1+(\varepsilon_r-1)t/b_m} \quad , \qquad (5)$$

in which b_m is the height of the modulator. This equation takes into account the reduction of the dielectric constant of the modulator at microwave frequencies due to the presence of an unavoidable air gap of thickness t between the top and/or bottom walls of the modulator housing and the crystal [Figure 5]. For our case, the desired center frequency is 13.5 GHz (22 mm) and we chose values of a_m = 8.2 mm and b_m = 3.0 mm. If n_o is taken to be 2.69 at 5 μm, these values are consistent with an effective dielectric constant of 9.04, which leads to a value of 9.55 for the true dielectric constant of CdTe if t is taken to be 0.02 mm. This value of ε_r is within the range of values measured for modulator crystals in Magerl's laboratory in Vienna. Since a wide crystal is expensive, a CdTe crystal with a cross section of 3.1 × 3.0 mm was embedded between two Al_2O_3 slabs of about the same dielectric constant and with dimensions of 2.54 × 3.0 × 30 mm to achieve a width near 8.2 mm and a height of 3.0 mm.

According to Eq. (2), the longer the crystal the more sideband power we should be able to obtain. However, from

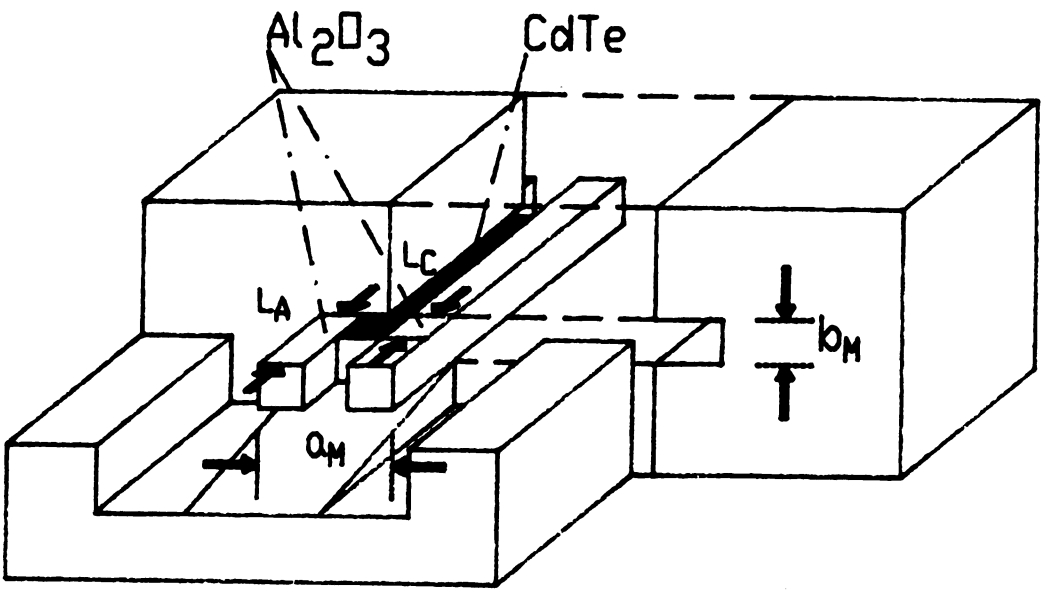

Figure 5. Arrangement of the CdTe crystal and of the Al_2O_3 slabs at the feeder end of the modulator housing. Their relative positions L_C and L_A are given with respect to the front surface of the housing.

Eq. (3), when the modulating frequency differs from the matching frequency f_{mo}, we find that the longer the crystal L, the more the microwave-dispersion-induced velocity mismatch will cost in sideband power. According to Ref. 25, the corresponding 3 dB bandwidth for CdTe can be shown to be approximately 250 GHz/L mm at 13.5 GHz. Therefore, the length L was chosen to be 25.4 mm, aiming at a modulator bandwidth of ≈ 10 GHz.

Since the sideband power is dependent on the square of the microwave electric field strength, for a constant microwave power, the smaller the field dimension, $a_m \times b_m$, the larger E_m. However, the size should be large enough to permit laser-beam focusing through the modulator. This consideration led to the choice of b_m = 3.0 mm and the width of the crystal to be 3.1 mm.

The crystal is enclosed in a 24 mm long brass housing, as shown in Figure 5. In order to obtain impedance match between the modulator and the incoming/outgoing standard rectangular waveguides, tapered double-ridge waveguides, WRD-750, are used in both sides of the crystal housing. Therefore, loss of microwave power, and therefore the sideband power, as a result of reflections can be avoided [7].

2.3 Experimental Adjustment of Modulator for Traveling Wave Mode and Resonant Mode Operations

The modulator can be operated in two modes: the traveling wave mode and the cavity mode. The basic difference between them is the microwave field strength inside the modulator. In the traveling wave mode microwaves are guided through the crystal and then absorbed by a termination. In the resonant mode, a tunable short is used to create a cavity between the entrance of the crystal and the short. In this way a much larger microwave electric field strength is produced, which increases the sideband power.

The electric field strength within the modulator can be determined [26] from microwave power flow in the traveling wave mode and within the cavity. By using Eq. (6) and Eq. (7), the modulator conversion efficiencies, η_{TW} and η_{RES}, are defined as the amount of sideband power generated from 1 W of infrared laser power;

$$\eta_{TW} = \left[\frac{\pi}{\lambda_\ell} n_o^3 r_{41} \right]^2 \mathrm{sinc}^2 \left[\frac{\omega_m L}{2w} \right] \frac{\eta_o P_m L^2}{a_m b_m \sqrt{\varepsilon_r - (\lambda_m / 2a_m)^2}} \quad . \quad (6)$$

In Eq. (6) η_o stands for the intrinsic impedance of free space, P_m is the microwave power traveling through the

modulator, and λ_m is the vacuum wavelength of the microwave signal; the remaining constants have been defined previously. With our crystal we can obtain ~200 μW sideband power from 1 W laser power with 20 W microwave power.

For the resonant mode operation, the conversion efficiency is

$$\eta_{RES} = 2\left[\frac{\pi}{\lambda_\ell} n_o^3 r_{41} \right]^2 \mathrm{sinc}^2\left[\frac{\omega_m L}{2w} \right] \frac{P_m Q_o \beta L}{\left[a_m b_m \varepsilon_o \varepsilon_r \omega_m (1+\beta) \right]^2} \quad .(7)$$

Here Q_o and β are the unloaded Q-factor and the coupling factor, respectively, of the modulator cavity.

Figure 6 shows the experimental setup that was used to adjust the relative positions of the Al_2O_3 slabs and the CdTe crtstal [Figure 5] to couple the microwave radiation into the modulator as well as possible. With a computer controlled Hewlett-Packard HP-8671B microwave source, the microwave frequency was swept from 12.4 - 18.0 GHz. After an initial adjustment of the length of the housing, it was possible, by adjusting the positions of both the modulator crystal and the Al_2O_3 slabs, to put the modulator into either the traveling wave mode or the resonant mode of operation.

Figure 7 shows, for the traveling wave mode operation, the frequency dependence of the input and reflected microwave power for the modulator crystal and Al_2O_3 in their

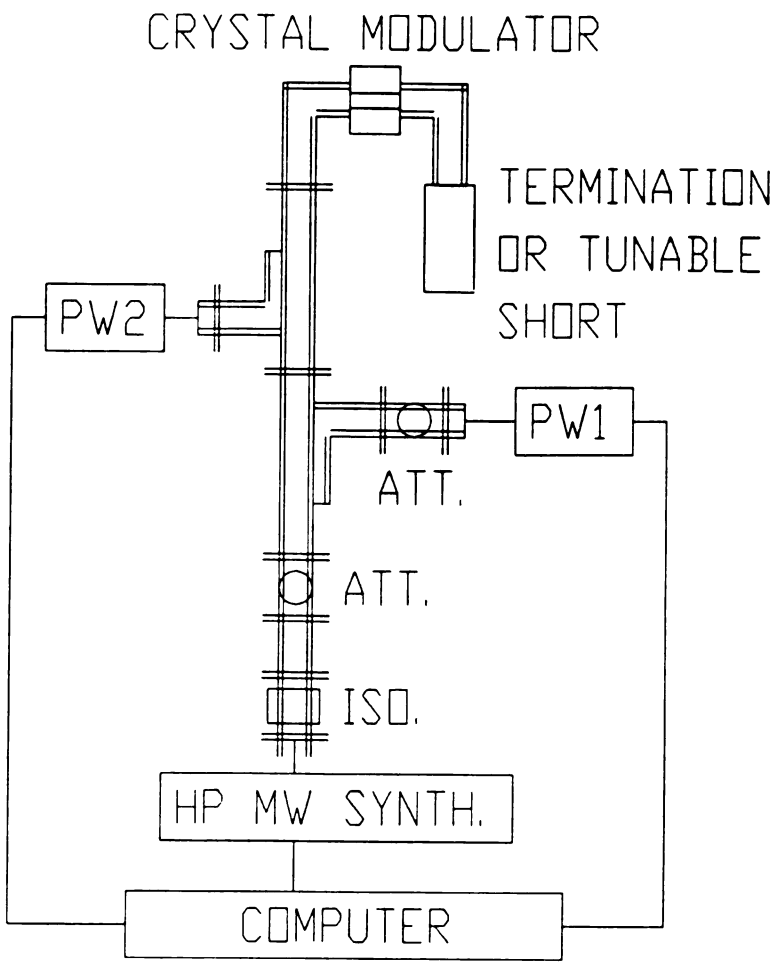

Figure 6. Experimental setup to adjust the relative positions of Al_2O_3 and crystal to the modulator housing to optimize the coupling effect.

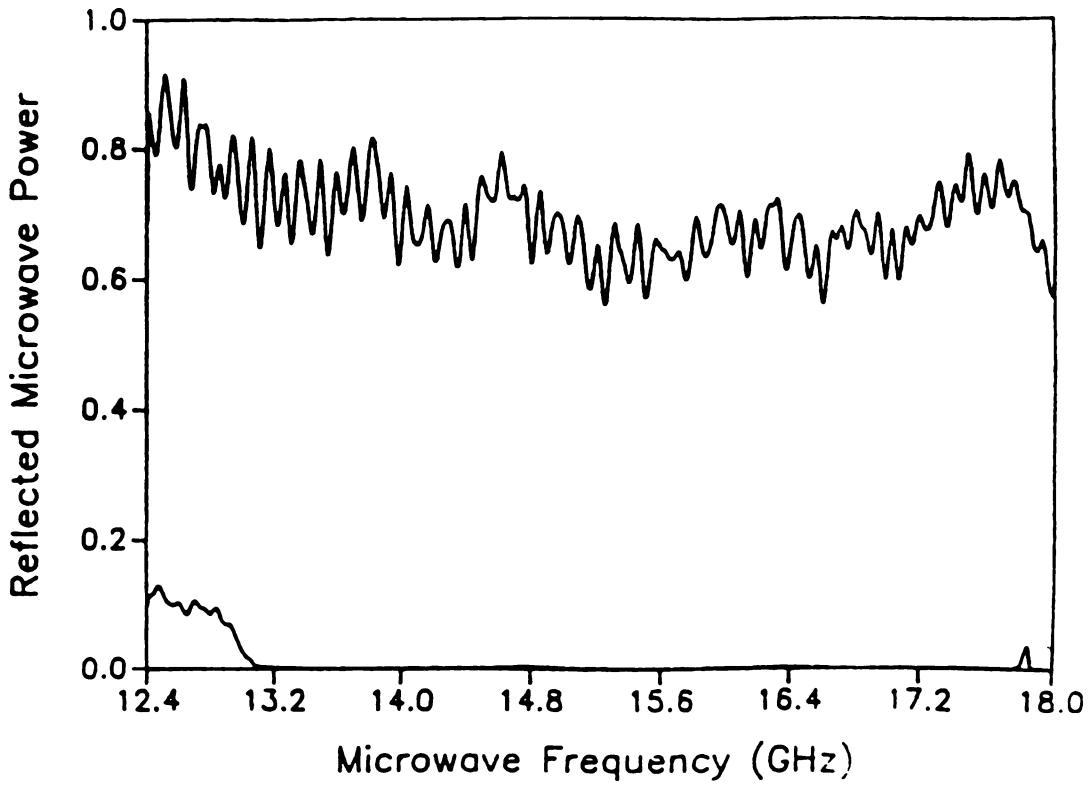

Figure 7. The incoming and reflected microwave power from the modulator in the 12.4 to 18.0 GHz region in traveling mode operation; the upper trace is incoming microwave power and the lower trace is the reflected power: the reflected power is near zero from 13.2 to 17.7 GHz.

optimum positions, as chosen by trial and error. For this plot, L_A = 2.5 mm and L_C = 2.0 mm [Figure 5]. As indicated above, the calculated conversion efficiency of the traveling wave modulator at 13.5 GHz is ~200 μW sideband power per watt of laser power for 20 W input MW power. Figure 8 shows the frequency dependence of the relative sideband power. Except for a dip near 17 GHz, the sideband power vs. frequency is fairly constant.

For the cavity mode of operation, the CdTe crystal and the Al_2O_3 slabs were both pushed back into the housing to a position given by L_C = -4.0 mm and L_A = -3.5 mm [Figure 5]. A double-ridge waveguide at the input and a double-ridged sliding short at the output provided excellent tunability of the cavity resonances. Figure 9 shows the microwave power reflected from the resonant modulator in the 12.4 - 18.0 GHz range and Figure 10 shows a single resonance near 14.8 GHz. With an unloaded Q-factor of Q_o = 840 the conversion efficiency is 2.2 mW sideband power per watt laser power with 20 W microwave drive power. Thus, we are able to achieve, with a single crystal and just one housing, both broadly tunable sideband output with power sufficient for linear spectroscopy and relatively high sideband power within (tunable) resonances suitable for saturation spectroscopy.

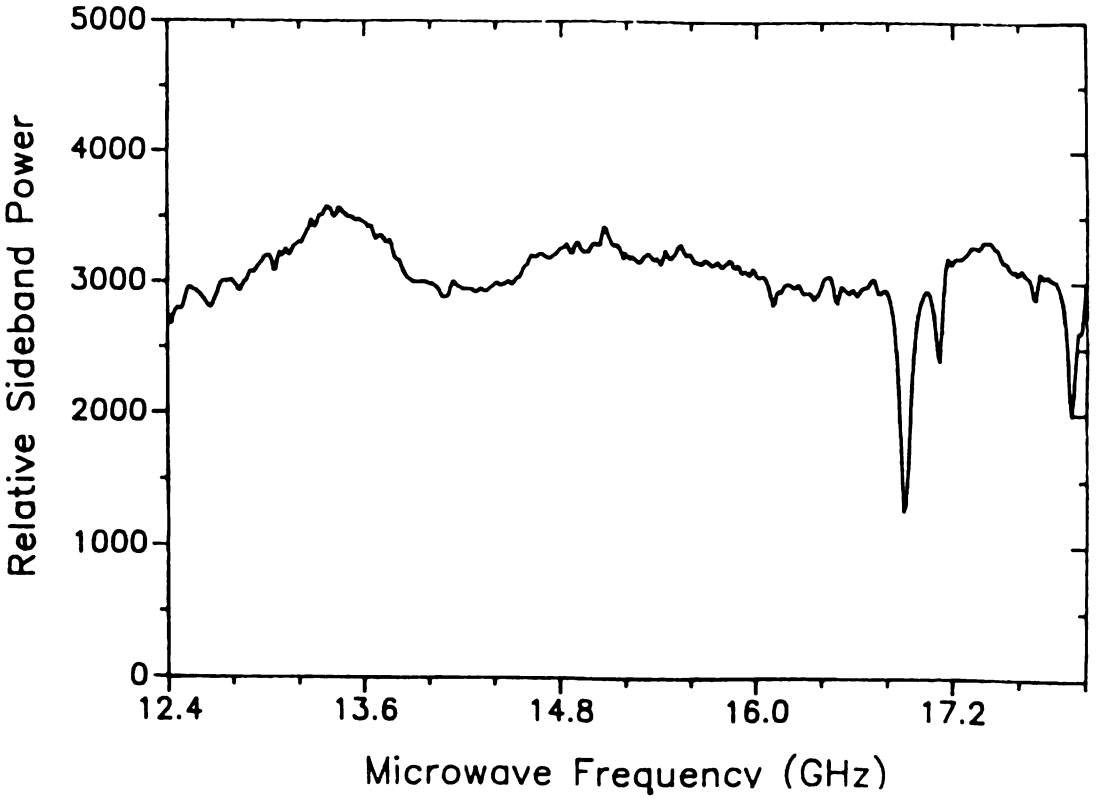

Figure 8. Frequency dependence of the sideband power with a controlled constant microwave power input. Except for a dip near 17 GHz, the sideband conversion efficiency vs. frequency is fairly smooth.

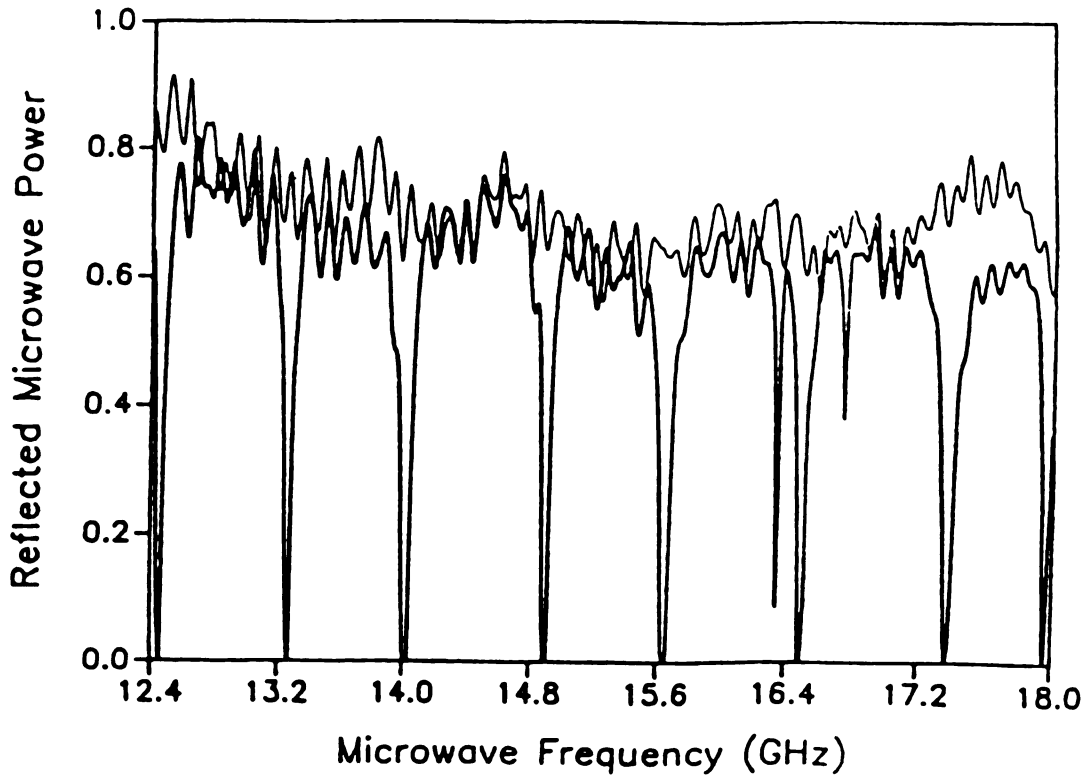

Figure 9. The incoming and reflected microwave power from the modulator between 12.4 and 18.0 GHz in the cavity mode operation. The upper trace is the incoming microwave power and the lower trace is the reflected microwave power.

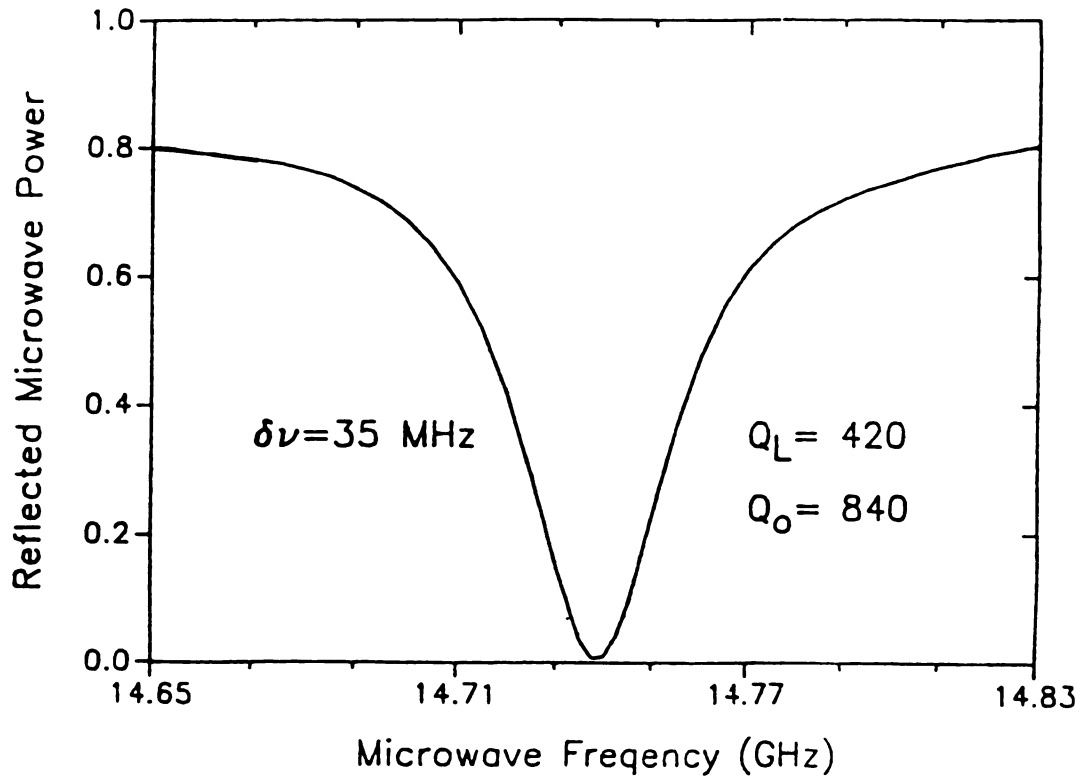

Figure 10. A single resonance near 14.8 Ghz in the cavity mode operation indicating an unloaded Q-factor of Q_o = 840.

CHAPTER 3

Instrumentation

After the discussion of the heart - *i.e.*, the CdTe electrooptic modulator - of the sideband laser in Chapter 2, in this chapter we will talk about the rest of the experimental apparatus including the carbon monoxide semisealed gas laser, the CO sideband laser spectrometer, and the simultaneous microwave switch/power leveling device.

3.1 Carbon Monoxide Semisealed Gas Laser

In 1964 Legay and Lagay-Sommaire [27] first suggested the possibility of laser action in the CO molecule utilizing the vibration-rotation transitions in the electronic ground state of CO. The first experimental observation of laser action on these transitions in CO was made by Patel and Kerl soon afterwards [28]. These workers observed laser oscillations in the wavelength range from 5.0 to 5.4 μm by using a pulsed electric discharge in low pressure CO. Since then, the CO laser has been developed extensively and has attracted considerable interest on account of its high power and efficiency. Output powers in excess of 100 kW and efficiencies in excess of 60% have been demonstrated [29]. However, to achieve this sort of performance the gas mixture must be kept at cryogenic temperature (77 - 100 K, cooled

by liquid nitrogen) and operated as a flowing-gas system. Lasing action in the 5 μm region arises from several P branch vibration-rotation transitions [e.g., from v' = 11 → v'' = 10 to v' = 7 → v'' = 6 at T = 77^{o}K] of the highly vibrationally excited CO molecule [30].

For laser action, the most important requirement is the creation of a population inversion. Pumping of the CO vibrational levels is usually achieved by electron-impact excitation. Like the isoelectronic N_2 molecule, the CO molecule has an unusually large cross section for electron-impact excitation of its vibrational levels. Thus nearly 90% of the electron energy in a discharge can be converted into vibrational energy of CO molecules. Another important feature of the CO molecule is that vibration-vibration relaxation proceeds at a much faster rate than vibration-translation relaxation (which is unusually slow). As a consequence of this feature, a non-Boltzmann population builds up in higher vibrational levels by a process known as "anharmonic pumping",

$$CO\ (v{=}n) + CO\ (v{=}m) \rightarrow CO\ (v{=}n{+}\ell) + CO\ (v{=}m{-}\ell)\ ,$$

which, because of the vibration anharmonicity, is favored when $n > m$ [31]. This process allows CO molecules to climb up the ladder of the vibrational levels with resulting non-Boltzmann distribution of the population among these

levels.

Although anharmonic pumping does not lead to total inversion in the vibrational populations of CO, a situation known as "partial inversion" occurs. This is illustrated in Figure 11 in which it is seen that although the populations for two neighboring vibrational states is equal, an inversion exists in the two P-branch transitions [(j'=5) → (j=6), (j'=4) → (j=5)] and two R-branch transitions indicated in the figure. Under conditions of partial inversion, laser action can thus take place and a new phenomenon, called cascading, plays an important role. The laser action depopulates a rotational level of the upper state and populates a rotational level of the lower vibrational state. The latter level can then accumulate enough population to result in population inversion with a rotational level of a still lower vibrational state. At the same time, the rotational level of the upper state may become sufficiently depopulated to result in population inversion with a rotational level of a still higher vibrational state. This process of cascading coupled with the very low V-T rate results in most of the vibrational energy being extracted as laser output energy with a multiline operation. This, together with the very high excitation efficiency, accounts for the high efficiency of the CO laser. The low-temperature requirement arises from the need for very efficient anharmonic pumping. In fact the

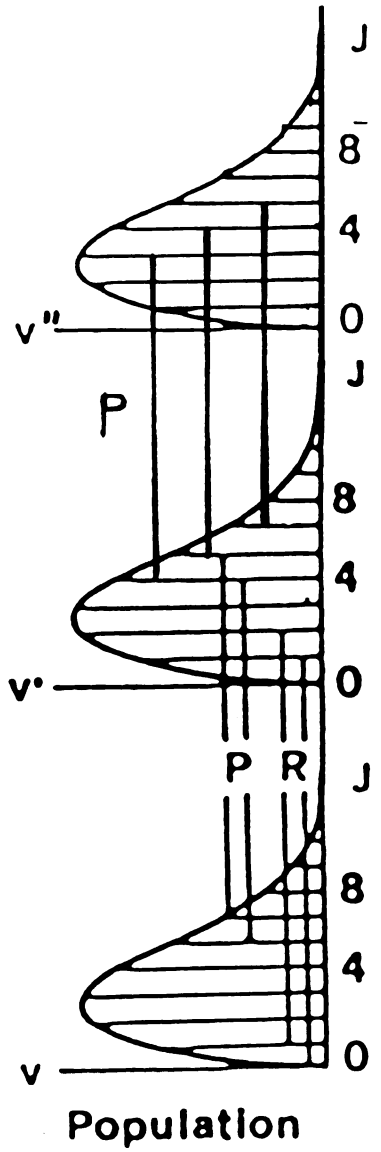

Figure 11. Partial inversion between two vibrational rotational states with the vibrational states having the same polulation.

overpopulation of the high vibrational levels compared to the Boltzmann distribution, and hence the degree of partial inversion, increases rapidly with decreasing translational temperature.

The first sealed-off operation of a stable CO laser was reported by C. Freed in 1971 [32], with a power output that was much lower than achieved for a flowing gas system. The CO laser used in our laboratory has a design similar to that reported by Freed. A 1.2 meter long semi-sealed plasma tube is used with a single Ni cathode in the center and two 0.6 m discharge paths to Ni anodes in both ends. The anodes are connected to a 3 kV voltage-regulated power supply through 0.2 MΩ resistors, whereas the cathode is connected directly to a -6 kV voltage-regulated power supply. The typical cathode voltage relative to the anodes is near -6.4 kV with total currents of about 18 mA. One end of the laser cavity is a replica grating with 150 grooves/mm, while the other end is a ZnSe partially transmitting mirror whose inner surface is concave with a 5 m radius and coated for 93% reflectivity at 5.4 μm and whose outer surface is convex with a 3 m radius and is anti-reflection coated. The end mirror is mounted on a piezoelectric translator (PZT) for resonator cavity length adjustment. The discharge tube is sealed with CaF_2 windows at the Brewster angle. The laser gas mixture consists of 2.5% CO, 3.5% Xe, 18.5% N_2 and 75.5% He at a total pressure of 15 - 17 Torr. The laser is

operated with the discharge tube cooled to about -72 °C. The output power ranges from ~1 W around 1800 cm^{-1} to ~0.2 W in the 1700 cm^{-1} region. The accessible spectral region is from 1650 to 1950 cm^{-1}.

3.2 CO-MW Sideband Laser Spectrometer

A block diagram of the spectrometer is shown in Figure 12. Except for the CO laser and its more primitive frequency stabilization system, the spectrometer is the same as that employed by us for sideband laser spectroscopy in the CO_2 laser region. The horizontally polarized CO laser radiation output is directed to the CdTe electrooptic crystal, 3.1 x 3 x 25 mm, which is mounted inside a matched double-ridged microwave housing. The vertically polarized microwaves are directed through the crystal by H-plane double-ridged bends which have 3-mm holes drilled in them for access by the infrared radiation. The small ends of the crystal have a special broadband anti-reflection coating that provides > 97% transmission from 5 - 11 μm to prevent the loss of infrared power by reflection, so that the crystal can be used in either the CO or the CO_2 laser region.

In order to make sure that the whole laser beam goes through the small crystal the infrared beam is focussed into the crystal and recollimated afterwards by ZnSe lenses

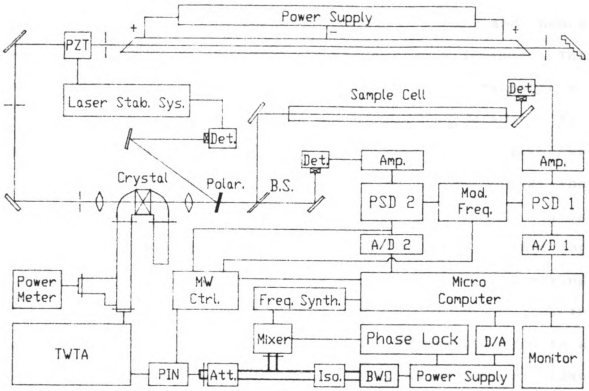

Figure 12. Block diagram of the CO microwave sideband laser spectrometer.

having 25 cm focal length. After leaving the recollimation lens, the laser beam is directed through a polarizer which is set to pass radiation whose plane of polarization is perpendicular to the incoming infrared beam and hence reflects most of the carrier and passes the sidebands. The reflected carrier is directed to a pyroelectric detector or through a laser Stark cell to a HgCdTe detector for stabilization of the laser. Most of the work to date has been performed with the laser stabilized to the top of the Doppler broadened laser gain curve [Figure 13]. This configuration yields an accuracy of 5 MHz at best by applying a 520 Hz dither voltage to the PZT and processing the output of the pyroelectric detector with a lock-in amplifier. However, the laser has also been stabilized to a saturation dip in a laser Stark spectrum, which provides better control of the laser frequency with the disadvantages of slightly poorer knowledge of the value of the frequency and time-consuming optical alignment. As will be seen later, we believe that the accuracy of the sideband spectrometer for frequency measurement is limited at present by the gain curve resettability and knowledge of the laser frequency.

After passage through the polarizer, the sideband power is split by a beam splitter into sample and reference beams; each beam is monitored by a HgCdTe photoconductive detector. The reference detector is used to stabilize the amplitude of

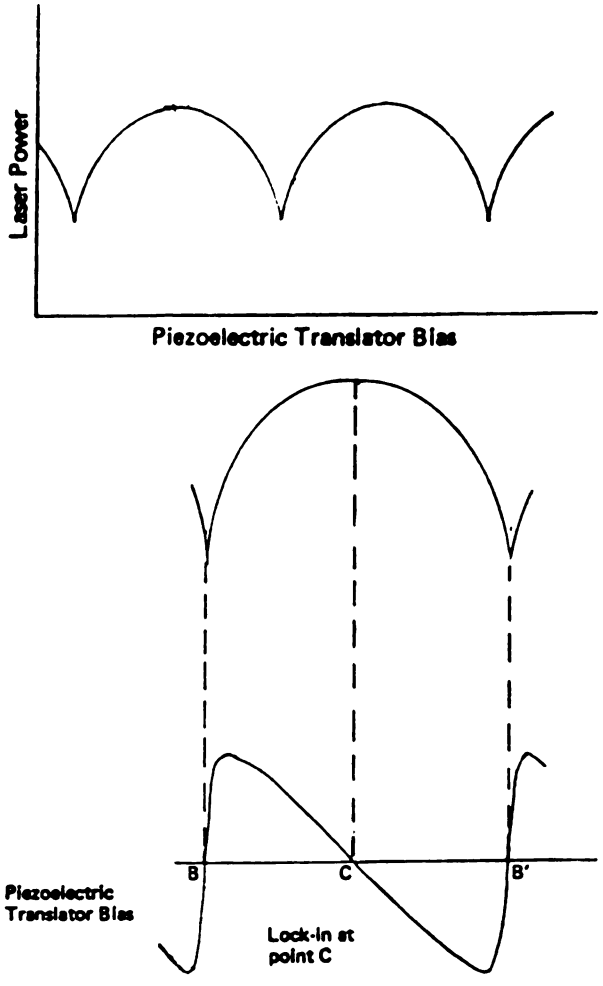

Figure 13. The upper graph shows the Doppler gain curve vs. the PZT bias voltage and the lower graph shows the stabilization on the top of the gain curve.

the sideband power in the manner described below, while the sample detector measures the absorption in one of several simple glass tubes with NaCl windows used for sample cells.

The microwave power is provided by a phase-locked backward wave oscillator (BWO) and is amplified to ~20 W afterward by a traveling wave tube amplifier (TWTA). The WRD-750 double ridged waveguide housing for the CdTe crystal is useful in the 8 - 18 GHz frequency range and the TWTA provides usable output across that range as well. However, two BWO's, one for 8 - 12.4 GHz and one for 12.4 - 18 GHz, are needed. The power supplies for the BWO's are of our own design except for the helix voltage, which is provided by a commercial operational power supply (OPS). The power supplies include a provision for adding a frequency controlling voltage to the OPS output.

The microwave frequency is controlled by a minicomputer (PDP-8) or a personal computer (IBM-PC/AT) that also reads the outputs of the sample and reference detectors. For each microwave frequency selected, the computer programs a digital-to-analog converter that drives the OPS to provide a helix voltage that brings the microwave frequency into the capture range of a commercial microwave synchronizer. The reference frequency for the stabilization is supplied by one of two radio frequency synthesizers operating in the 400 - 440 MHz range; the synthesizer frequency is also controlled by the computer. The RF output and a portion of

the microwave power are mixed in a commercial broad-band mixer-multiplier and the beat frequency is directed to the phase-locking synchronizer. The computer is programmed in such a way that, after a simple adjustment of the offset and gain of the operational power supply, any frequency region of any width within the BWO band can be scanned at any desired interval (subject to a limitation on total number of points) at any rate up to 50 frequencies/sec, which is limited by the settling time of the RF synthesizers and the speed of the computer program. The overall stability and frequency accuracy of the microwave system is < 1 kHz.

For modulation purposes, a PIN diode switch was first placed in the microwave line between the BWO and the TWTA to perform a 100% square wave amplitude modulation of the microwave power and therefore a 100% square wave amplitude modulation of the laser sidebands. However, even though the crystal and its housing have been carefully matched to the microwave input, there is still substantial variation of sideband amplitude with frequency. In Figure 14 the sideband signal from the lockin amplifier that measures the infrared radiation at the sample detector with an empty sample cell is compared to the microwave output power in the 14.5 - 16.5 GHz region. It appears that the variation in sideband power is mainly a result of the output microwave power variation from the TWTA; this can be attributed to three factors: 1. microwave output power variation vs.

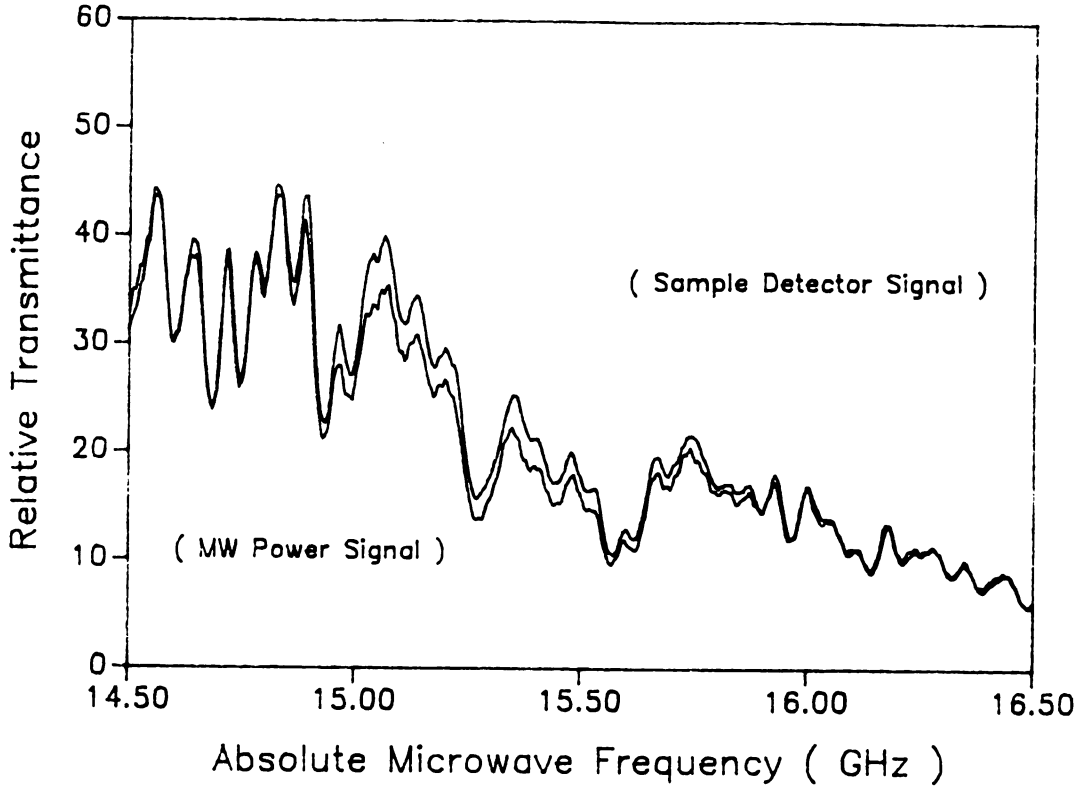

Figure 14. Simultaneous recording of the relative sample detector signal with an empty sample cell and the relative microwave power signal with 100% amplitude modulation applied and no leveling. The horizontal axis is the frequency of the microwave source used to generate the sideband.

frequency from the backward wave oscillator; 2. frequency dependent amplification of the TWTA; 3. variation of microwave power due to reflections in the microwave circuit. It seemed to us that it should be possible to use the output of a microwave power meter that monitors the TWTA output in a feedback loop to level the microwave power and hopefully thereby flatten the sideband amplitude. For this purpose an attenuating PIN diode and an electronic circuit designed by Mr. Martin Rabb are used. More detail will be given in the next section.

3.3 Simultaneous Microwave Modulation/Power Leveling Device

The location of the amplitude modulation and power leveling device is shown in the block diagram of the sideband spectrometer in Figure 12 and the detailed circuit diagram of the feedback control is shown in Figure 15. For this purpose, a PIN diode attenuator (General Microwave Corporation, Model 1958) rather than a PIN diode switch is used, because an attenuator diode allows control of the degree of the microwave attenuation by variation of the diode current. The model 1958 Atttenuator/Modulator operates in the 6 - 18 GHz range with a maximum insertion loss of 2.5 dB and a maximum VSWR of 1.8. There are four parts to the electronic circuit in Figure 15: a current switching transistor, a current control circuit, a current

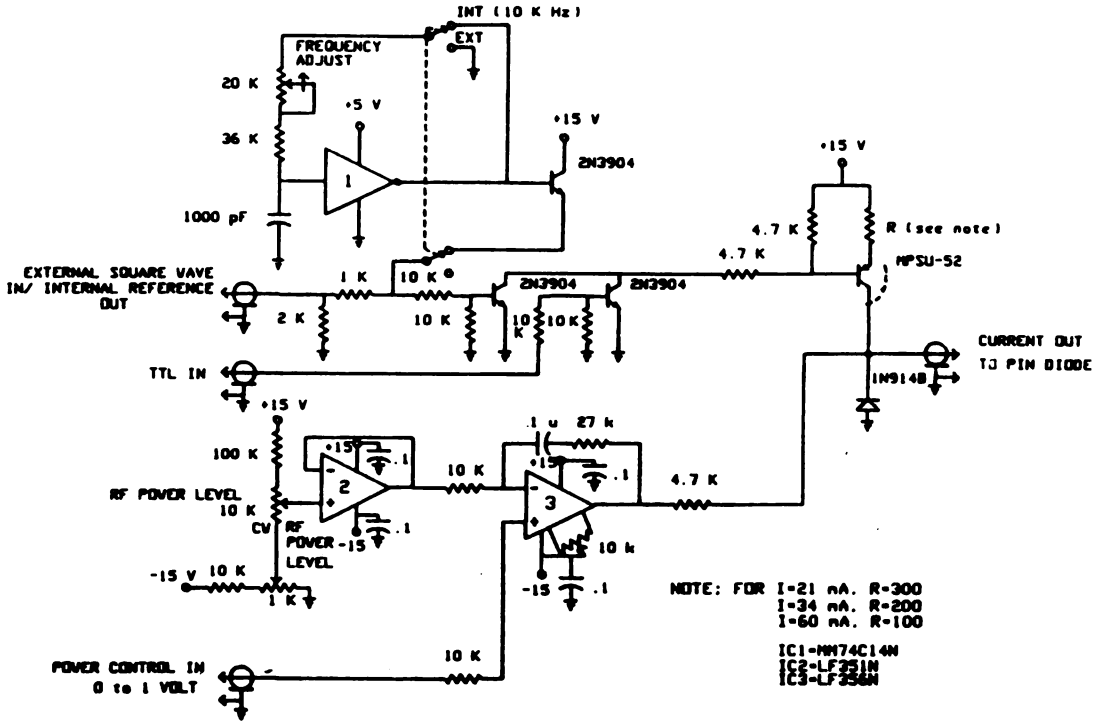

Figure 15. Circuit diagram for the amplitude modulation and control electronics. The circuit provides the drive current needed to control the microwave attenuation of a PIN diode.

switching circuit, and a square wave generator. The attenuation of the PIN diode increases with increasing drive current, reaching 60 dB at drive currents ranging from 15 to 70 mA, according to the manufacturer. Our units reach maximum attenuation at a drive current of ~40 mA. Typical attenuation values for various values of the current for our units, again according to the manufacturer, are 10, 20 and 30 dB attenuation for 1, 3, and 6 mA, respectively. A more detailed description of the circuit itself is given in Ref. 33.

With this circuit the microwave attenuation through the PIN is switched between two values, one > 60 dB ("off") and the other ("on") determined by comparison of an internally generated DC voltage with an external input voltage that may be derived from output of a microwave power meter or the output of a lockin amplifier which measures the infrared radiation at the reference detector. For test purposes, an empty sample cell was used with the microwave power meter output connected to the control device. The sideband power and the microwave power are shown in Figure 16 with the microwave power controlled to be a constant value. Although the sideband power variation is smoother than in Figure 14, the still varying sideband power shows that in addition to the microwave power variation, the sideband power is also affected by the infrared laser power variation and by the changes of the laser sideband

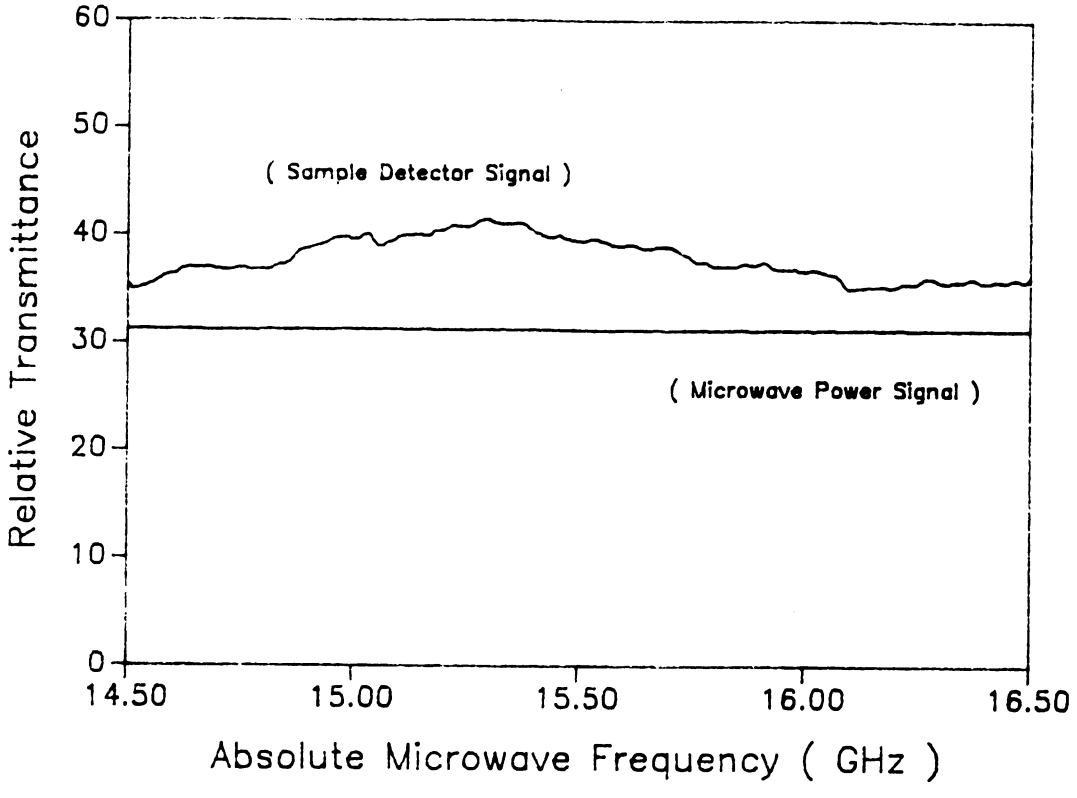

Figure 16. Recording of the sideband power as a function of microwave frequency when the microwave power is controlled by leveling the output of a microwave power meter.

generation efficiency vs. frequency.

To reduce the variation of sideband power as the frequency is changed, the processed output from the reference detector is used to control the attenuation of the PIN diode during the "on" portion of its cycle. Figure 17 shows the simultaneously recorded infrared amplitude from the sample detector and the leveled infrared amplitude from the reference detector. As long as the system is within the dynamic range of the microwave power generation, the background for a spectrum may be adjusted to be exceptionally flat. The slightly tilted sample signal reveals the effects of variation in the optical paths between the two beams and the effect of the relatively small detector crystal size (1 x 1 mm) to the beam size. It shows that by using the microwave power control we can not only level the variation of the input microwave power but also compensate for changes in the power of the infrared laser and for the variation of the sideband conversion efficiency.

Figure 18 shows that when the reference sideband signal is controlled and leveled, the sample signal appears as a flat line but the microwave power varies, inversely in comparison with the sample sideband power shown in Figure 16 where the power is controlled by leveling the output of microwave power meter.

In our first spectroscopic studies with the sideband

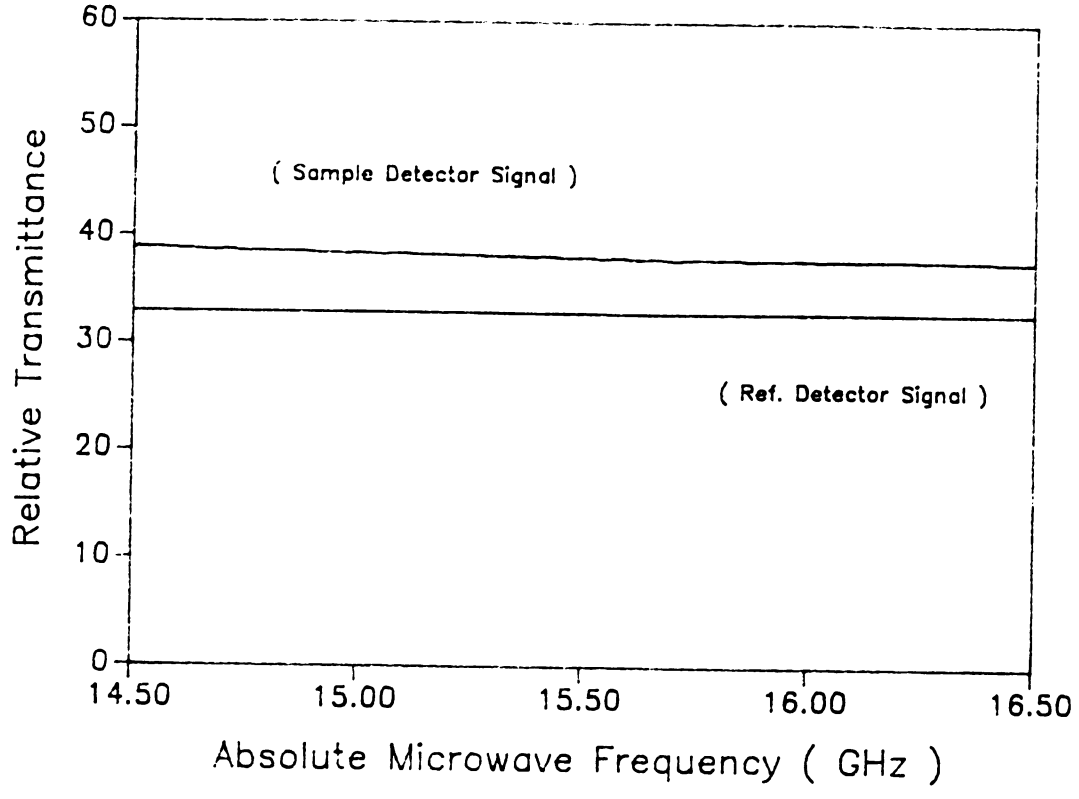

Figure 17. Simultaneous recording of the sample detector signal with an empty sample cell and the reference detector signal with reference detector signal leveled.

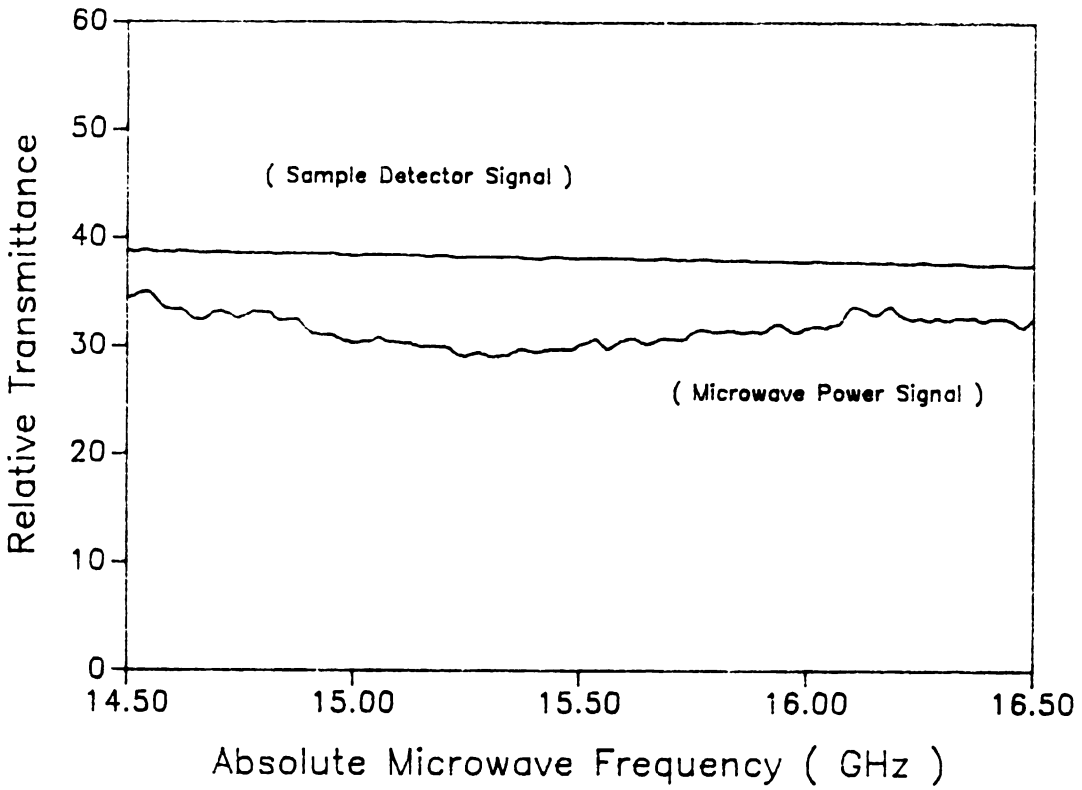

Figure 18. Recording of both the sample detector signal and the microwave power signal as a function of microwave frequency with an empty sample cell when the reference detector signal is leveled.

system we performed a double beam experiment in which the radiation was split into two parts by a beam splitter, with one part directed to a reference detector and the other part passed through a sample cell to a signal detector and only the 100% amplitude modulation was applied. The raw spectrum of the amplitudes of the two beams with ~200 mTorr H_2CO inside the sample cell is shown in Figure 19. The recorded outputs of both two detectors were later ratioed to obtain the spectrum [Figure 20]. With the control circuit the spectrum with a flattened background could be shown [Figure 21] on the monitor screen directly by using the output of the reference detector in a feed back loop to control the microwave power and thereby level the sideband amplitude.

This system has been used in the CO_2 sideband laser in our laboratory [8 - 10]. The use of this combination of sideband power stabilization and modulation has three advantages in ordinary spectroscopy. First, it is convenient to use; as long as the system is within the dynamic range of the microwave power generator, the background for a spectrum is very flat. Second, comparison of Figure 20 and 21 reveals that higher signal-to-noise ratio is obtained in the spectrum of the latter figure. Part of the reason for the improvement is due to the digitization error, which is increased by ratioing two small digitized signals, and part appears to be the result of

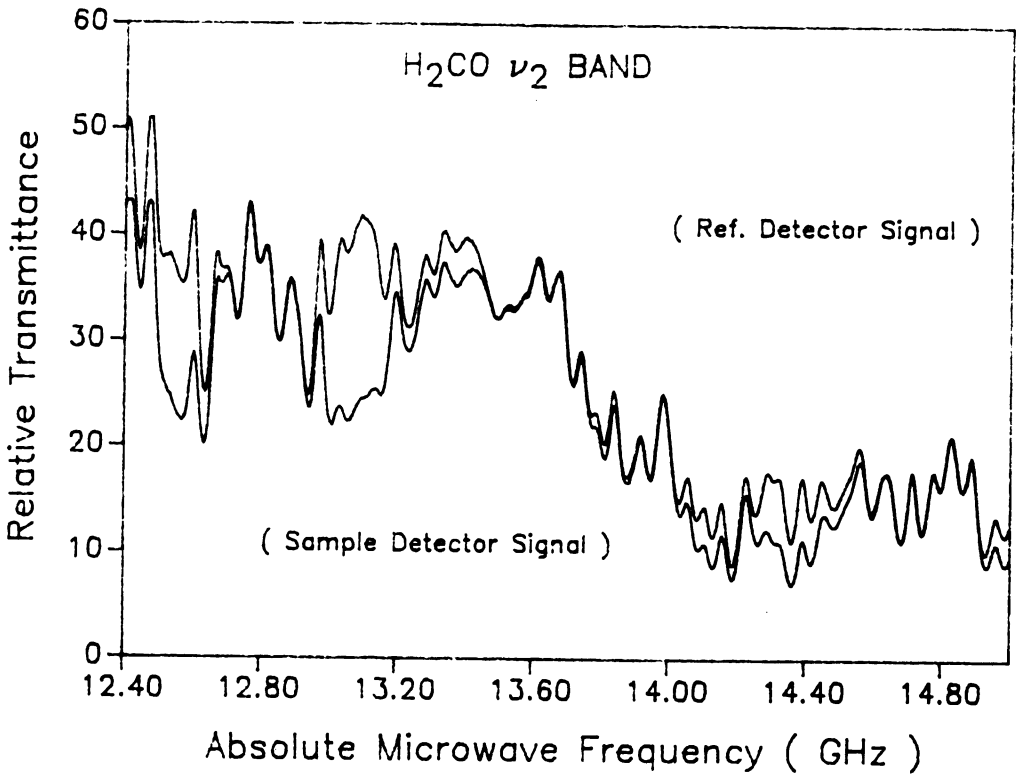

Figure 19. The raw spectrum with simultaneous recording of the sample detector signal and the reference detector signal with 100% amplitude modulation applied only. The sample is H_2CO at ~200 mTorr in a 1 m sample cell.

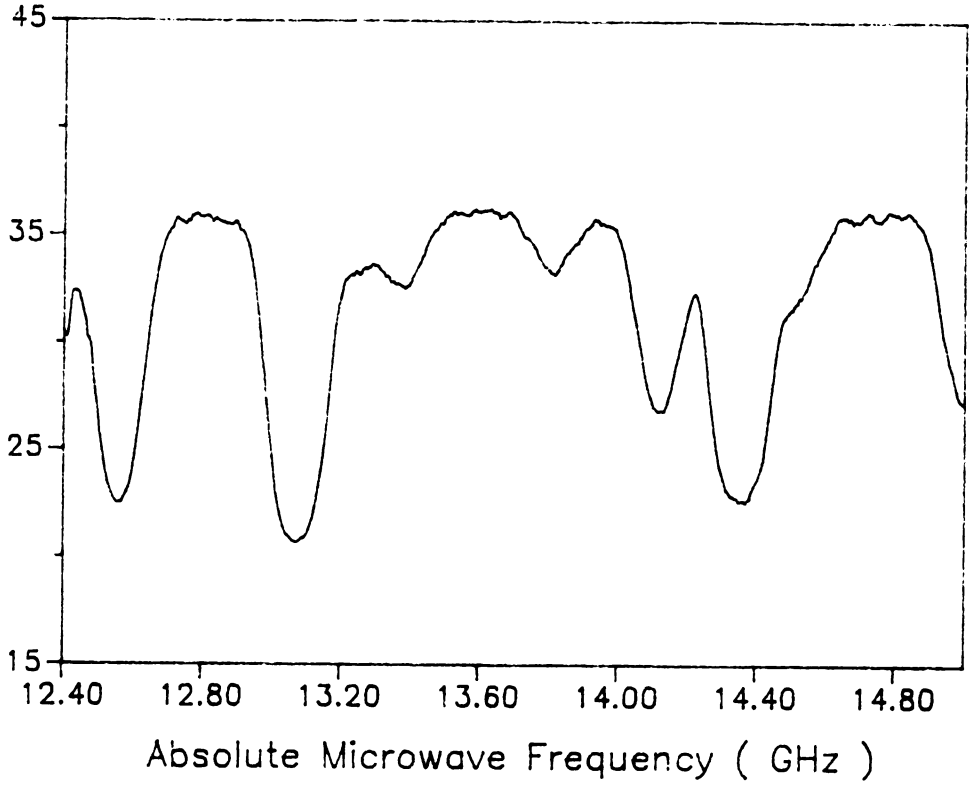

Figure 20. Ratio of the outputs of the sample and reference detectors for the spectrum shown in Figure 19. The vertical axis is in arbitrary units.

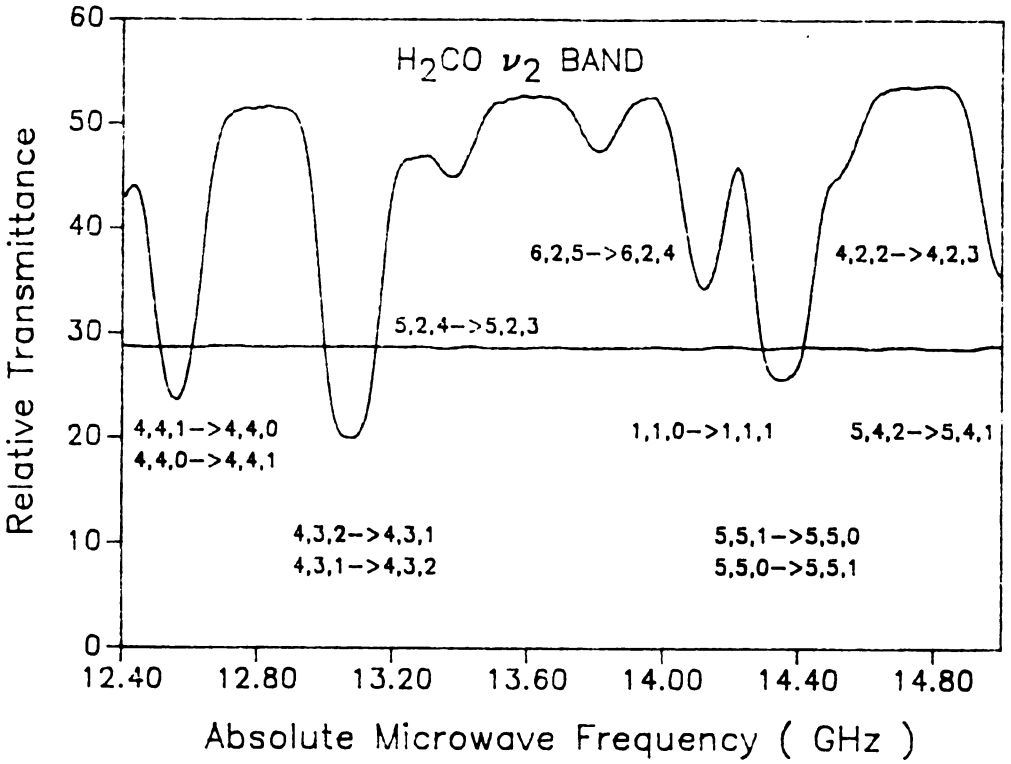

Figure 21. Recording of the spectrum described in Figure 19, taken with the amplitude modulation and control circuit activated. The flat line is the output of the reference detector used to control the sideband power by controlling the microwave power.

compensation of noise from the infrared laser by the sideband leveling system. Third, although the total intensity of the carrier is much larger than that of the sidebands, the intensity of modulated carrier is comparable to that of the modulated sidebands, but with a different polarization. The polarizer reduces the intensity of modulated carrier relative to modulated sidebands by almost three orders of magnitude. Thus, while there is substantial carrier power after the polarizer, it is not modulated and we have been able to ignore it in all of the spectroscopy that we have carried out to date.

CHAPTER 4

Performance Test and Conclusions

Several hundred transitions in samples of HCOOH, N_2O, OCS, H_2CO, and D_2CO have been recorded with the CO laser sideband system to gain practice with the new CO laser and to test the performance of this system. In this chapter the tests for absolute frequency accuracy and the reproducibility of our new CO sideband laser system are described in the following sections and finally some conclusions will be stated.

4.1 Absolute Frequency Measurements

After the assembly and adjustment of the CO sideband laser spectrometer, we thought that operation of the new system would be as easy as, and the performance would be similar to, the CO_2 sideband laser spectrometer. The first transition selected for study was the ν_3 vibrational band of HCOOH. A preliminary FT-IR spectrum taken by Dr. Dean Peterson with 0.1 cm^{-1} resolution is shown in Figure 22. A portion of the spectrum of HCOOH taken by the CO sideband laser system is shown in Figure 23. In the course of our experiment, a study of the same vibration-rotation band with a combination of FTIR and laser Stark Lamb dip techniques was published by Weber et al. [34]. We decided to stop at

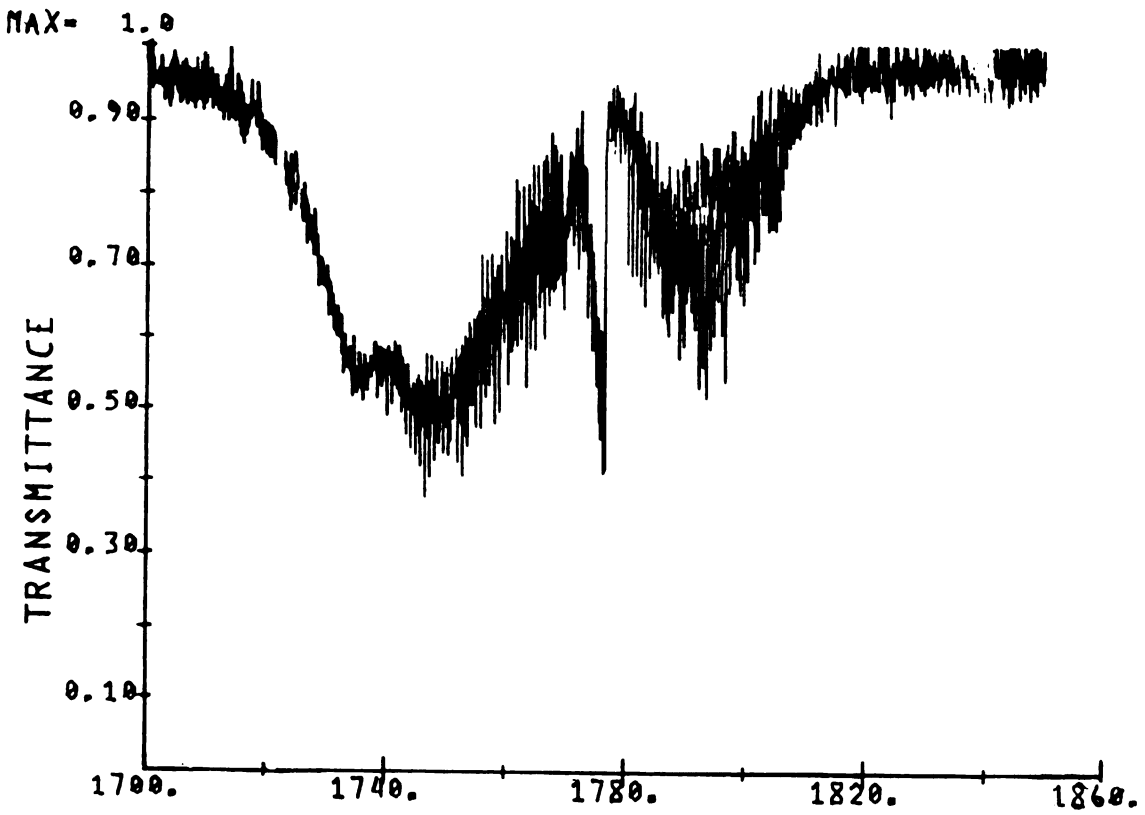

Figure 22. A preliminary spectrum of HCOOH, ν_3 vibrational band, taken by a BOMEM DA 3.01 FTIR spectrometer with 0.1 cm^{-1} resolution.

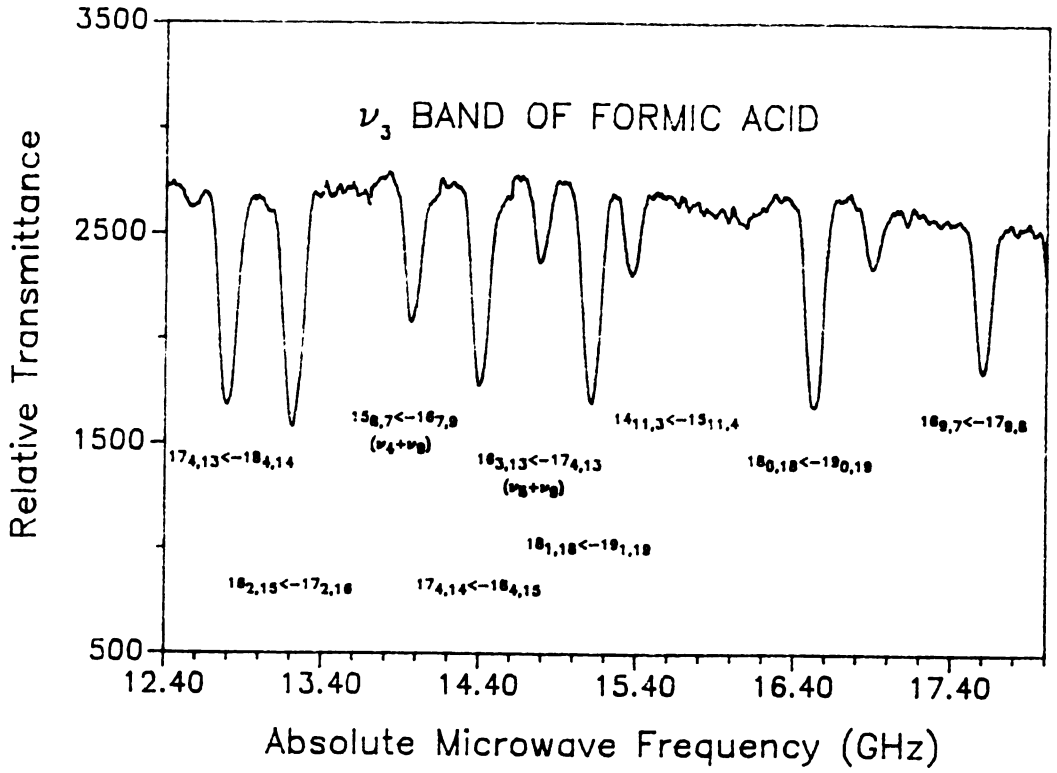

Figure 23. A portion of the CO sideband laser spectrum of HCOOH. The CO laser line is $^{12}C^{16}O$ 13 to 12 P(18). The microwave frequencies on the horizontal axis must be added to or subtracted from the frequency of this laser line to obtain the frequencies of the transitions.

that point and compare our observed frequencies with the newly-published values to determine how well our system works. To our surprise we found that there was a ~10 MHz difference in this absolute frequency comparison. In order to understand the origin of this discrepancy an extensive study of known spectra was undertaken.

A number of tests of frequency measurement with the new system were performed. Most of these tests involved transitions in the $01^{1}1 \leftarrow 00^{0}0$, combination band of $^{14}N_2{}^{16}O$ (~1850 cm^{-1}) and the $20^{0}0 \leftarrow 00^{0}0$, overtone band of $^{16}O^{12}C^{32}S$ (~1720 cm^{-1}), which we will hereafter refer to as N_2O and OCS, respectively. Transitions in these bands have been the subject of precise frequency measurements [35 - 37] by a heterodyne laser technique that gives frequencies based on accurately measured CO_2 laser frequencies. We will use the N_2O and OCS frequencies reported in these papers as reference frequencies for our measurements.

The samples of N_2O and OCS are commercial cylinder gases obtained from Ohio Medical Supply and Union Carbide Corporation, respectively. Except for the usual freeze-pump-thaw cycling, the samples were used as received. The sample pressures (~ 7 Torr for N_2O and ~ 0.4 Torr for OCS) were estimated with a capacitance manometer. All of the measurements were carried out in a 1 meter sample cell and at room temperature.

For the spectroscopic frequency measurements, the output of the lock-in amplifier monitoring the sample detector was digitized by the computer and recorded on disc. The lineshapes were later fitted directly by the method of least squares to a Gaussian function and the center frequency was noted. In principle, the sample detector measures transmission [Figure 24], and the logarithm of the percent transmission is the quantity that should be fit to a lineshape function. Unfortunately, this requires knowledge of the zero of transmission, which is not easily attainable with our spectrometer, or an additional parameter in the fitting; it also requires more effort to determine starting parameters for the least squares iteration. We have found by a number of tests of theoretical and experimental lineshapes that the direct fitting gives center frequencies that are well within the standard error of either fitting. Consequently, the simpler procedure was adopted for all of the frequency measurements in this work. Of course, the simpler fitting approaches the correct procedure as the percent absorption decreases. The fitting program contains provision for a linear slope of the 100% transmission line that may occur as a result of incomplete stabiliaztion of the sideband power caused by optical differences in the sample and reference paths. Such a slope can lead to significant errors in frequency measurement if not compensated.

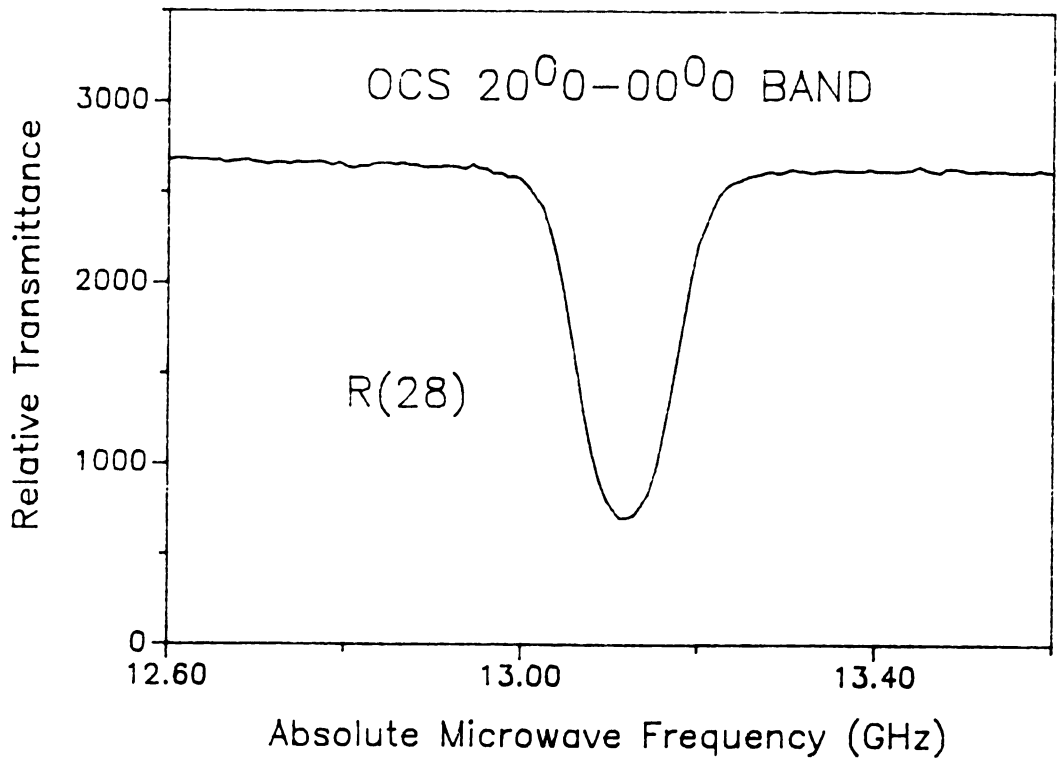

Figure 24. A typical CO sideband laser spectrum of OCS. The relative transmittance vs. absolute microwave frequency is directly fitted to a Gaussian function by the least squares method to obtain the center microwave frequency of the transition. The microwave frequency is added to the frequency of the $^{12}C^{18}O$ 14 to 13 P(14) laser line to obtain the infrared frequency of this transition.

Typical spectra of N_2O in the 1880 cm^{-1} region and of OCS in the 1720 cm^{-1} region are shown in Figures 25 and 26, respectively. The absolute frequencies measured in this work are compared to the reported frequencies in Table III and Table IV for N_2O and OCS, respectively. They show that there is always a positive ~10 MHz difference between our measurement and the reference frequency in the 1880 cm^{-1} region and a positive ~5 MHz difference in the 1720 cm^{-1} region. That was something that we needed to investigate.

Since the sideband laser frequency is obtained by the addition or subtraction of the microwave frequency from the IR laser frequency, and the microwave frequency is known accurately within 1 kHz, we concentrated on possible discrepancies in the IR laser frequencies. Uncertainty in the CO laser frequency can be attributed to two possible problems, the error caused by the stabilization scheme and the knowledge of the CO laser frequency itself.

Frequency measurements by the infrared microwave sideband technique require accurately known frequencies of the gas laser transitions used to generate the sidebands. This is not a problem in the CO_2 laser region, where it is relatively easy to stabilize the laser transitions on the fluorescence Lamb dip [38] reproducibly to better than within 100 kHz of frequencies that have been measured to even higher accuracy. The situation is very different in the CO laser region where, although CO saturation dips have

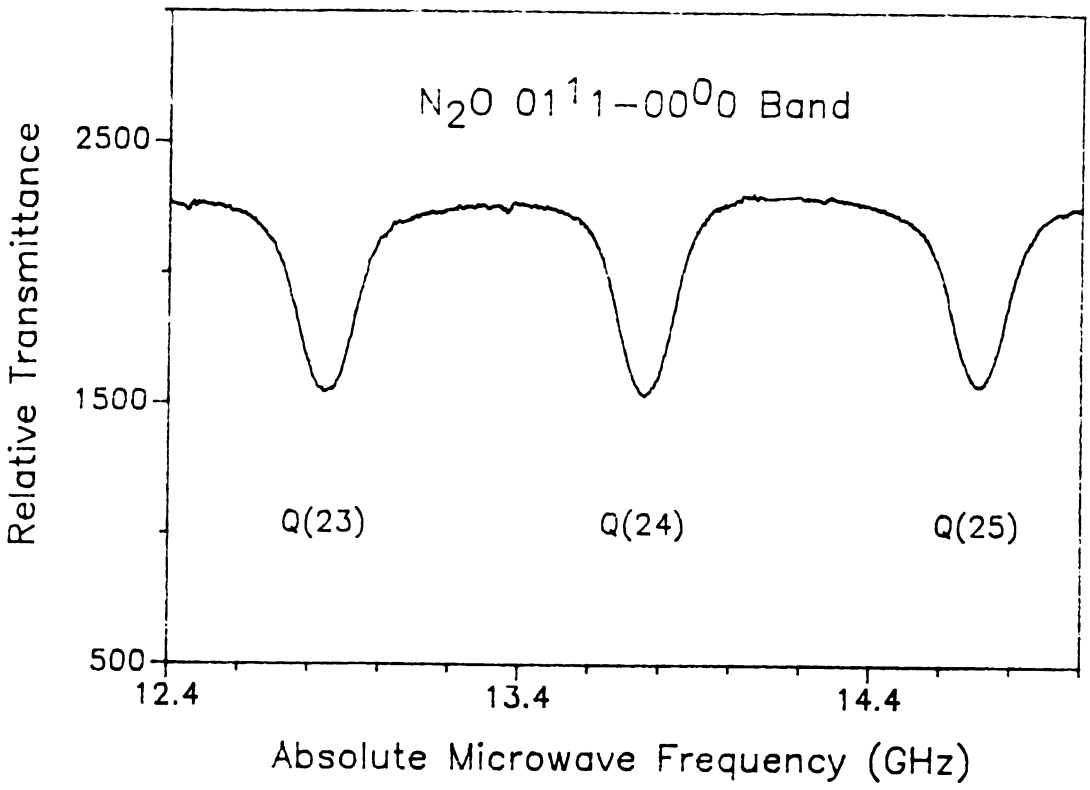

Figure 25. A CO sideband laser spectrum of N_2O at ~7 Torr pressure in a 1 meter sample cell; the CO laser line used here is $^{12}C^{16}O$ 9 to 8 P(14). The microwave frequencies are subtracted from the laser frequency to obtain the frequencies of the transitions.

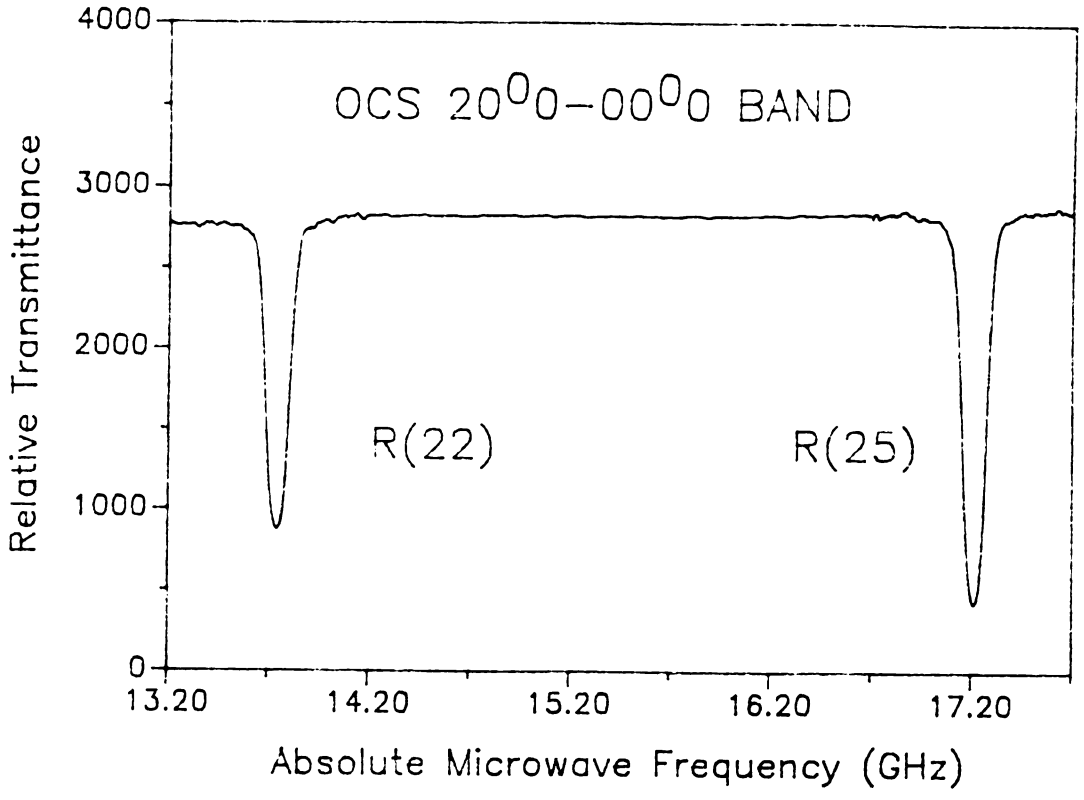

Figure 26. A CO sideband laser spectrum of OCS at ~200 mTorr pressure in a 1 meter sample cell; the CO laser line is $^{13}C^{16}O$ 14 to 13 P(15). The microwave frequencies for R(22) and R(25) must be subtracted from and added to the laser frequency, respectively, to obtain the frequencies of the transitions.

Table III.

Comparison of Frequencies (MHz) of Transitions

in the $01^{1}1$ <- $00^{0}0$ Band of N_2O

Transition	Laser Line[a]	ν(mic)[b]	ν(obs)[c]	ν(ref)[d]	O-R[e]
P(38)	10-9 P(16)α	-17912.4	55350336.0	55350324.7	11.3
P(25)	10-9 P(13)α	-14978.8	55713400.1	55713392.7	7.4
P(24)	9-8 P(19)α	-15295.9	55740708.4	55740700.9	7.5
P(10)	9-8 P(16)α	-14518.3	56113574.2	56113562.2	12.0
P(4)	9-8 P(15)α	17735.7	56267906.9	56267897.7	9.2
R(16)	8-7 P(17)α	15616.5	56781767.0	56781755.2	11.8
R(20)	8-7 P(16)β	-15322.8	56874935.9	56874929.2	6.7
P(30)	8-7 P(17)β	-13033.0	55575530.7	55575516.1	14.6
P(29)	8-7 P(17)β	14720.7	55603284.5	55603268.9	15.6
P(31)	8-7 P(18)γ	-12618.8	55547685.9	55547674.8	11.1
P(30)	8-7 P(18)γ	15224.6	55575529.3	55575516.1	13.2
P(18)	8-7 P(15)γ	-13033.8	55902686.6	55902667.8	18.8
P(17)	8-7 P(17)γ	13641.1	55929361.5	55929347.1	14.4

a. Isotopes are as follows: α = $^{12}C^{16}O$; β = $^{12}C^{18}O$; γ = $^{13}C^{16}O$.

b. Microwave frequency to be added algebraically to laser frequency to obtain observed transition frquency.

c. Transition frequency observed in this work; laser frequencies from Ref. 44.

d. J. S. Wells, A. Hinz, and A. G. Maki, J. Mol. Spectrosc., vol. 114, pp. 84-96 (1985)

e. ν(obs) - ν(ref).

Table IV.

Comparison of Frequencies (MHz) of Transitions

in the $20^0 0$ <- $00^0 0$ Band of OCS

Transition	Laser Line[a]	ν(mic)[b]	ν(obs)[c]	ν(ref)[d]	O-R[e]
OCS R(41)	15-14 P(15)α	16904.9	51737926.9	51737920.9	6.0
OCS R(54)	15-14 P(14)α	12746.9	51848559.3	51848553.6	5.7
OCS P(8)	15-14 P(11)β	-14299.0	51194433.2	51194427.3	5.9
OCS R(52)	14-13 P(12)β	13126.2	51832378.6	51832375.0	3.6
OCS R(28)	14-13 P(14)β	13118.4	51614482.5	51614478.4	4.1
OCS R(25)	14-13 P(14)β	-17169.5	51584194.6	51584191.8	2.8
OCS R(22)	14-13 P(15)γ	-13745.4	51553242.5	51553234.4	8.1
OCS R(25)	14-13 P(15)γ	17213.6	51584201.5	51584191.8	9.7
OCS R(2)	14-13 P(17)γ	-12908.0	51329838.9	51329828.6	10.3
OCS R(45)	14-13 P(13)γ	-14210.0	51773343.3	51773335.2	8.1
OCS R(58)	14-13 P(13)γ	-16455.1	51879992.6	51879985.5	7.1
OCS R(62)	14-13 P(13)γ	13739.4	51910187.1	51910178.2	8.9
OCS P(4)	14-13 P(18)γ	15437.9	51244695.9	51244688.2	7.7

a. Isotopes are as folows: α = $^{12}C^{16}O$; β = $^{12}C^{18}O$; γ = $^{13}C^{16}O$.

b. Microwave frequency to be addded algebraically to laser frequency to obtain observed transition frquency.

c. Transition frequency observed in this work; laser frequencies from Ref. 44.

d. J. S. Wells, F. R. Peterson, and A. G. Maki, J. Mol. Spectrosc., vol. 98, pp. 404-412 (1983)

e. ν(obs) - ν(ref).

been observed [39] and stabilization on the saturation dips by use of the optogalvanic effect has been performed [40]. Most CO lasers are still stabilized to the top of the gain curve, which means that an uncertainty up to ~5 MHz is unavoidable because of the distortion of the gain curve by multimode oscillation of the laser and the numerous optical reflections. In addition to this, there is a tendency for a CO laser to oscillate on more than one laser transition. When this happens, stabilization to the top of the a gain curve could cause ~40 MHz error. Figure 27 shows an unusual example in which the same D_2CO transitions were observed in the same spectrum twice at different applied microwave frequencies because of multiline CO laser oscillation. Fortunately, we found that in most cases it is possible, by rotating the grating, by changing the size of diaphragms in the laser cavity, and by adjusting the laser current across the gain tube [41], to make the laser oscillate on only one line.

For knowledge of the CO laser frequency, only a limited number of frequencies of a Lamb dip stablilized $^{12}C^{16}O$ laser have been measured, and these have not yet been published [42]. For the measurements described here, we used three sources of CO laser frequencies. Two of these are measurements of a large number of CO transitions by grating and Fourier transform spectroscopy, an older report by Dale et al. [43] that includes a number of difference frequency

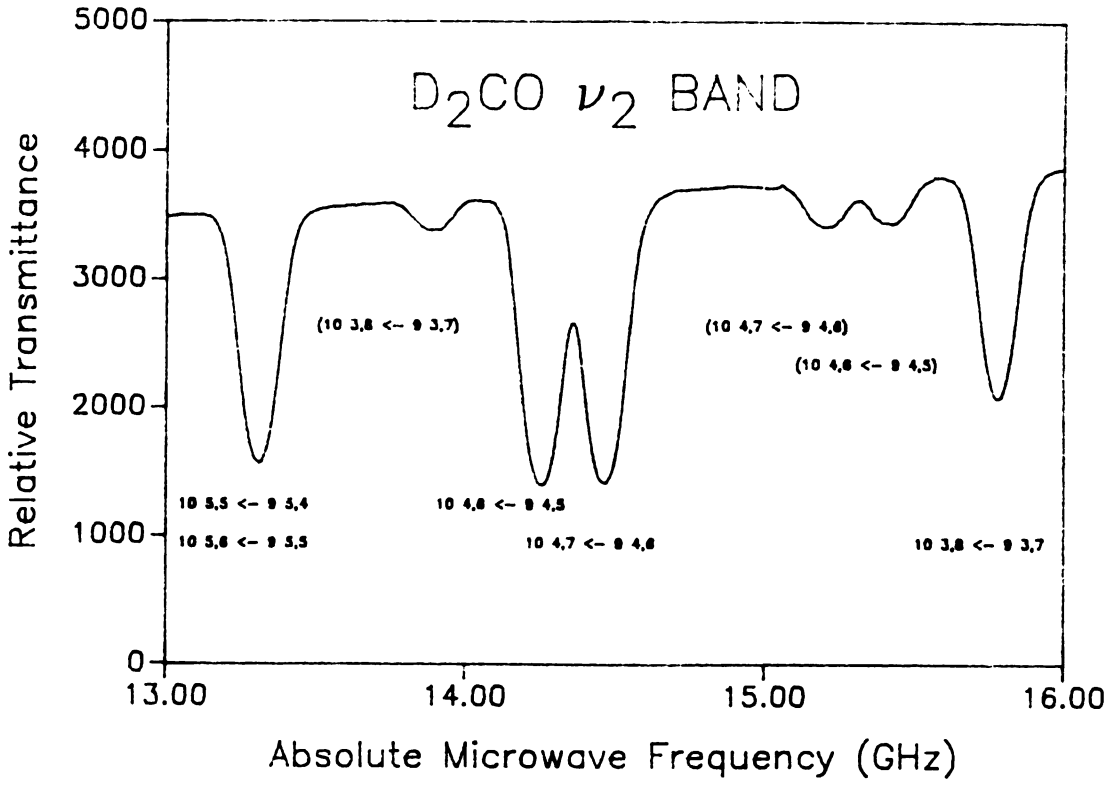

Figure 27. The same D_2CO transitions at two different microwave frequencies, observed in a spectrum because of multiline CO laser oscillation. The transitions in parentheses are from the $^{13}C^{16}O$ 14 to 13 P(15) laser line at 1720.08957 cm^{-1}; the other set of transitions is from the $^{13}C^{16}O$ 13 to 12 P(21) laser line at 1721.07758 cm^{-1}. The microwave frequencies must be added to or subtracted from the laser frequency, respectively, to obtain the frequencies of the transitions.

measurements and a more recent report by Guelachvili et al. [44]. The third source of CO frequencies is a limited set of measurements reported in the papers describing the heterodyne measurements on N_2O [35] and OCS [37]. Some frequencies in the regions of interest from the three sources are compared in Table V, where differences as large as 30 MHz (0.001 cm^{-1}) are seen.

In Tables III and IV the frequencies of several transitions in N_2O and OCS are compared to frequencies measured by a heterodyne technique. The CO laser frequencies reported by Guelachvili et al. [44] were used for our measurements. The most obvious point is that all of our frequencies are higher than the heterodyne results and that the differences are larger in the 1850 cm^{-1} region than in the 1720 cm^{-1} region. This same trend is seen in a comparison of the second and third columns of Table V, where the heterodyne measurements of the laser frequencies are lower than the FTIR results of Guelachvili et al. [44] and the differences are larger in the higher frequency region. Corresponding differences are seen between FTIR values and the recent Lamb dip measurements [42], which are within ~2 MHz of the heterodyne results. If the mean difference between the FTIR values and the heterodyne frequencies in each of the two regions is subtracted from our values, the mean difference in frequency between our results for N_2O and OCS is ~3 MHz, which is probably the result of some

Table V.

Comparison of Reported Values of CO Laser Frequencies (MHz)

CO Laser[a]	Refs. 35,37[b]	Ref. 44[c]	Ref. 43[d]
V=17 TO 16 P(12)	50566284.6	50566287.6	50566261.9
V=17 TO 16 P(11)	50676003.6	50676008.3	50676982.5
V=16 TO 15 P(14)	51088540.3	51088573.5	51088547.5
V=15 TO 14 P(20)	51132433.3	51132435.8	51132404.5
V=16 TO 15 P(13)	51201324.6	51201327.9	51201302.4
V=15 TO 14 P(19)	51252087.8	51252089.9	51252059.7
V=15 TO 14 P(18)	51370776.2	51370779.9	51370750.8
V=15 TO 14 P(16)	51605247.0	51605250.5	51605223.3
V=15 TO 14 P(15)	51721018.1	51721022.4	51720996.1
V=10 TO 9 P(19)	54999306.6	54999314.8	54999301.8
V=10 TO 9 P(15)	55489266.5	55489275.9	55489263.6
V= 9 TO 8 P(18)	55880995.3	55881004.7	55880993.3
V= 9 TO 8 P(15)	56250161.9	56250171.1	56250160.8
V= 9 TO 8 P(14)	56371258.7	56371267.1	56371256.0
V= 7 TO 6 P(19)	57276297.7	57276305.0	57276299.4
V= 7 TO 6 P(18)	57403401.8	57403408.4	57403402.5

a. Laser emission from $^{12}C^{16}O$.

b. Measured by a heterodyne method based on CO_2 laser.

c. Measured by Fourier transform spectroscopy. Frequencies calculated from constants given in Ref. 44.

d. Determined by a combination of grating spectroscopy and measurement of beat frequencies between CO lasers.

combinations of the uncertainty of the heterodyne measurements of N_2O and OCS (~3 MHz) [37] and the stabilization scheme of our system, as described previously. There is also some indication in Tables III and IV that the errors in the FTIR results for the laser frequencies might be different for the different isotopic species, but that conclusion is obscured somewhat by the uncertainties in the present results.

Table VI lists the frequencies of a number of transitions in OCS, N_2O and D_2CO that could be recorded by the infrared microwave sideband system with two different isotopic CO laser lines. Examination of the last column of Table VI, which lists the absolute value of the difference in each case, shows that the measurement uncertainty as a result of uncertainty in the laser frequencies as well as our measurement errors, can be as large as 9 MHz.

4.2 Reproducibility

The reproducibility of frequency measurements from run to run and from day to day are compared in Table VII. In this table the microwave frequencies for the three measurements listed under "A" for each transition were made one right after the other. (The microwave frequency must be added algebraically to the laser frequency to obtain the infrared frequency; therefore, a negative microwave

Table VI.

Comparison of Frequencies of Transitions Measured with Two Laser Lines

Transition[a]	Laser Line[b]	ν(mic)[c]	ν(obs)[d]	$\Delta\nu$[e]
OCS R(25)	14-13 P(14) β	-17169.5	51584194.6	
	14-13 P(15) γ	17213.6	51584201.5	6.9
N_2O P(30)	8- 7 P(17) β	-13033.0	55575530.7	
	8- 7 P(18) γ	15224.6	55575529.3	1.4
D_2CO $23_{3,20}$-$22_{3,19}$	13-12 P(14) β	-16088.7	52302741.0	
	13-12 P(15) γ	16622.9	52302749.8	8.8
D_2CO $22_{5,17}$-$21_{5,16}$	14-13 P(17) α	-12947.3	52222160.9	
	13-12 P(15) β	14631.3	52222161.9	1.0
D_2CO $14_{8,7}$ -$13_{8,6}$	14-13 P(13) γ	17705.4	51805258.8	
	14-13 P(12) β	-14001.1	51805251.5	7.3
D_2CO $10_{8,3}$ - $9_{8,2}$	14-13 P(14) β	-10168.1	51591195.9	
	15-14 P(16) α	-14055.0	51591195.2	0.7
D_2CO $6_{5,2}$ - $5_{5,1}$	14-13 P(16) β	-17749.7	51362055.1	
	15-14 P(18) α	-8727.3	51362052.2	2.9
D_2CO $19_{3,17}$-$18_{3,16}$	15-14 P(12) α	-15772.9	52046658.4	
	14-13 P(10) β	13211.4	52046649.5	8.9

a. Bands are as follows: N_2O $01^11 \leftarrow 00^00$; OCS $20^00 \leftarrow 00^00$; D_2CO ν_2.

b. Isotopes are as follows: α = $^{12}C^{16}O$; β = $^{12}C^{18}O$; γ = $^{13}C^{16}O$.

c. Microwave frequency (in MHz) to be added algebraically to laser frequency to obtain transition frequency.

d. Observed transition frequency in MHz; laser frequencies from Ref. 44.

e. Absolute value of the difference (in MHz) in the two measurements of the transition frequency.

Table VII.

Reproducibility of Frequency Measurements with IR-MW Sideband Laser in the CO Laser Region

Transition[a]	Laser Line[b]	A[c](MHz)	B[d](MHz)
N_2O P(25)	10-9 P(13)α	-14979.28	-14978.28
		-14979.23	-14978.77
		-14979.31	-14978.12
N_2O P(31)	8-7 P(18)γ	-12619.11	-12618.92
		-12619.02	-12618.54
		-12618.84	-12618.21
N_2O P(4)	9-8 P(15)α	17735.41	17736.05
		17735.97	17736.26
		17735.62	17735.04
OCS R(22)	14-13 P(15)γ	-13746.52	-13744.13
		-13746.23	-13744.89
		-13746.24	-13744.22
OCS P(18)	14-13 P(18)γ	15437.20	15438.55
		15437.43	15438.10
		15437.68	15438.40
OCS P(8)	15-14 P(11)α	-14298.94	-14299.13
		-14298.77	-14298.88
		-14299.16	-14298.80

a. Bands are as follows: N_2O $01^11 \leftarrow 00^00$; OCS $20^00 \leftarrow 00^00$.

b. Isotopes are as follows: α = $^{12}C^{16}O$; β = $^{12}C^{18}O$; γ = $^{13}C^{16}O$.

c. Each set of three frequencies in this column were measured on right after the other.

d. Each set of three frequencies in this column were measured one right after the other, but the laser was reset between the measurements in the A and B columns.

frequency indicates that the absorption frequency is less than the laser frequency.) The measurements listed under "B" for each transition were also made one right after the other, but were either made later in the day or on a different day. In either case the laser was made to oscillate on other laser lines between the "A" and "B" sets of measurements. It may be seen that the reproducibility of successive measurements is better than ± 0.5 MHz, whereas the reproducibility from day to day is of the order of ± 4 MHz. In each case, care was taken to insure that the laser was oscillating on only one transition and that the laser output as a function of cavity length was a symmetrical smooth curve before the laser was locked to the peak in that curve.

The two sets of measurements in Table VIII used the same laser line for two different N_2O transitions and the frequencies of the two transitions in column A are made right after one another, as are the frequencies in Column B. It can be seen that the differences in the frequencies in the two columns for these two sets of measurements are all within 3.6 ± 0.4 MHz indicating that the relative accuracy for two transitions measured with the same setting of the same laser line is one order of magnitude better than the resettability of the laser.

Table VIII.

Relative Accuracy of Frequency Measurements with the Same Setting of the CO Laser Gain Profile

---

Laser Line: $^{12}C^{18}O$ 8 to 7 P(17)

Laser Line frequency: Fq^a 1854.23490 cm^{-1} 55,588,563.78 MHz

N_2O P(30):	A:	-13034.81	B:	-13031.20
		-13035.36		-13031.73
		-13035.22		-13031.96
	Ave =	-13035.13	Ave =	-13031.63 $\Delta\nu$ = 3.5 MHz

$\nu_{P(30)} - Fq^b$ = -13035.13 MHz $\nu_{P(30)} - Fq^c$ = -13031.63 MHz

N_2O P(29)	A:	14718.90	B:	14722.76
		14718.53		14722.51
		14718.54		14722.03
	Ave =	14718.66	Ave =	14722.43 $\Delta\nu$ = 3.77 MHz

$\nu_{P(29)} - Fq^b$ = 14718.66 MHz $\nu_{P(29)} - Fq^c$ = 14722.43 MHz

---

a. Laser frequency reported in Ref. 44.

b. Laser frequency set on the top of the gain curve in A.

c. Laser frequency set on the top of the gain curve in B.

Freq. of N_2O P(29) - Freq. of N_2O P(30) =

A: (Fq^b + 14718.66) - (Fq^b - 13035.13) = 27753.79 MHz

B: (Fq^c + 14722.43) - (Fq^c - 13031.63) = 27754.06 MHz

4.3 Conclusion

It has been demonstrated that the same design considerations that led to successful implementation of infrared microwave sideband laser spectroscopy in the CO_2 laser region can be applied to the CO laser region. Even though single-transition CO laser power is generally lower than CO_2 laser power, the sideband output is more than ample for linear spectroscopy. We have in fact observed transitions with the CO laser system with laser power as low as 25 mW.

We conclude from this work that most CO laser frequencies are not known to an accuracy comparable to the ability to measure frequencies of spectroscopic transitions by the infrared microwave sideband method. Our work also shows the need for a procedure for reproducible generation of accurately known laser frequencies in the CO laser region. The data in Table VII indicate that absorption frequencies could be measured easily in favorable cases to ~1 MHz absolute accuracy by Doppler-limited linear spectroscopy in the CO region if the laser fequencies could be generated to that accuracy, as can be done easily in the CO_2 laser region. Both a routine method of stabilization and precise measurements of the laser frequencies are needed. In the meantime, it appears that the absolute accuracy of measurements of spectroscopic transitions by the

use of infrared microwave sidebands in the CO laser laser region is limited by the uncertainties in laser frequencies to ~± 10 MHz except for the recently-measured values [42], although the relative accuracy of frequencies of transitions measured with the same laser line and different microwave frequencies is considerably better, ~± 2 MHz.

Reference

1. T. Kasuya, Appl. Phys., vol. 3, pp. 223 (1974).

2. R. G. Brewer, A. Mooradian (eds.), "Laser Spectroscopy, Proceedings of the 1st Intern. Conf. Vale 1973", pp. 247, Academic Press, New York (1974).

3. E. Hirota, "Vibrational Spectra and Structure", ed. J. R. Durig, vol. 14, pp. 1-67, Elsevier Science Publishers. (1985).

4. M. Takami, J. Chem. Phys., vol. 76(4), pp. 1670-1675 (1982).

   S. Yamamoto, K. Kuchitsu, T. Nakanaga, H. Takoo, C. Matsumura, and M. Takami, J. Chem. Phys., vol. 84(11), pp. 6027-6033 (1986).

5. P. R. Griffiths, and J. A. de Haseth, "Fourier Transform Infrared Spectroscopy", Wiley, New York (1986).

6. V. J. Corcoran, J. M. Martin, and W. T. Smith, Appl. Phys. Lett., vol. 22(10), pp. 517-519 (1973).

7. G. Magerl, W. Schupita, and E. Bonek, IEEE J. Quantum Electron., vol. QE-18(8), pp. 1214-1220 (1982).

8. S. K. Lee, R. H. Schwendeman, and G. Magerl, J. Mol. Spectrosc., vol. 117, pp. 416-434 (1986).

9. H. Sasada, and R. H. Schwendeman, J. Mol. Spectrosc., vol. 117, pp. 331-341 (1986).

10. S. K. Lee, R. H. Schwendeman and R. L. Crownover, D. D. Skatrud, F. C. De Lucia, J. Mol. Spectrosc., vol. 123, pp. 145-160 (1987).

11. G. Magerl, J. M. Frye, W. A. Kreiner, and T. Oka, Appl. Phys. Lett., vol. 42(8), pp. 656-658 (1983).

12. G. Magerl, W. Schupita, J. M. Frye, W. A. Kreiner, and T. Oka, J. Mol. Spectrosc., vol. 107, pp. 72-83 (1984).

13. Y.-T. Chen, J. M. Frye, and T. Oka, J. Opt. Soc. Am. B, vol. 3(7), pp. 935-939 (1986).

14. F. Scappini, W. A. Kreiner, J. M. Frye, and T. Oka, J. Mol. Spectrosc., vol. 106, pp. 436-440 (1984).

15. L. Jörissen, W. A. Kneiner, Y.-T. Chen, and T. Oka, J. Mol. Spectrosc., vol. 120, pp. 233-235 (1986).

16. E. J. Danielewicz, and P. D. Coleman: Appl. Opt., vol. 13, pp. 1164 (1974).

17. G. M. Carter, Appl. Phys. Lett., vol. 32(12), pp. 810-812 (1978).

18. G. R. Fowles, "Introduction to Modern Optics", 2nd ed. Holt, Rinehart and Winston, Inc. New York (1975).

19. M. Born and E. Wolf, "Principles of Optics", Macmillan, New York (1964).

20. A. Yariv, "Quantum Electronics", 2nd ed., John Wiley & Sons, Inc., New York (1975).

21. S. Namba, J. Opt. Soc. Am., vol. 51(1), pp. 76-79 (1961).

22. N. McAvoy, J. Osmundson, and G. Schiffner, Appl. Opt., vol. 11, pp. 473-474, (1972).

23. I. P. Kaminow, and J. Liu, Proceedings of the IEEE, pp. 132-136 (1963).

24. W. Demtröder, "Laser Spectroscopy", Springer-Verlag Berlin Heidelberg New York (1981).

25. G. Magerl and E. Bonek, presented at the Int. Conf. on Lasers '79. Dec. 17~21, 1979, Orlando, FL.

26. A. F. Harvey, "Microwave Engineering", Academic Press London and New York, (1963).

27. F. Legay and N. Legay-Sommaire, Compt. Rend. Hebd. Séances Acad. Sci. A259, pp. 99 (1964).

28. C. K. N. Patel and R. J. Kerl, Appl. Phys. Lett. vol 5, pp. 81 (1964).

29. M. L. Bhaumik, in "High-Power Gas Lasers", ed. by E. R. Pike (The Institute of Physics, Bristol and London, 1975) pp. 122-147.

30. O. Svelto, "Principles of Lasers", 2nd ed. pp. 232 (1982).

31. R. E. Center, "High Power, Efficient Electrically Excited CO Laser". pp. 95, in Laser Handbook, edited by M. L. Stitch, North-Holland Publishing Company (1979).

32. C. Freed, Appl. Phys. Lett., vol. 18, 458-461 (1971).

33. M. Rabb, S.-C. Hsu, and R. H. Schwendeman, in preparation.

34. W. H. Weber, P. D. Maker, J. W. C. Johns and E. Weinberger, J. Mol. Spectrosc., vol. 121, pp. 243-260 (1987).

35. J. S. Wells, A. Hinz, and A. G. Maki, J. Mol. Spectrosc., vol. 114, pp. 84-96, (1985).

36. J. S. Wells, D. A. Jennings, A. Hinz, J. S. Murray, and A. G. Maki, J. Opt. Soc., Am. B., vol. 2, pp. 857-861 (1985).

37. J. S. Wells, F. R. Peterson, and A. G. Maki, J. Mol. Spectrosc., vol. 98, pp. 404-412 (1983).

38. C. Freed and A. Javan, Appl. Phys. Lett., vol. 17, pp. 53-56 (1970).

39. C. Freed and H. A. Haus, IEEE, J. Quantum Elecron., vol. QE-9(2), (1973).

40. M. Schneider, A. Hinz, A. Groh, K. M. Evenson, and W. Urban, Appl. Phys. B., vol. 44, pp. 241-245 (1987).

41. W. H. Weber and R. W. Terhune, J. Chem. Phys., vol. 78(11), pp. 6422-6436 (1983).

42. M. Schneider and K. M. Evanson, private communication.

43. R. M. Dale, M. Herman, J. W. C. Johns, A. R. W. McKellar, S. Nagler, and I. K. M. Stathy, Canad. J. Phys. vol. 57, pp. 677-686 (1979).

44. G. Guelachvili, D. de Villeneuve, R. Farrenq, W. Urban, and J. Verges, J. Mol. Spectrosc., vol. 98, pp. 64-79 (1983).

PART II

LINEAR AND NONLINEAR SPECTROSCOPIC APPLICATIONS OF THE MICROWAVE MODULATED INFRARED SIDEBAND LASER IN THE CO LASER REGION

LINEAR SPECTROSCOPIC APPLICATION

Infrared Spectrum of the ν_2 Band of D_2CO.

The use of an electrooptic modulator (CdTe crystal) for generation of tunable microwave modulated sidebands on infrared laser radiation, which was developed originally by Magerl et al. in Vienna for the CO_2 laser region [1], has been extended to the 5 - 6 μm region with a home-built CO laser in our laboratory [2]. In the first part of this dissertation the theory, experimental setup, and the performance of the new sideband laser spectrometer have been discussed in detail. With high signal-to-noise ratio (shown by the good lineshape of a molecular transition), with absolute frequency accuracy within ± 10 MHz (which is mainly limited by the knowledge of the CO laser transition frequency) and with reproducibility within ~± 4 MHz (subject to the reproducibility of the laser gain curve), this new system has shown its power as a useful tunable infrared laser source.

Through the use of a stabilization scheme to adjust the laser frequency to stay at the top of the laser gain curve, and with the sideband modulator operated in the traveling wave mode, this new tunable laser system has been applied to a Doppler-limited, linear spectroscopic study of the ν_2 band (CO stretch) of D_2CO.

1. Introduction

The ν_2 band of D_2CO was one of the first infrared bands to be studied by the technique of infrared laser Stark spectroscopy in the CO laser region [3]. In the paper by Johns and McKellar the band center and the rotational constants for the $v_2 = 1$ state were determined from precise measurements of Stark-shifted transitions of relatively low J and K_a [3]. It was not possible from the transitions measured to determine centrifugal distortion constants of either state; therefore, the ground state constants were constrained in the fitting to the calculated values from the previously-reported microwave data [4,5] and the centrifugal distortion constants in the $v_2 = 1$ state were assumed to be the same as in the ground state. The ν_2 band has also been studied previously by conventional infrared spectroscopy, but at relatively low resolution [6 - 8].

Rotational spectra in the ground and $v_2 = 1$ vibrational states of D_2CO have been described [4,5,9 - 11]. The most recent reports are of a comprehensive study of millimeter wave spectra by Dangoisse et al. [11] and of microwave measurements of $\Delta K = 2$ transitions by Chu et al. [5]. The latter work provided useful data for the A rotational constant of this near symmetric top molecule. For the $v_2 = 1$ state, only five rotational frequencies have been reported [4]. In addition to these reports of pure

rotational spectra, high-resolution infrared studies of the ν_3, ν_4, and ν_6 bands in the 10 μm region [12] and of the ν_1 and ν_5 bands in the 5 μm region [13] have each been used to obtain combination differences for the ground state which have been combined with the rotational frequencies to obtain precise ground state constants. The constants obtained from these analyses are all in very good agreement with one another.

In the present study 38 CO laser transitions were used with three different CO isotopes [Table I] in the frequency range from 1666 cm^{-1} to 1759 cm^{-1}. More than 150 infrared transitions have been recorded including transitions with J and K_a values as high as 36 and 11, respectively. These data have been combined with the previous microwave and millimeter wave results and fit to a Hamiltonian that includes rotational and fourth and sixth order centrifugal distortion constants for the ground and v_2 = 1 states. In the next section the necessary theory is outlined; in subsequent sections the experiment is described briefly and the measured frequencies and derived parameters are presented; in the final section the results are summarized and discussed.

Table I.

Carbon Monoxide Laser Lines[a] Used for the Measurement of ν_2 Band of D_2CO

Isotope	Transition	Wavenumber(cm^{-1})	Frequency(GHz)	Wavelength(μm)
C12O16	v=17 TO 16 P(14)	1679.29067	50343.86765	5.95490
C12O16	v=17 TO 16 P(12)	1686.70978	50566.28697	5.92870
C12O16	v=16 TO 15 P(18)	1688.75973	50627.74307	5.92151
C12O16	v=17 TO 16 P(11)	1690.36966	50676.00764	5.91587
C12O16	v=16 TO 15 P(17)	1692.65144	50744.41365	5.90789
C12O16	v=16 TO 15 P(16)	1696.51072	50860.11173	5.89445
C12O16	v=16 TO 15 P(13)	1707.89244	51201.32736	5.85517
C12O16	v=16 TO 15 P(12)	1711.62050	51313.09181	5.84242
C12O16	v=15 TO 14 P(18)	1713.54476	51370.77949	5.83586
C12O16	v=15 TO 14 P(16)	1721.36586	51605.25010	5.80934
C12O16	v=15 TO 14 P(15)	1725.22759	51721.02196	5.79634
C12O16	v=15 TO 14 P(14)	1729.05659	51835.81238	5.78350
C12O16	v=15 TO 14 P(13)	1732.85270	51949.61699	5.77083
C12O16	v=15 TO 14 P(12)	1736.61578	52062.43141	5.75833
C12O16	v=14 TO 13 P(18)	1738.41382	52116.33524	5.75237
C12O16	v=14 TO 13 P(17)	1742.37566	52235.10824	5.73929
C12O18	v=16 TO 15 P(16)	1666.34432	49955.74600	6.00116
C12O18	v=16 TO 15 P(14)	1673.60447	50173.39987	5.97513
C12O18	v=16 TO 15 P(13)	1677.18872	50280.85279	5.96236
C12O18	v=15 TO 14 P(17)	1686.34790	50555.43805	5.92997
C12O18	v=15 TO 14 P(15)	1693.73399	50776.86760	5.90411
C12O18	v=15 TO 14 P(11)	1708.13944	51208.73213	5.85432
C12O18	v=15 TO 14 P(10)	1711.66363	51314.38458	5.84227
C12O18	v=14 TO 13 P(16)	1713.84581	51379.80485	5.83483
C12O18	v=14 TO 13 P(14)	1721.23623	51601.36413	5.80978
C12O18	v=14 TO 13 P(13)	1724.88559	51710.76914	5.79749
C12O18	v=14 TO 13 P(12)	1728.50421	51819.25245	5.78535
C12O18	v=14 TO 13 P(11)	1732.09194	51926.81009	5.77337
C12O18	v=14 TO 13 P(10)	1735.64867	52033.43808	5.76153
C12O18	v=13 TO 12 P(16)	1737.71274	52095.31727	5.75469
C12O18	v=13 TO 12 P(15)	1741.45577	52207.53048	5.74232
C12O18	v=13 TO 12 P(14)	1745.16831	52318.82973	5.73011
C12O18	v=12 TO 11 P(19)	1750.14757	52468.10408	5.71380
C12O18	v=13 TO 12 P(12)	1752.50141	52538.67045	5.70613
C12O18	v=12 TO 11 P(18)	1754.01387	52584.01280	5.70121
C12O18	v=13 TO 12 P(10)	1759.71097	52754.80768	5.68275
C13O16	v=14 TO 13 P(13)	1727.44684	51787.55331	5.78889
C13O16	v=13 TO 12 P(15)	1744.07746	52286.12695	5.73369

a. Values calculated from constants reported in Ref. 14.

2. Theoretical Calculation of the Spectra

Molecular vibration-rotation spectra involving low rotational energy can often be understood by using the simple models of the harmonic oscillator and the rigid rotor. With the approximation that the vibration-rotation interaction is included in effective rotational constants, the vibrational Hamiltonian and the rotational Hamiltonian can be written down separately. Therefore, the wave function for nuclear motio nis approximately a product of rotational and vibrational wave functions and the vibration-rotation energy of the molecule can be treated as the sum of rotational and vibrational energies.

At the level of approximation just described, the rigid rotor Hamiltonian (in wavenumber unit) referred to its principal axes of inertia is known to be [15]

$$\hat{H}_{rigid} = B_x \hat{J}_x^2 + B_y \hat{J}_y^2 + B_z \hat{J}_z^2 \quad , \qquad (1)$$

where B_x , B_y , B_z are given by

$$B_\alpha = h/8\pi^2 c I_\alpha \quad ,$$

and I_x , I_y , I_z are the effective principal moments of inertia of the molecule. The angular momentum operator components $\hat{J}_x$, $\hat{J}_y$, $\hat{J}_z$, measured in units of $h/2\pi$, are referred to the principal axes of the rotating molecule. These axes are usually labelled as a, b, and c, when the

rotational constants are in order of decreasing magnitude $B_a \geq B_b \geq B_c$; also, the notation A, B, C instead of B_a, B_b, B_c is normally used as the standard.

For a singlet electronic state, the matrix elements of $\hat{H}_{rigid}$ may be determined for basis functions for which the allowed values of the rotational quantum numbers are J = 0, 1, 2,... and k = -J, -J+1, ... J-1, J. To facilitate the use of these matrix elements, the Hamiltonian can be rewritten as

$$\hat{H}_{rigid} = \frac{1}{2}(B_x + B_y)\hat{J}^2 + [B_z - \frac{1}{2}(B_x + B_y)]\hat{J}_z^2 + \frac{1}{4}(B_x - B_y)[(\hat{J}_x + i\hat{J}_y)^2 + (\hat{J}_x - i\hat{J}_y)^2], \quad (2)$$

for which the non-zero Hamitonian matrix elements are

$$\langle J, k|\hat{H}_{rigid}|J, k\rangle = \frac{1}{2}(B_x + B_y)J(J+1) + [B_z - \frac{1}{2}(B_x + B_y)]k^2, \quad (3)$$

and

$$\langle J, k\pm2|\hat{H}_{rigid}|J, k\rangle = \frac{1}{4}(B_x - B_y)\{[J(J+1) - k(k\pm1)] \times [J(J+1) - (k\pm1)(k\pm2)]\}^{1/2} \quad (4)$$

For a symmetric top molecule, for which $B_x = B_y$, the Hamiltonian matrix is already diagonal, and the energy levels can be given directly as

$$\hat{H}_{rigid}(J,K) = B_xJ(J+1) + (B_z-B_x)k^2 \quad .$$

However, for an asymmetric top molecule, $B_x \neq B_y \neq B_z$, and there is no general formula for the energy levels. The method usually used to obtain the energy levels of an asymmetric top molecule is the diagonalization of the Hamiltonian matrix numerically by computer. Normally, the symmetric-top wave functions are used as a convenient complete orthonormal set to obtain the Hamiltonian matrix of the asymmetric rotor since they are functions of the same coordinates and satisfy the same boundary conditions as the asymmetric-top wavefunctions.

However, in order to achieve precise agreement between the calculated values with the observed line frequencies, especially for high rotational quantum number, the rigid rotor model needs to be corrected because of the breakdown due to the distortion of the molecule by centrifugal forces. In 1977, Watson [15] provided the currently-accepted definitive treatment in which the rigid rotor model was improved by the addition of higher-order terms to the Hamiltonian [Eq. (2)]; these terms are proportional to what are known as quartic and sextic centrifugal distortion coefficients. This so-called Watson's asymmetric top "A" reduced Hamiltonian, which eliminates non-zero off-diagonal matrix elements with $| \Delta k | > 2$, is shown as

$$\hat{H}^{(A)}_{rot} = B_x \hat{J}_x^2 + B_y \hat{J}_y^2 + B_z \hat{J}_z^2 - \Delta_J (\hat{J}^2)^2 - \Delta_{JK} \hat{J}^2 \hat{J}_z^2$$

$$- \Delta_K \hat{J}_z^4 - \frac{1}{2} [\delta_J \hat{J}^2 + \delta_K \hat{J}_z^2 , \hat{J}_+^2 + \hat{J}_-^2]_+$$

$$+ \phi_J (\hat{J}^2)^3 + \phi_{JK} (\hat{J}^2)^2 \hat{J}_z^2 + \phi_{KJ} \hat{J}^2 \hat{J}_z^4 + \phi_K \hat{J}_z^6$$

$$+ \frac{1}{2} [\phi_J (\hat{J}^2)^2 + \phi_{JK} \hat{J}^2 \hat{J}_z^2 + \phi_K \hat{J}_z^4 , \hat{J}_+^2 + \hat{J}_-^2]_+, \quad (5)$$

where $\hat{J}_\pm = \hat{J}_x \pm i\hat{J}_y$, and $[\hat{A}, \hat{B}]_+$ represents the anti-commutator $\hat{A}\hat{B} + \hat{B}\hat{A}$. The Hamiltonian matrix elements are

$$H_{k,k} = \langle J, k | \hat{H}^{(A)}_{rot} | J, k \rangle = \frac{1}{2} [B_x + B_y] J(J+1)$$

$$+ \{ B_z - \frac{1}{2} [B_x + B_y] \} k^2 - \Delta_J J^2(J+1)^2$$

$$- \Delta_{JK} J(J+1)k^2 - \Delta_K k^4 + \phi_J J^3(J+1)^3 + \phi_{JK} J^2(J+1)^2 k^2$$

$$+ \phi_{KJ} J(J+1)k^4 + \phi_K k^6, \quad (6)$$

and

$$H_{k\pm2,k} = \langle J, k\pm2 | \hat{H}^{(A)}_{rot} | J, k \rangle = \{ \frac{1}{4} [B_x - B_y]$$

$$- \delta_J J(J+1) - \frac{1}{2} \delta_K [(k\pm2)^2 + k^2] + \phi_J J^2(J+1)^2$$

$$+ \frac{1}{2} \phi_{JK} J(J+1) [(k\pm2)^2 + k^2] + \frac{1}{2} \phi_k [(k\pm2)^4 + k^4] \}$$

$$x \{ [J(J+1) - k(k\pm1)] [J(J+1) - (k\pm1)(k\pm2)] \}^{1/2}. \quad (7)$$

The energies are calculated by diagonalization of the matrices constructed from these elements. The calculations were performed by the computer program "ASYMTP.FOR".

3. Fitting the Experimental Spectra

To determine the experimental spectroscopic frequencies the stored experimental intensity data for the lineshapes were fit by the method of least squares to a Gaussian function, or a sum of Gaussian functions if the lines were overlapped with the computer program "GFIT.FOR". In principle, the percent transmission should be converted to absorbancy before the fitting, but tests with a number of experimental and theoretical curves have shown that the difference in center frequency obtained by the two methods is negligible. We, therefore, use the simpler technique because it is easy to determine starting parameters for the least squares fitting when the simple Gaussian is fit. Except when two or more transitions were severely overlapped or for very weak transitions, the standard error in center frequency obtained from the fitting was always much less than the ± 5 MHz uncertainty in the laser frequency. The fitting error was therefore ignored for reasonably strong well-resolved transitions.

Theoretical frequencies of the transitions were calculated by means of a computer program "ASYMTP.FOR", that is a simplification of the program written by Dr. R. H. Schwendeman at Michigan State University for the analysis of the Coriolis-coupled spectra in the 10 μm region of D_2CO [12]. For the present spectrum, only one excited

vibrational state was involved and no coupling was required. The program calculates the frequencies from energy levels obtained by diagonalization of an asymmetric rotor Hamiltonian [Eq. (5)] including quartic and sextic centrifugal distortion constants. The Hamiltonian is written in a representation based on Watson's A reduction with a I^r axis system, $x \leftrightarrow b$, $y \leftrightarrow c$, $z \leftrightarrow a$ [15]; the elements for the energy matrices were computed by Eq. (6) and (7). The transitions are arranged in order of increasing J before submission to the least-squares fitting program "VBRFT.FOR" in order to reduce the number of derivatives that must be stored during the calculation. The least-squares fittings were performed with weights that were taken to be the square of the inverse of the estimated uncertainty of each experimental frequency.

4. Experiments

The infrared microwave sideband laser spectrometer for the CO laser region [Figure 1] has been described in detail in the previous part of this dissertation and in a recent publication [2], so only a brief description will be given here. The CO laser has a 1.2 m discharge path in a semi-sealed tube containing approximately 2.5% CO, 3.4% Xe, 18.5% N_2, and 75.6% He at a total pressure of ~16 Torr. The laser is operated with approximately 9 mA discharge current

in each of two discharge paths. The laser frequency is controlled by applying a 0.52 kHz dither to the end mirror by means of a piezoelectric translator (PZT) and by using a lock-in amplifier to process the output of a pyroelectric detector that monitors the carrier radiation. The output of the lock-in amplifier is amplified and applied to the PZT as a correction voltage. Tests shown in the previous part of this dissertation indicate that this method of frequency stabilization gives laser frequencies which are reproducible from day to day to within ± 4 MHz. The absolute frequency accuracy is ± 10 MHz, except for the few cases where the laser cannot be kept from oscillating on more than one laser line, in which case the output profile is a superposition of two modes of rather different frequency. Because the laser frequencies for reasonable v and J are well separated in the 1700 cm^{-1} region of interest in the present study, laser oscillation on two different transitions proved to be only a minor problem for this work.

The infrared microwave sidebands were generated in a CdTe electrooptic modulator crystal that is housed in a matched waveguide configuration. The crystal was operated in the "traveling wave mode" in which the microwaves were absorbed by a broad-band termination after passing through the modulator. After leaving the crystal, the modulation sidebands passed through a polarizer to remove most of the carrier and through a beamsplitter for separation into

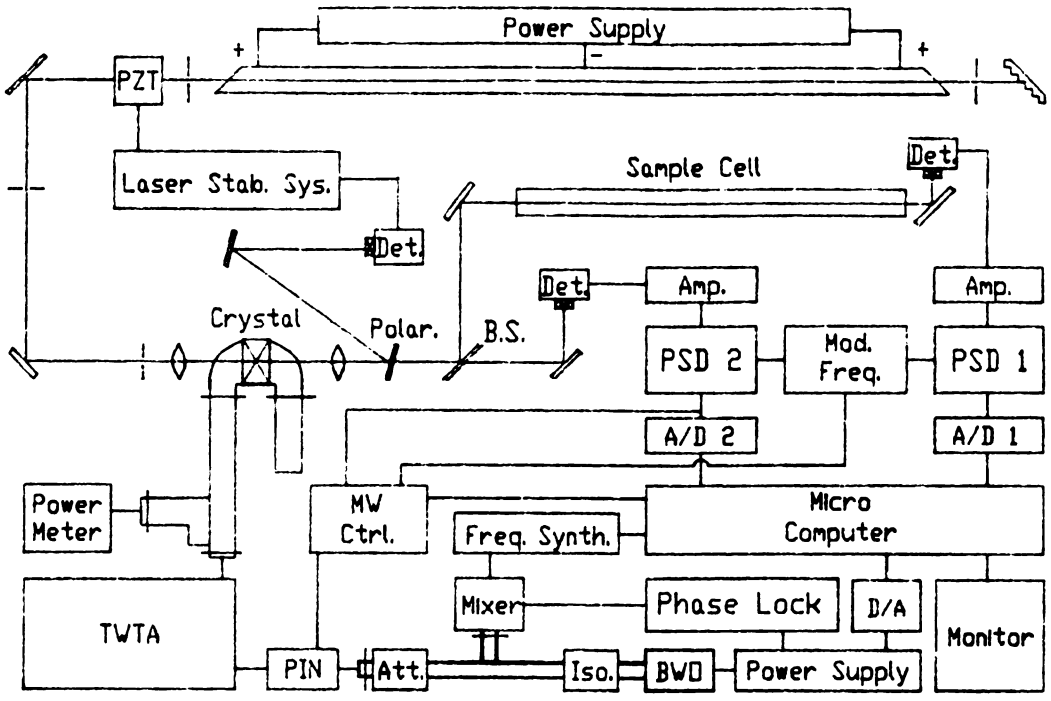

Figure 1. Block diagram of the CO microwave sideband laser spectrometer operating in the traveling wave mode for linear spectroscopic measurement.

sample and reference beams. The carrier reflected from the polarizer was used for the frequency stabilization.

The microwave power was provided by traveling-wave-tube amplification of the output from a backward wave oscillator whose frequency was phase-locked to a harmonic of a computer-controlled radio frequency synthesizer. The microwaves were chopped at 10 kHz by a PIN diode whose attenuation during the "on" portion of the chopping cycle was continuously adjusted by means of a feedback loop to give constant sideband power at the reference detector. As a result of the amplitude stabilization provided by the feedback, typical spectra [Figures 2 - 4] show an almost flat background. Both the sample and reference spectra were obtained by processing the outputs of HgCdTe photoconductive detectors by means of lock-in amplifiers tuned to 10 kHz. The spectrometer was operated under the control of a minicomputer which stepped the microwave frequency and recorded the spectra.

The D_2CO sample was obtained from Merck as deuterated paraformaldehyde. The bulb containing the sample was warmed to ~100 ^{o}C in a mineral oil bath in order to generate the monomer, which was allowed to diffuse into a sample cell that consisted of a 1-meter glass tube with NaCl windows. Sample pressures, which were 0.1 - 0.5 Torr, were estimated with a thermocouple-type gauge.

The laser frequencies for this work were obtained from

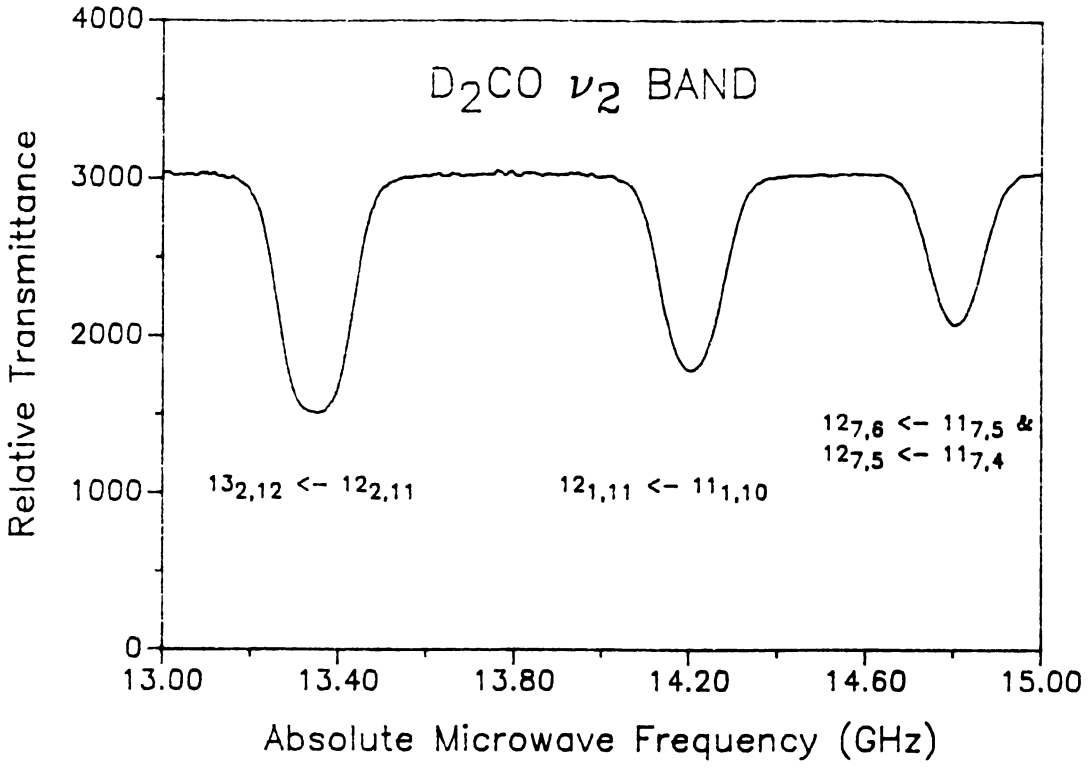

Figure 2. Portion of the spectrum of the ν_2 band of D_2CO taken with the infrared microwave sideband laser spectrometer in the CO laser region. The vertical axis is relative transmittance; the horizontal axis is the microwave frequency to be added to or subtracted from the frequency of the $^{12}C^{18}O$ 14 to 13 P(13) laser line to obtain the infrared frequency. The $^{13}_{2,12} \leftarrow {}^{12}_{2,11}$ transition absorbed the positive sideband whereas the other three transitions absorbed the negative sideband.

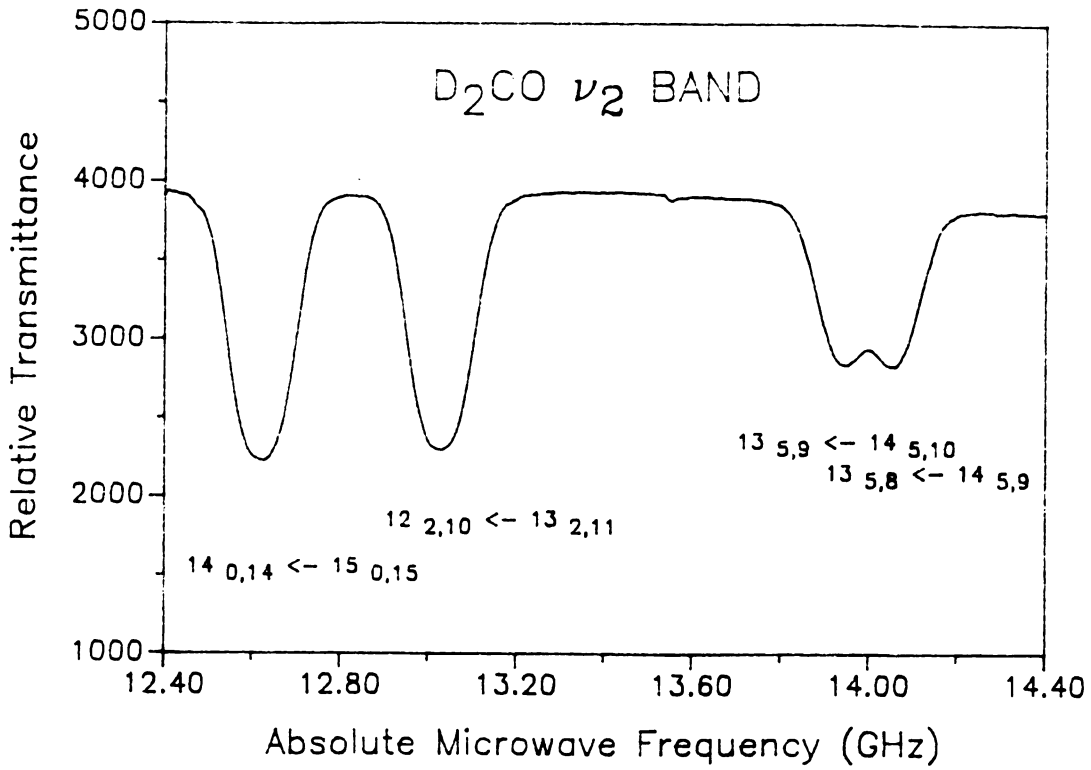

Figure 3. Portion of the spectrum of the ν_2 band of D_2CO taken with the infrared microwave sideband laser spectrometer in the CO laser region. The vertical axis is relative transmittance; the horizontal axis is the microwave frequency to be added to or subtracted from the frequency of the $^{12}C^{18}O$ 16 to 15 P(14) laser line to obtain the infrared frequency. The $^{12}_{2,10} \leftarrow {}^{13}_{2,11}$ transition absorbed the positive sideband whereas the other three transitions absorbed the negative sideband.

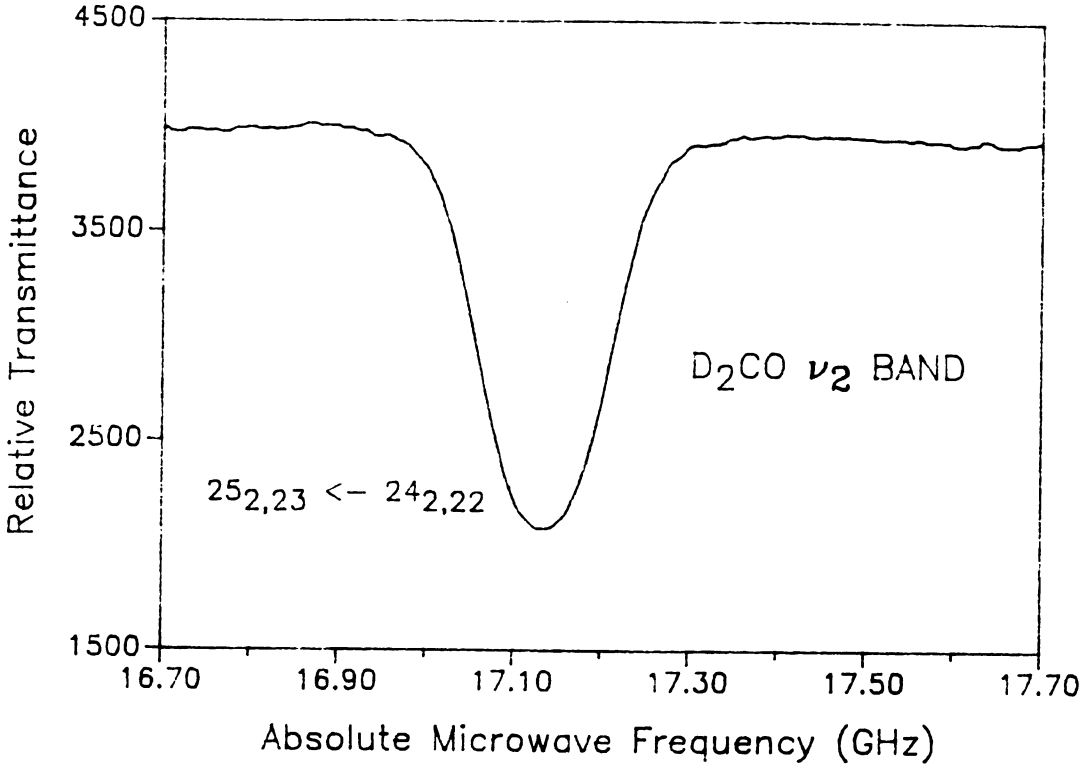

Figure 4. Recording of a single transition $25_{2,23} \leftarrow 24_{2,22}$ in the spectrum of the ν_2 band of D_2CO taken with the infrared microwave sideband laser spectrometer in the CO laser region. The vertical axis is relative transmittance; the horizontal axis is the microwave frequency (17135.4 GHz) to be added to the frequency of the $^{12}C^{18}O$ 13 to 12 P(14) laser line to obtain the infrared frequency.

the report of Guelachvili et al. [14]. The microwave frequencies were determined from the RF reference frequencies, which were in turn frequently intercompared and measured by two different electronic counters.

5. Experimental Results and Discussion

The frequencies of the assigned infrared transitions in the ν_2 band of D_2CO are listed with their estimated uncertainties in Table II. At first, the uncertainties of well-resolved infrared transitions were assumed to be ± 10 MHz. Analysis of the standard deviations of the fittings indicated that the random error in the frequencies was less than half this value and as a result, the uncertainties of resolved transitions were reduced to ± 5 MHz with a corresponding reduction in uncertainty for the unresolved transitions. The measured infrared frequencies were combined with the rotational frequencies and uncertainties for ground state transitions reported in Table V of Ref. 11 and the five $v_2 = 1$ transitions given in Table III of Ref. 4 and fit to energy levels calculated by the method described in the previous section. We did not use the precise infrared data in Ref. 3 because our fitting program does not include provision for inclusion of Stark effect data. Several least squares adjustments of parameters were carried out and the resulting parameters for two of them are

Table II.

Comparison of Observed and Calculated Wavenumbers for the ν_2 Band of D_2CO

J'	k'_a,k'_c	J"	k''_a,k''_c	Laser Line[a]	MW Freq.[b]	ν_{obs}[c]	O-C[d]	Unc.[e]	Fit[f]
16	7,10	17	7,11	16-15 P(16)β	17086.1	1666.91425	-3	33	
16	7, 9	17	7,10	16-15 P(16)β	17086.1	1666.91425	0	33	
13	3,11	14	3,12	16-15 P(14)β	-16928.9	1673.03978	-3	16	
13	5, 8	14	5, 9	16-15 P(14)β	-14061.0	1673.13545	-8	33	
13	5, 9	14	5,10	16-15 P(14)β	-13933.2	1673.13971	11	33	
14	0,14	15	0,15	16-15 P(14)β	-12620.1	1673.18351	-5	16	
14	1,14	15	1,15	16-15 P(14)β	-10622.4	1673.25015	-12	16	
13	6, 8	14	6, 9	16-15 P(14)β	-9606.0	1673.28405	-12	33	
13	6, 7	14	6, 8	16-15 P(14)β	-9606.0	1673.28405	0	33	
13	10, 4	14	10, 5	16-15 P(14)β	8996.1	1673.90455	39	33	Z
13	10, 3	14	10, 4	16-15 P(14)β	8996.1	1673.90455	39	33	Z
12	2,10	13	2,11	16-15 P(14)β	13028.7	1674.03906	0	16	
13	11, 3	14	11, 4	16-15 P(14)β	14567.1	1674.09038	33	33	Z
13	11, 2	14	11, 3	16-15 P(14)β	14567.1	1674.09038	33	33	Z
11	1,10	12	1,11	16-15 P(13)β	-9053.6	1676.88672	-13	16	
11	3, 8	12	3, 9	16-15 P(13)β	-8797.2	1676.89528	4	16	
11	6, 6	12	6, 7	16-15 P(13)β	11089.2	1677.55862	0	33	
11	6, 5	12	6, 6	16-15 P(13)β	11089.2	1677.55862	1	33	
11	7, 5	12	7, 6	16-15 P(13)β	14990.9	1677.68876	8	33	
11	7, 4	12	7, 5	16-15 P(13)β	14990.9	1677.68876	8	33	
11	2,10	12	2,11	16-15 P(13)β	16633.8	1677.74356	9	16	
11	0,11	12	0,12	17-16 P(14)α	-13129.2	1678.85273	-5	16	
10	1, 9	11	1,10	17-16 P(14)α	-12194.0	1678.88392	-40	33	
10	6, 5	11	6, 6	17-16 P(14)α	11414.3	1679.67141	-13	33	
10	6, 4	11	6, 5	17-16 P(14)α	11414.3	1679.67141	-13	33	
10	2, 9	11	2,10	17-16 P(14)α	13838.4	1679.75227	21	16	
10	7, 4	11	7, 5	17-16 P(14)α	15180.9	1679.79705	9	33	
10	7, 3	11	7, 4	17-16 P(14)α	15180.9	1679.79705	9	33	
7	2, 6	8	2, 7	15-14 P(17)β	-17049.8	1685.77918	12	16	
7	5, 3	8	5, 4	15-14 P(17)β	-16020.8	1685.81350	7	33	
7	5, 2	8	5, 3	15-14 P(17)β	-16020.8	1685.81350	9	33	
7	6, 2	8	6, 3	15-14 P(17)β	-12952.8	1685.91584	-5	33	
7	6, 1	8	6, 2	15-14 P(17)β	-12952.8	1685.91584	-5	33	
7	0, 7	8	0, 8	17-16 P(12)α	-13550.2	1686.25779	-1	16	
6	1, 5	7	1, 6	17-16 P(12)α	11590.5	1687.09640	21	33	

Table II (cont'd.).

J'	k'_a,k'_c	J"	k''_a,k''_c	Laser Line[a]	MW Freq.[b]	ν_{obs}[c]	O-C[d]	Unc.[e]	Fit[f]
5	1, 4	6	1, 5	16-15 P(18)α	12617.9	1689.18062	27	16	
5	2, 4	6	2, 5	17-16 P(11)α	-17441.5	1689.78787	-6	16	
5	4, 2	6	4, 3	17-16 P(11)α	-16395.8	1689.82275	-11	33	
5	4, 1	6	4, 2	17-16 P(11)α	-16395.8	1689.82275	4	33	
5	5, 1	6	5, 2	17-16 P(11)α	-13904.8	1689.90584	-12	33	
5	5, 0	6	5, 1	17-16 P(11)α	-13904.8	1689.90584	-12	33	
5	0, 5	6	0, 6	17-16 P(11)α	-11220.4	1689.99539	-45	33	
4	1, 4	5	1, 5	16-15 P(17)α	-10830.2	1692.29018	-13	33	
3	1, 2	4	1, 3	15-14 P(15)β	-11409.8	1693.35340	2	16	
3	1, 3	4	1, 4	15-14 P(15)β	13131.2	1694.17200	8	16	
15	3,13	15	3,12	16-15 P(16)α	14378.7	1696.99034	21	16	
6	1, 6	6	1, 5	16-15 P(16)α	17872.6	1697.10689	31	33	
3	0, 3	2	0, 2	16-15 P(13)α	-16053.9	1707.35694	5	16	
3	2, 2	2	2, 1	16-15 P(13)α	-14119.9	1707.42145	5	16	
3	2, 1	2	2, 0	16-15 P(13)α	-13152.5	1707.45372	-8	16	
3	1, 2	2	1, 1	15-14 P(11)β	-13365.0	1707.69363	-16	33	
8	1, 7	8	1, 8	16-15 P(13)α	13758.8	1708.35139	38	50	
5	2, 4	4	2, 3	16-15 P(12)α	-13149.2	1711.18189	-6	16	
5	3, 3	4	3, 2	15-14 P(10)β	-11951.3	1711.26498	-16	33	
5	3, 2	4	3, 1	15-14 P(10)β	-11810.1	1711.26969	27	33	
5	4, 2	4	4, 1	15-14 P(10)β	-10513.6	1711.31293	6	33	
5	4, 1	4	4, 0	15-14 P(10)β	-10513.6	1711.31293	3	33	
5	2, 3	4	2, 2	15-14 P(10)β	-9716.4	1711.33953	3	16	
6	2, 5	5	2, 4	15-14 P(18)α	-15358.6	1713.03245	-8	16	
6	3, 4	5	3, 3	15-14 P(18)α	-11937.9	1713.14655	-17	33	
6	3, 3	5	3, 2	15-14 P(18)α	-11602.2	1713.15775	-27	33	
6	4, 3	5	4, 2	15-14 P(18)α	-10620.2	1713.19051	18	50	
6	4, 2	5	4, 1	15-14 P(18)α	-10620.2	1713.19051	2	50	
6	5, 2	5	5, 1	14-13 P(16)β	-17749.7	1713.25374	-17	33	
6	5, 1	5	5, 0	14-13 P(16)β	-17749.7	1713.25374	-17	33	
6	2, 4	5	2, 3	14-13 P(16)β	-16354.1	1713.30030	-13	16	
7	1, 7	6	1, 6	15-14 P(18)α	16995.8	1714.11168	14	16	
10	6, 4	9	6, 3	14-13 P(14)β	-16042.4	1720.70111	-3	33	
10	3, 7	9	3, 6	14-13 P(14)β	-16042.4	1720.70111	-25	33	
10	7, 4	9	7, 3	15-14 P(16)α	-17266.3	1720.78992	18	50	

Table II (cont'd.).

J'	k'_a,k'_c	J"	k''_a,k''_c	Laser Line[a]	MW Freq.[b]	ν_{obs}[c]	O-C[d]	Unc.[e]	Fit[f]
10	7, 3	9	7, 2	15-14 P(16)α	-17266.3	1720.78992	18	50	
11	1,11	10	1,10	14-13 P(14)β	-13363.7	1720.79046	-58	50	
10	8, 3	9	8, 2	14-13 P(14)β	-10168.1	1720.89706	-9	33	
10	8, 2	9	8, 1	14-13 P(14)β	-10168.1	1720.89706	-9	33	
10	1, 9	9	1, 8	15-14 P(16)α	-11785.3	1720.97274	-30	33	
11	0,11	10	0,10	15-14 P(16)α	-11480.1	1720.98292	-16	33	
11	2,10	10	2, 9	15-14 P(16)α	17266.3	1721.94180	-44	50	
12	6, 7	11	6, 6	14-13 P(13)β	-17188.1	1724.31226	-21	33	
12	6, 6	11	6, 5	14-13 P(13)β	-17188.1	1724.31226	-23	33	
12	7, 6	11	7, 5	14-13 P(13)β	-14806.5	1724.39170	-14	33	
12	7, 5	11	7, 4	14-13 P(13)β	-14806.5	1724.39170	-14	33	
12	1,11	11	1,10	14-13 P(13)β	-14206.5	1724.41171	-14	16	
12	8, 5	11	8, 4	14-13 P(13)β	-11787.2	1724.49241	1	33	
12	8, 4	11	8, 3	14-13 P(13)β	-11787.2	1724.49241	1	33	
12	3, 9	11	3, 8	14-13 P(13)β	-11243.3	1724.51055	14	16	
12	10, 3	11	10, 2	15-14 P(15)α	-14400.2	1724.74725	6	33	Z
12	10, 2	11	10, 1	15-14 P(15)α	-14400.2	1724.74725	6	33	Z
13	2,12	12	2,11	14-13 P(13)β	13348.1	1725.33084	0	16	
14	1,14	13	1,13	15-14 P(15)α	11062.1	1725.59658	46	33	
14	0,14	13	0,13	15-14 P(15)α	13495.0	1725.67774	17	16	
13	2,11	12	2,10	14-13 P(13)τ	-16468.4	1726.89751	14	16	
14	6, 9	13	6, 8	14-13 P(13)τ	12944.0	1727.87860	23	33	
14	6, 8	13	6, 7	14-13 P(13)τ	12944.0	1727.87860	13	33	
14	4,10	13	4, 9	14-13 P(12)β	-17766.8	1727.91157	-4	16	
14	7, 8	13	7, 7	14-13 P(13)τ	14953.5	1727.94563	10	33	
14	7, 7	13	7, 6	14-13 P(13)τ	14953.5	1727.94563	10	33	
14	8, 7	13	8, 6	14-13 P(12)β	-13997.5	1728.03730	4	33	
14	8, 6	13	8, 5	14-13 P(12)β	-13997.5	1728.03730	4	33	
14	9, 6	13	9, 5	14-13 P(12)β	-10641.7	1728.14924	9	50	
14	9, 5	13	9, 4	14-13 P(12)β	-10641.7	1728.14924	9	50	
15	2,14	14	2,13	15-14 P(14)α	-13197.3	1728.61637	6	16	
16	1,16	15	1,15	15-14 P(14)α	-10208.9	1728.71606	-13	16	
14	2,12	13	2,11	15-14 P(14)α	-9893.4	1728.72658	-14	16	
16	0,16	15	0,15	15-14 P(14)α	-8952.4	1728.75797	-14	16	
15	3,13	14	3,12	15-14 P(14)α	11037.8	1729.42477	-2	16	

Table II (cont'd.).

J'	k'_a,k'_c	J"	k''_a,k''_c	Laser Line[a]	MW Freq.[b]	ν_{obs}[c]	O-C[d]	Unc.[e]	Fit[f]
15	4,12	14	4,11	15-14 P(14)α	16799.6	1729.61696	-56	66	
15	5,11	14	5,10	15-14 P(14)α	16905.3	1729.62049	-16	66	
15	5,10	14	5, 9	15-14 P(14)α	17125.0	1729.62782	27	33	
15	6,10	14	6, 9	15-14 P(14)α	17643.2	1729.64510	40	33	
15	6, 9	14	6, 8	15-14 P(14)α	17643.2	1729.64510	17	33	
16	8, 9	15	8, 8	14-13 P(11)β	-16774.2	1731.53241	4	33	
16	8, 8	15	8, 7	14-13 P(11)β	-16774.2	1731.53241	4	33	
16	4,12	15	4,11	14-13 P(11)β	-15811.3	1731.56453	-2	16	
16	9, 8	15	9, 7	14-13 P(11)β	-13679.6	1731.63564	0	50	
16	9, 7	15	9, 6	14-13 P(11)β	-13679.6	1731.63564	0	50	
17	5,12	16	5,11	15-14 P(13)α	9363.0	1733.16502	17	50	
17	7,11	16	7,10	15-14 P(13)α	10030.2	1733.18727	-4	33	
17	7,10	16	7, 9	15-14 P(13)α	10030.2	1733.18727	-7	33	
18	9,10	17	9, 9	14-13 P(10)β	-17316.2	1735.07106	-15	50	
18	9, 9	17	9, 8	14-13 P(10)β	-17316.2	1735.07106	-15	50	
19	1,18	18	1,17	14-13 P(10)β	-14514.5	1735.16452	-10	16	
18	10, 9	17	10, 8	14-13 P(10)β	-13808.9	1735.18805	298	33	Z
18	10, 8	17	10, 7	14-13 P(10)β	-13808.9	1735.18805	298	33	Z
19	3,17	18	3,16	14-13 P(10)β	13211.4	1736.08935	6	16	
21	1,21	20	1,20	15-14 P(12)α	-10585.6	1736.26268	-37	33	
21	0,21	20	0,20	15-14 P(12)α	-10368.5	1736.26992	15	33	
19	4,15	18	4,14	15-14 P(12)α	14480.1	1737.09878	11	16	
19	2,17	18	2,16	15-14 P(12)α	15995.2	1737.14932	13	33	
21	2,20	20	2,19	14-13 P(18)α	-15030.2	1737.91247	-10	33	
21	1,20	20	1,19	13-12 P(16)β	10619.5	1738.06697	2	16	
20	4,17	19	4,16	13-12 P(16)β	16762.6	1738.27188	51	50	
20	4,16	19	4,15	14-13 P(18)α	16375.6	1738.96005	0	33	
23	1,22	22	1,21	13-12 P(15)β	-15500.2	1740.93874	-3	16	
22	5,18	21	5,17	13-12 P(15)β	8867.1	1741.75155	-1	16	
22	9,14	21	9,13	13-12 P(15)β	10041.6	1741.79072	-62	33	Z
22	9,13	21	9,12	13-12 P(15)β	10041.6	1741.79072	-63	33	Z
22	10,13	21	10,12	14-13 P(17)α	-14521.5	1741.89128	774	33	Z
22	10,12	21	10,11	13-12 P(15)β	13056.4	1741.89129	775	33	Z
22	5,17	21	5,16	14-13 P(17)α	-12947.3	1741.94378	-1	16	
22	11,12	21	11,11	13-12 P(15)β	16291.6	1741.99920	222	33	Z

Table II (cont'd.).

J'	k'_a,k'_c	- J"	k''_a,k''_c	Laser Line[a]	MW Freq.[b]	ν_{obs}[c]	O-C[d]	Unc.[e]	Fit[f]
22	11,11	- 21	11,10	13-12 P(15)β	16291.6	1741.99920	222	33	Z
25	1,25	- 24	1,24	14-13 P(17)α	-9463.0	1742.06001	90	50	
25	0,25	- 24	0,24	14-13 P(17)α	-9463.0	1742.06001	-48	50	
22	4,18	- 21	4,17	14-13 P(17)α	9197.0	1742.68244	1	33	
23	10,14	- 22	10,13	13-12 P(15)τ	-16247.4	1743.53551	954	33	Z
23	10,13	- 22	10,12	13-12 P(15)τ	-16247.4	1743.53551	954	33	Z
23	4,19	- 22	4,18	13-12 P(15)τ	13443.0	1744.52587	6	16	
23	3,20	- 22	3,19	13-12 P(14)β	-16084.3	1744.63179	-2	16	
24	4,21	- 23	4,20	13-12 P(14)β	-11259.6	1744.79273	-18	16	
27	0,27	- 26	0,26	13-12 P(14)β	-8674.2	1744.87897	-35	33	
27	1,27	- 26	1,26	13-12 P(14)β	-8674.2	1744.87897	27	33	
24	5,19	- 23	5,18	13-12 P(14)β	9198.3	1745.47513	-20	16	
25	2,23	- 24	2,22	13-12 P(14)β	17135.4	1745.73988	-2	16	
28	2,26	- 27	2,25	12-11 P(19)β	-11139.4	1749.77600	-5	16	
26	4,22	- 25	4,21	12-11 P(19)β	-8427.1	1749.86647	-3	16	
27	3,24	- 26	3,23	12-11 P(19)β	13501.4	1750.59793	21	16	
30	2,29	- 29	2,28	12-11 P(19)β	15752.1	1750.67300	9	16	
30	1,29	- 29	1,28	12-11 P(19)β	15979.8	1750.68060	11	16	
28	3,25	- 27	3,24	13-12 P(12)β	-16302.8	1751.95761	11	16	
31	2,30	- 30	2,29	13-12 P(12)β	-14430.7	1752.02005	-7	33	
31	1,30	- 30	1,29	13-12 P(12)β	-14270.0	1752.02541	3	33	
33	1,33	- 32	1,32	13-12 P(12)β	15669.7	1753.02409	13	33	
33	0,33	- 32	0,32	13-12 P(12)β	15669.7	1753.02409	8	33	
29	9,21	- 28	9,20	13-12 P(12)β	17153.3	1753.07358	-240	33	Z
29	9,20	- 28	9,19	13-12 P(12)β	17153.3	1753.07358	-249	33	Z
29	8,22	- 28	8,21	13-12 P(12)β	17424.3	1753.08262	88	50	
29	8,21	- 28	8,20	13-12 P(12)β	17424.3	1753.08262	-89	50	
29	5,25	- 28	5,24	13-12 P(12)β	17567.8	1753.08741	16	50	
29	6,23	- 28	6,22	12-11 P(18)β	-15530.4	1753.49583	-12	50	
31	3,29	- 30	3,28	12-11 P(18)β	-10472.2	1753.66455	-13	16	
34	1,34	- 33	1,33	12-11 P(18)β	9642.6	1754.33551	-8	33	
34	0,34	- 33	0,33	12-11 P(18)β	9642.6	1754.33551	-11	33	
29	5,24	- 28	5,23	12-11 P(18)β	11631.3	1754.40185	3	16	
30	3,27	- 29	3,26	12-11 P(18)β	16496.6	1754.56414	21	50	
30	5,26	- 29	5,25	12-11 P(18)β	17876.4	1754.61016	-69	50	

Table II (cont'd.).

J'	k'_a,k'_c	- J"	k''_a,k''_c	Laser Line[a]	MW Freq.[b]	ν_{obs}[c]	O-C[d]	Unc.[e]	Fit[f]
35	1,34	- 34	1,33	12-11 P(17)β	-17188.9	1757.27671	-62	50	
35	2,34	- 34	2,33	12-11 P(17)β	-17188.9	1757.27671	53	50	
32	4,28	- 31	4,27	13-12 P(10)β	-16410.4	1759.16358	-15	16	
34	4,31	- 33	4,30	13-12 P(10)β	-15227.2	1759.20305	12	16	
33	9,24	- 32	9,23	13-12 P(10)β	-13667.9	1759.25506	-469	33	Z
33	9,25	- 32	9,24	13-12 P(10)β	-13667.9	1759.25506	-395	33	Z
33	10,23	- 32	10,22	13-12 P(10)β	-13562.2	1759.25858	669	33	Z
33	10,24	- 32	10,23	13-12 P(10)β	-13562.2	1759.25858	673	33	Z
36	3,34	- 35	3,33	13-12 P(10)β	14468.8	1760.19360	-2	33	
36	2,34	- 35	2,33	13-12 P(10)β	15001.9	1760.21138	-4	16	
33	6,27	- 32	6,26	13-12 P(10)β	17382.0	1760.29077	6	16	

a. Laser frequencies were taken from Ref. 14; the notation for isotopic species is as follows: α = $^{12}C^{16}O$, β = $^{12}C^{18}O$, and τ = $^{13}C^{16}O$.

b. Microwave frequency in MHz; a minus sign indicates that the microwave frequency is subtracted from the laser frequency to obtain ν_{obs}.

c. Observed wavenumber in cm^{-1}.

d. Observed minus calculated wavenumber in multiples of 0.00001 cm^{-1}. Parameters are from the third column of Table III and the second column of Table IV.

e. Uncertainty in multiples of 0.00001 cm^{-1}.

f. Transitions marked by Z were eliminated from the fit.

compared to previous results for the ground state in Table III and for the $v_2 = 1$ state in Table IV.

In one fitting the 15 rotational parameters for the ground state, the 15 rotational parameters for the $v_2 = 1$ state, and the ν_2 vibrational energy were adjusted to fit the rotational frequencies and all of the well-determined vibration-rotation frequencies for $K_a < 9$ and for $J < 20$ for $K_a = 9$. These parameters are shown in the second column of Table III and the third column of Table IV. The observed minus calculated frequencies for this fitting are not shown but the standard deviation for an object of unit weight shown at the bottom of Table IV indicates that most of the residuals were smaller than the estimated uncertainties. For this and subsequent fittings, several infrared frequencies were omitted; these are marked with a Z in Table II. The reason for these omissions is discussed below.

The ν_2 vibration is of symmetry A_1 in C_{2v}. Therefore, the vibration-rotation transitions follow a-type rotational selection rules for which the frequencies are not very sensitive to the molecular constants that multiply functions that are approximately simple powers of K_a. For this reason, the infrared frequencies in the present study do not add much information about the ground state constants to that already available from the rotational frequencies. By contrast, the ground state combination differences obtained in the previous studies of the Coriolis-coupled ν_3, ν_4, ν_6

Table III.

Comparison of Ground State Rotational and Centrifugal Distortion Constants for D_2CO

Parameter[a]	This Work[b]	ν_3,ν_4,ν_6 Bands[c]	ν_1,ν_5 Bands[d]	Microwave[e]
A	4.7250502(29)	4.7250501(13)	4.7250505(18)	4.7250455(42)
B	1.0768638(6)	1.0768638(2)	1.0768639(3)	1.0768640(8)
C	0.8734485(6)	0.8734482(2)	0.8734482(3)	0.8734489(8)
$\Delta_J \times 10^4$	0.017645(62)	0.017636(15)	0.017629(30)	0.017712(167)
$\Delta_{JK} \times 10^4$	0.20691(65)	0.20676(13)	0.20682(26)	0.20781(167)
$\Delta_K \times 10^4$	1.48900(899)	1.49498(40)	1.49357(200)	1.46768(2502)
$\delta_J \times 10^4$	0.003824(7)	0.003823(2)	0.003824(4)	0.003813(17)
$\delta_K \times 10^4$	0.173637(1041)	0.174166(85)	0.174090(142)	0.173453(3336)
$\Phi_J \times 10^7$	0.000108(121)	0.000069(17)	0.000072(47)	0.0 (fixed)
$\Phi_{JK} \times 10^7$	0.00412(323)	0.00548(35)	0.00517(117)	-0.00097(200)
$\Phi_{KJ} \times 10^7$	-0.0099(401)	-0.0124(13)	-0.0168(64)	0.1001(834)
$\Phi_K \times 10^7$	-0.3578(10297)	0.1660(17)	0.1651(100)	-2.0681(9173)
$\phi_J \times 10^7$	0.000022(23)	0.000026(4)	0.000021(13)	0.0 (fixed)
$\phi_{JK} \times 10^7$	0.00348(307)	0.00282(39)	0.00350(167)	0.0 (fixed)
$\phi_K \times 10^7$	0.0412(1042)	0.0978(74)	0.0807(309)	0.0667(667)

a. Units are cm^{-1}.

b. Values in parentheses are 2.5 times standard error in multiples of the unit of the last digit in the parameter.

c. Obtained by fit of combination differences of the bands shown in Ref. 12.

d. Obtained by fit of combination differences of the bands shown in Ref. 13.

e. Ref. 11.

Table IV.

Vibration Rotation Parameters for the ν_2 State of D_2CO

Parameter[a]	This Work[b]	This Work[c]	Laser Stark[d]
ν_o	1701.61924(10)	1701.61924(10)	1701.62000(83)
A	4.7264861(163)	4.7264857(164)	4.7264898(1946)
B	1.0695897(12)	1.0695898(13)	1.0696867(1946)
C	0.8672745(12)	0.8672748(13)	0.8672200(2780)
$\Delta_J \times 10^4$	0.017549(24)	0.017562(66)	--
$\Delta_{JK} \times 10^4$	0.21804(52)	0.21816(83)	--
$\Delta_K \times 10^4$	1.4943(53)	1.4883(105)	--
$\delta_J \times 10^4$	0.003767(11)	0.003768(12)	--
$\delta_K \times 10^4$	0.18087(107)	0.18042(143)	--
$\Phi_J \times 10^7$	0.000051(19)	0.000087(112)	--
$\Phi_{JK} \times 10^7$	0.00692(88)	0.00569(301)	--
$\Phi_{KJ} \times 10^7$	-0.0220(71)	-0.0201(394)	--
$\Phi_K \times 10^7$	0.1551(506)	-0.3671(10358)	--
$\phi_J \times 10^7$	0.000016(8)	0.000012(22)	--
$\phi_{JK} \times 10^7$	0.00323(93)	0.00382(294)	--
$\phi_K \times 10^7$	0.1162(223)	0.0644(978)	--
Std. Dev.[e]	0.71	0.71	

a. Units are cm^{-1} except for the standard deviations.

b. Ground state parameters constrained to values from Ref. 12. Values in parentheses are 2.5 times standard error in multiples of the units of the last digit in the parameter.

c. All parameters varied.

d. Ref. 3.

e. Standard deviation for an observation of unit weight (from the fit).

and ν_1, ν_5 systems contain considerable information about the ground state constants and in each of these studies ground state constants were derived. All of these sets of constants are compared in Table III where it is seen that the values determined in Ref. 12 and 13 are essentially equivalent.

Because of the availability of highly precise sets of constants for the ground state, we report the results of a least squares fitting of the present infrared data in which the values of the ground state constants were constrained to the values reported in Ref. 12. The $v_2 = 1$ constants obtained from this fitting are given in the second column of Table IV and the observed minus calculated frequencies for the infrared transitions for this set of parameters are shown in Table II. The two fittings described here give roughly equivalent representations of the experimental data, as can be seen by comparison of the standard deviations for an observation of unit weight reported at the bottom of Table IV.

It is apparent from the residuals for the transitions marked with a Z in Table II that there is a resonance effect for $K_a = 9$ and 10 that gets stronger for high J. The nature of this effect is not known at this time, but it could be the result of a Fermi resonance with $v_4 = 2$, which should occur near 1900 cm^{-1}. The fact that the residuals for the $K_a = 9$ states in Table II are negative whereas those for

K_a = 10 are positive suggests that if a Fermi resonance is involved, the K_a = 9 and 10 rotational levels of the resonant state lie between the K_a = 9 and K = 10 levels of v_2 = 1.

6. Conclusion

The results of Tables II-IV demonstrate a successful application of the new technique of infrared microwave sideband laser spectroscopy in the CO laser region. They provide further evidence of typical experimental accuracy in frequency measurement in the CO laser region of better than ± 10 MHz, although it is necessary to insure that the laser is oscillating on only one laser transition in order to achieve this accuracy. As shown in the previous part of this dissertation, differences in frequencies of transitions measured with different microwave sidebands on the same laser line are reliable to about ± 3 MHz. In an attempt to improve the resolution and precision of relative frequency measurements, we are trying to measure saturation dips in D_2CO with the CO laser sideband system in the "cavity mode" described in the previous part. However, greater absolute accuracy in frequency measurement in this spectral region with the sideband system will have to await development of a routine method for generation of reproducible CO laser frequencies and precise measurement of the frequencies so

generated.

The parameters for the $v_2 = 1$ state given in Table IV should allow calculation of the frequencies of the ν_2 band of D_2CO to within ± 10 MHz for transitions with $J \leq 36$ and $K_a \leq 8$. This is a substantial improvement in accuracy compared to the parameters previously available [3].

NONLINEAR SPECTROSCOPIC APPLICATION

Measurements of the Frequencies of Asymmetry Doublets of H_2CO and D_2CO with IR-RF and IR-MW Double Resonance Methods

As was mentioned in Part I of this dissertation, one of the main advantages of the microwave modulated infrared sideband laser system is that it has sufficient intensity to be a tunable pumping source for saturation spectroscopy.

From the viewpoint of molecular structure, the difficulties encountered for linear spectroscopy in the IR region include: 1. limited resolution due to the Doppler effect; 2. low intensities of fine and hyperfine structure transitions in excited vibrational states as a result of low populations due to the Boltzmann distribution; and 3. the complexity of the spectra that makes it difficult to identify energy levels because of the overlap of various combinations of vibrational bands and the perturbations between them. These difficulties can be overcome by using various forms of saturation spectroscopic measurements. Lamb dip measurement and double resonance are two of the most popular saturation spectroscopic methods.

First of all, the Doppler effect is the familiar effect that causes the frequency of a train's whistle to increase as the train travels with constant velocity towards an

observer and to decrease as it leaves. In a similar way, the frequency of the radiation felt by a molecule differs from the absolute frequency of the radiation because of the relative velocity between the source and the molecule. If the transition frequency of the molecule is ν_o, then for the molecule with a velocity v in the same direction as the radiation, the radiation with frequency

$$\nu' = \frac{\nu_o}{1 - v/c}$$

will be absorbed. Because the relative velocity of the molecule is distributed according to the Maxwell distribution, the transition lineshape caused by this effect is called the Doppler lineshape. It is not a problem in the microwave and radiofrequency region, simply because the ν_o is so small that the Doppler effect linewidth is normally much smaller than the homogeneous linewidth of the transition and can be neglected. But in the infrared region the situation is different. For example, at ~1700 cm^{-1}, D_2CO has a Doppler full width of ~110 MHz, whereas the homogeneous widths at the pressures used for the work in the previous section were < 10MHz. As we have seen in Figures 2 and 3, two or more transitions often overlap one another because the IR frequency separation is smaller than the Doppler linewidth. In some cases, we can use a least squares method to fit the lineshape of the transitions as a superposition of two Gaussian profiles, as for example, to

separate the transitions $13_{5,9} \leftarrow 14_{5,10}$ and $13_{5,8} \leftarrow 14_{5,9}$ shown in Figure 3. However, in some cases, such as in Figure 2 for example, there is just no way to separate and measure the frequencies of the two transitions $12_{7,6} \leftarrow 11_{7,5}$ and $12_{7,5} \leftarrow 11_{7,4}$ by conventional linear spectroscopic methods.

Since the Doppler effect comes mainly from the Maxwell distribution of the velocity of the molecule, the way to eliminate it is to select just a certain velocity group of the molecules to absorb the radiation. The molecular beam technique and the Lamb dip measurement are two of the most popular methods for achieving this selectivity. Because the molecular beam technique gains its selectivity by a special design for generation of the sample beam and is not necessarily a saturation spectroscopic measurement, only the Lamb dip measurement will be discussed here. The Lamb dip method makes use of a mirror to reflect the incoming laser beam back through the sample cell again. Since molecules with velocity v relative to the incoming beam have velocity -v relative to the reflected beam, only the radiation with frequency ν_o will be absorbed by the same group of molecules during both passes, and this group of molecules has v = 0. If the laser radiation beam has enough power to partially saturate the transition during the first pass, then the absorption of the reflected radiation will be reduced. Since this occurs only for $\nu = \nu_o$, a dip in the absorption

spectrum occurs at the frequency ν_o. Also, because this dip requires v = 0, the linewidth of the dip is only the homogeneous width, which may be as low as 10 kHz. With this kind of resolution, it is possible to separate many severely overlapped transitions.

Because of the Boltzmann distribution, at room temperature the population in individual rotational levels in an excited vibrational state at 1700 cm^{-1} is around 2/10000 of that of the corresponding levels in the ground vibrational state. Therefore, it is very difficult to obtain the microwave spectrum directly to investigate the rotational structure in the vibrational excited state or to obtain hot band transitions to realize more about the structure of a higher vibrational state. Even substantial increases in temperature do not increase the population in the excited vibrational state enough for reasonable spectroscopic measurement, and also greatly complicate the spectrum.

The double resonance method, however, can overcome this small population distribution by utilizing an intense pumping laser radiation to saturate an infrared transition so as to cause a non-Boltzmann distribution in the two energy levels involved in the IR transition. This decreases the population of the energy level in the ground state and increases the population of the energy level in the vibrational excited state. At the same time radiation from

a probing source is applied to monitor the absorbance change in a transition that either has one common energy level (three level double resonance) or has at least one of its energy levels related through energy transfer (four level double resonance) to the two energy levels that belong to the pumping transition.

Usually, even for a small molecule the rovibration spectrum is very complicated and it is difficult to identify the energy states for an observed transition. A variety of techniques such as the Stark effect or Zeeman effect may be applied to identify the levels by means of the splittings induced. Unfortunately, these effects can make the spectrum even more complicated to analyze because of these splittings. By contrast, the three level double resonance method usually can be used to simplify the spectrum, since it has the selectivity that only certain transitions that satisfy known energy level patterns will be selected and observed. More detail about the three level double resonance method will be provided later.

As mentioned in Part I of this dissertation, the CO_2-MW sideband laser has been used successfully to obtain Doppler-free Lamb dip spectra [16-18] and IR-RF double resonance signals [19,20]. Shortly after the success of applying the CO-MW sideband laser to the study of the ν_2 band of D_2CO, an attempt was made to operate this new sideband laser in the resonant cavity mode to observe Lamb

dip spectra of H_2CO at ~1760 cm^{-1}. Unfortunately, although the laser sideband should have enough intensity (~1 mW) to saturate the transition, a difficulty exists in the use of the CO sideband laser system to obtain the Lamb dip signal. For the Lamb dip measurements, the transition width should be equal to the homogeneous width. This means that the width is expected to be of the order of 1 MHz or less. In order to stabilize the CO laser to the top of the gain curve, a sinusoidal signal must be applied to the piezoelectric translator in the laser cavity to frequency modulate the laser output. For reliable stabilization, the peak-to-peak frequency difference from this modulation signal is about 7 MHz. This means that even though our tunable sideband laser is powerful enough to generate a Lamb dip, the Lamb dip signal is averaged out as a result of the frequency modulation of the laser. Therefore, a more elaborate frequency stabilization scheme is required. After several unsuccessful attempts to observe a Lamb dip, we decided to try a double resonance experiment first, simply because the double resonance signal is not so sensitive to the stability of the IR laser frequency.

1. Introduction

Because of the near prolate asymmetric top structure of H_2CO and D_2CO, as shown in Figure 5, the $\pm k$ degeneracy is

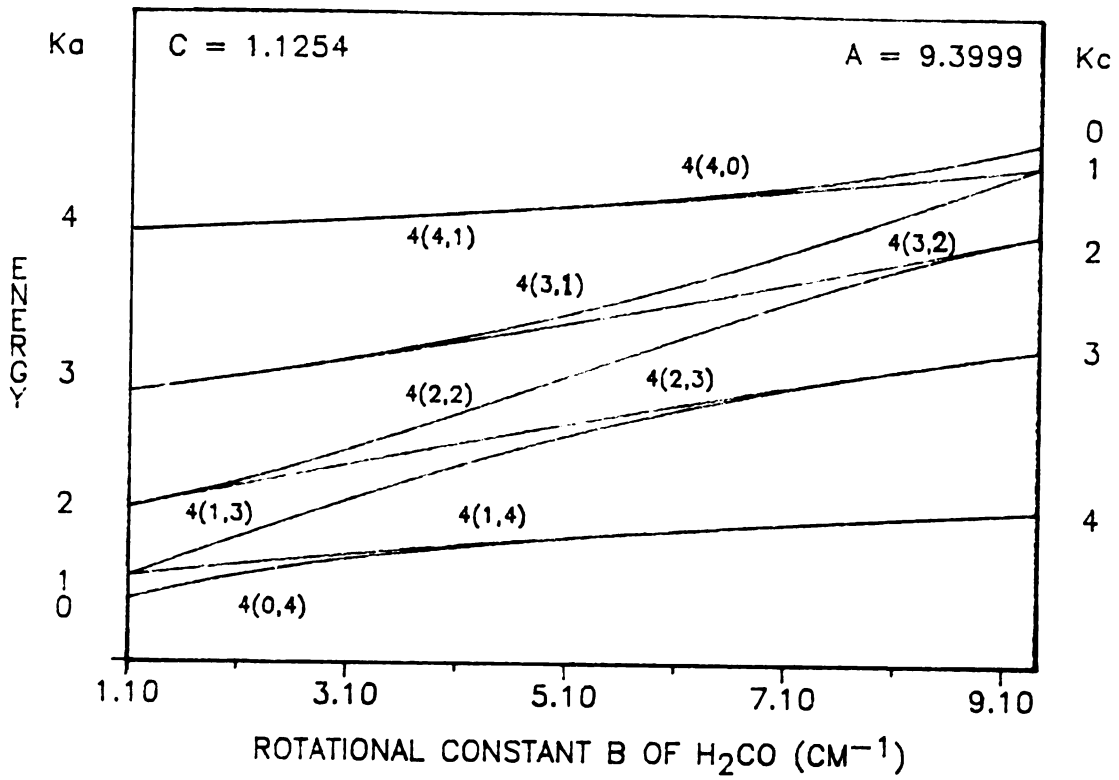

Figure 5. Qualitative behavior of the asymmetric-top energy levels. The rotational constant B varies from left to right, equaling C and giving a prolate symmetric top on the left, and equaling A to give an oblate symmetric top on the right. For the ν_2 vibrational state of H_2CO, A = 9.3999 cm^{-1}, C = 1.1254 cm^{-1}, and B = 1.2879 cm^{-1}. The rotational states with $\pm k$ degeneracy in J = 4 are split by the asymmetry.

split into two levels with the same K_a and different K_c by the asymmetry [21]. (Asymmetric rotor energy levels are labeled by the value of K = |k| that they would have if B = C (K_a) and if B = A (K_c).) The size of the splitting depends on the J and K_a quantum numbers and ranges in H_2CO and D_2CO from the radio frequency to the microwave region. Transitions between these "asymmetry doublets" are strong since they follow the selection rule for a-type rotational transitions, $\Delta K_a = 0$ and $\Delta K_c = \pm 1$. They therefore should be observable by radio frequency or microwave spectroscopy directly.

When the asymmetry splittings fall into the radio frequency region, the K-type doublet transitions are weak because of the very small population difference between the two energy levels and the very low sensitivity for radio frequency detection. Even in the ground state, the IR-RF double resonance method provides a much more sensitive method for detecting the K-type doublet transitions than conventional radio frequency spectroscopy [22]. However, because of the lack of an intense tunable infrared laser source, only a few K-type doublet transitions have been measured; the one report by P. Glorieux and G. W. Hills in 1978 [23] describes transitions pumped by the accidental coincidence between infrared transitions in H_2CO, HDCO and CO_2 laser lines. In that experiment the radio frequency cell was put inside the laser cavity to further enhance the

sensitivity for the observation of the collision-induced transitions as well.

When the transitions fall into the microwave region and involve levels in the ground vibrational state, they have been studied by microwave spectroscopy directly [11]. However, in an excited vibrational state, as a result of the Boltzmann distribution of populations, only a few K-type doublet transitions have been observed by ordinary microwave spectroscopy, even by heating the sample up to 200 ^{o}C [9]. A number of IR-MW double resonance measurements have already been carried out in formaldehyde. For example, a Zeeman-tuned He-Xe laser was used to study microwave transitions in the ground and ν_5 = 1 vibrational states of HDCO [24], and in the ground state of H_2CO [25] as well as to study the IR-MW double resonance effect [26,27]. In the CO laser region, the rotational structure in the ν_2 = 1 state of H_2CO was studied by using the laser Stark effect to tune the IR transition to meet the CO laser frequency [28].

The purpose of the measurements described in this dissertation is to show that the new CO laser infrared microwave sideband source has sufficient power, when operated in the resonant cacity mode [1,2], to perform infrared microwave (IR-MW) and infrared radio frequency (IR-RF) double resonance.

2. Theory

The experiments of infrared microwave double resonance are classified into two groups according to which of the radiation sources is detected. One method is based on the intensity variation of a microwave absorption line caused by infrared pumping; the other method is based on the intensity variation of an infrared absorption caused by microwave pumping. Since infrared detection usually has higher sensitivity than microwave detection, the second method usually is adopted. Especially, for infrared radio frequency double resonance measurements, only the second method is used because the sensitivity of the radio frequency detection is so low.

The theory of infrared microwave double resonance had been explored by the rate equation method in the early days [26,27] and later treated by quantum mechanics by Oka [29] and by Takami [30,31] by using the density matrix in a steady state approximation. The Hamiltonian for the three-level systems shown in Figure 6 under the influence of infrared and microwave or radio frequency radiations is given by

$$H = H_o - E\,\mu \cos \omega t - E_m\,\mu \cos \omega_m t + H_r \,. \qquad (6)$$

Here, H_o is the Hamiltonian of the unperturbed molecule, H_r

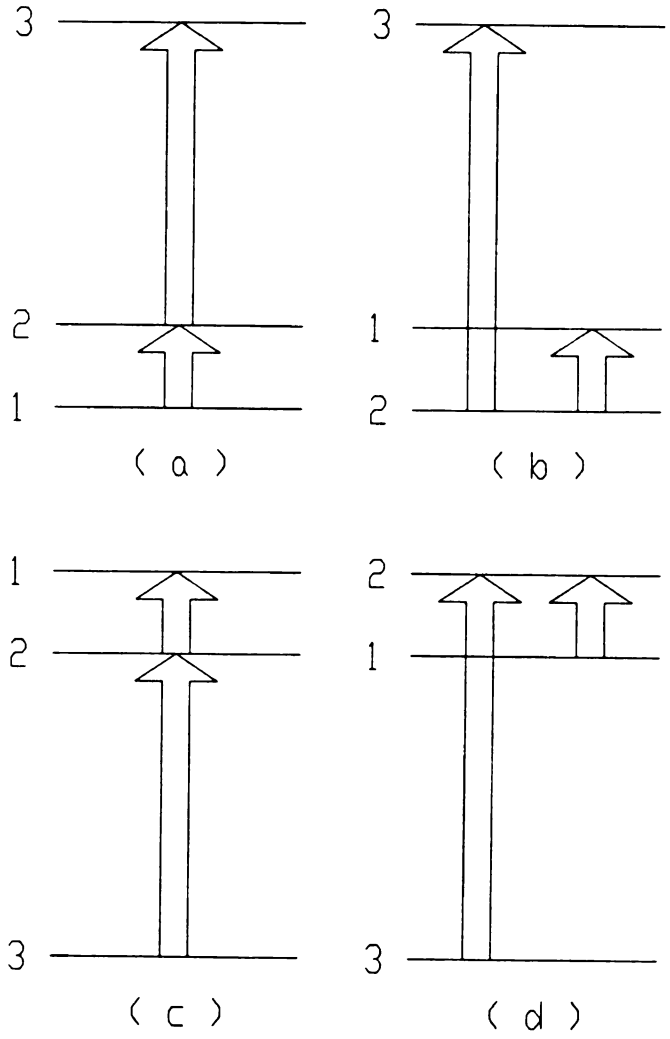

Figure 6. Four types of three-level system for infrared microwave or infrared radio frequency double resonance. The energy levels are numbered so that the infrared transition is between levels 2 and 3, and the microwave or radio frequency transition is between levels 1 and 2.

is the random perturbations which cause relaxation of the system to thermal equilibrium, μ is the dipole moment, E, E_m, ω and ω_m are the amplitudes and angular frequencies of the infrared and microwave radiations, respectively. The power absorbed from the infrared radiation by the molecules in a double resonance experiment can be shown to be

$$P = - \int_{-\infty}^{+\infty} \frac{i}{4\pi} h \omega N \alpha \, dv_z \, , \qquad (7)$$

where $\alpha = \varkappa \rho_{32} \exp(i\omega t) - c.c.$; $\varkappa = 2\pi \mu_{23} E/h$ where μ_{ij} is the transition matrix element from the i-th to the j-th level; and ρ_{32} is the off-diagonal element of the density matrix corresponding to the infrared transition. Also, N is the total number of molecules in the interaction region and v_z is the velocity component of the molecule in the direction of the incident infrared radiation. Within the rotating wave approximation an explicit form for α can be calculated by solving the equation of motion of the density matrix in the steady state and α can be shown to be a function of ρ_{ii}^{o}, $\varkappa$, $\varkappa_m$, $\Delta\omega$, $\Delta\omega_m$, and γ. Here ρ_{ii} is the diagonal element of the density matrix at thermal equilibrium, $\varkappa_m = 2\pi \mu_{12} E_m/h$, $\Delta\omega = \omega - \omega_{23} - kv_z$, $\Delta\omega_m = \omega_m - \omega_{12}$, $k = \omega/c$, ω_{ij} is the angular frequency of the transition from the i-th to the j-th level without any Doppler shift, and c is the speed of light. For these calculations it is common to assume that all of the

relaxation processes are expressed by a single relaxation constant γ in order to simplify the equation.

The double resonance signal ΔP is defined as the change in P caused by microwave pumping,

$$\Delta P = P_{(x_m)} - P_{(x_m=0)} \cdot \qquad (8)$$

At thermal equilibrium, the diagonal density matrix elements ρ^o_{ii} are given by the Maxwell velocity distribution

$$N \rho_{ii}^{o} = N_i^o \exp(- v_z^2/u^2) / (\sqrt{\pi}\, u), \qquad (9)$$

where N_i^o is the number of molecules in the i-th level at thermal equilibrium and u is the most probable speed of the molecules. In the Doppler limit approximation where the homogeneous width is much smaller than the Doppler width, only the small δv_z group of molecules with $v_z = (\omega - \omega_{23})/k$ will absorb infrared radiation with frequency ω. For simplification of the integration in the Eq. (7) it is common to assume that δv_z is very small so that only molecules with $v_z = (\omega - \omega_{23})/k$ are pumped by the infrared radiation. For example, if $\omega = \omega_{23}$ only molecules with $v_z = 0$ will absorb the infrared radiation.

In Figure 6 four types of three-level systems are shown. The following calculation is carried out for the (a) type three-level system. The double resonance signals for the other three types can be obtained by using suitable

values for N_i^o and by changing the sign of Eq. (7) for types (c) and (d).

For the case when x is small, (*i.e.*, weak infrared saturation), the double resonance lineshape can be derived by expanding α as a function of x [31]. Then,

$$\Delta P = \frac{h\omega x^2 x_m^{\,2}}{8\sqrt{\pi}\, ku} \left[\Delta P^{(0)} + \Delta P^{(1)} x^2 + \Delta P^{(2)} x^4 + \cdots\cdots \right], \qquad (10)$$

where $\Delta P^{(0)}$ and $\Delta P^{(1)} x^2$ can be shown to be

$$\Delta P^{(0)} = \frac{(N_1^o - N_2^o)}{(\Delta\omega_m)^2 + \gamma^2 + x_m^2}\ , \qquad (11)$$

and

$$\Delta P^{(1)} x^2 \approx \frac{1}{2} (N_2^o - N_3^o) \frac{x^2}{\gamma^2} L_m\ , \qquad (12)$$

where

$$L_m = \frac{1}{(\Delta\omega_m)^2 + \gamma^2 + x_m^{\,2}}\ . \qquad (13)$$

Several points about these formulas should be emphasized:

a. Although the IR signal is monitored, the spectrum is Doppler free. It can be seen from Eqs. (11)-(13) that either $\Delta P^{(0)}$ or $\Delta P^{(0)} + \Delta P^{(1)} x^2$ give a lineshape that is a Lorentzian profile and that there is no v_z dependence; therefore, the spectrum is Doppler free.

b. When the microwave or radio frequency transition is in the ground state, $| N_1^o - N_2^o |$ is smaller than $| N_2^o - N_3^o |$ since the latter belongs to an IR transition. Moreover, when the microwave or radio frequency transition is in the vibrational excited state, the $| N_1^o - N_2^o |$ is even smaller. This suggests that for the (c) and (d) types of three-level double resonance measurements shown in Figure 6, the $\Delta P^{(1)} x^2$ term in Eq. (10) plays a more important role.

c. Since the second term of Eq. (10) is proportional to x^2/γ^2, the fact that γ is proportional to the sample pressure means that the double resonance signal has a pressure dependence.

d. For (b) and (d) types of three-level double resonance measurements as shown in Figure 6, the first and the second terms in Eq. (10) will have different signs. In some cases, by varying the sample pressure a change in sign of ΔP can be observed [26,31].

3. Experimental

Figure 7 shows the experimental setup for the IR-RF double resonance experiment. The generation of the microwave modulated laser sidebands in the resonant cavity

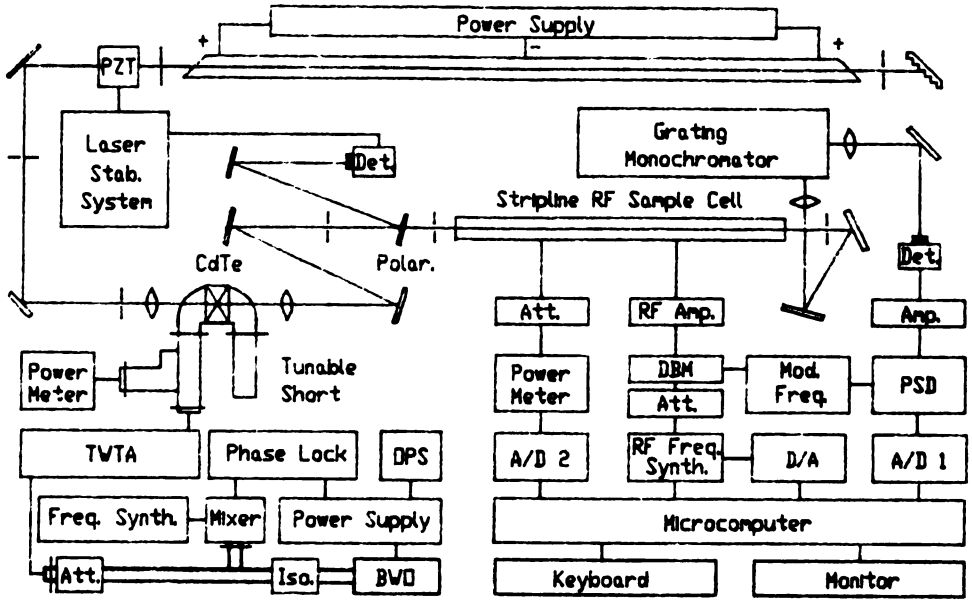

Figure 7. Instrument block diagram for the infrared radio frequency double resonance experiment.

mode has been described in detail in Part I of this dissertation. In the resonant cavity mode the modulator crystal is made part of a tunable microwave cavity in order to increase the amplitude of the microwave electric field at the crystal and therefore increase the sideband power. For our crystal, the loaded Q of the cavity is ~500 and the calculated output power for 20 W microwave power is ~2 mW sideband power per watt of incident CO laser power. Typical single line, single mode output of our CO laser is 200-500 mW, so a laser sideband with 0.4 - 1 mW intensity was used for double resonance experiments.

To carry out an infrared radio frequency double resonance experiment, the frequency of an appropriate infrared transition in the ν_2 band of H_2CO or D_2CO was measured in a preliminary linear spectroscopy experiment. Then, in the resonant cavity mode the microwave frequency ν_m was set to let either $\nu_\ell + \nu_m$ or $\nu_\ell - \nu_m$ equal the measured frequency of the IR transition. The tunable short after the CdTe crystal was adjusted manually to optimize the microwave cavity for the frequency ν_m. In order to further increase the sideband power density and therefore increase x, the recollimating lens after the modulator crystal was chosen to have one half the focal length of the focussing lens in front of the crystal.

The radio frequency radiation for the RF source is generated by a radio frequency synthesizer (PTS 500)

operating in the range 1 - 500 MHz with 0 - +13 dBm output power. The PTS radio frequency amplitude and frequency is controlled by a personal computer (IBM/AT). The output from the PTS synthesizer is connected to a variable attenuator (0 - 101 dB) and then to a double-balance mixer (DBM). In the DBM the radio frequency radiation is 100% amplitude modulated by a 22.5 kHz square wave which is provided by a function generator and a home built current driver. The amplitude-modulated radio-frequency radiation is then directed to a radio frequency power amplifier that has 50 dBm amplification. The amplified and modulated radio frequency output is then sent to a 50 ohm impedance matched RF sample cell [Figure 8] which is a 1-meter length of X-band waveguide fitted with a centered septum in a stripline design [32]. The open ends of the cell are covered with BaF_2 windows for infrared access. The radio frequency power is measured at the output of the sample cell by a power meter after 30 dB attenuation. Normally, the radio frequency power used in the IR-RF double resonance measurement is ~10 mW.

After the laser sidebands are directed through the RF stripline cell, a monochromator is used to separate the positive and negative sidebands in order to increase the signal-to-noise ratio by avoiding saturation of the detector with the contributions from the unwanted sideband and residual carrier. A liquid nitrogen cooled HgCdTe

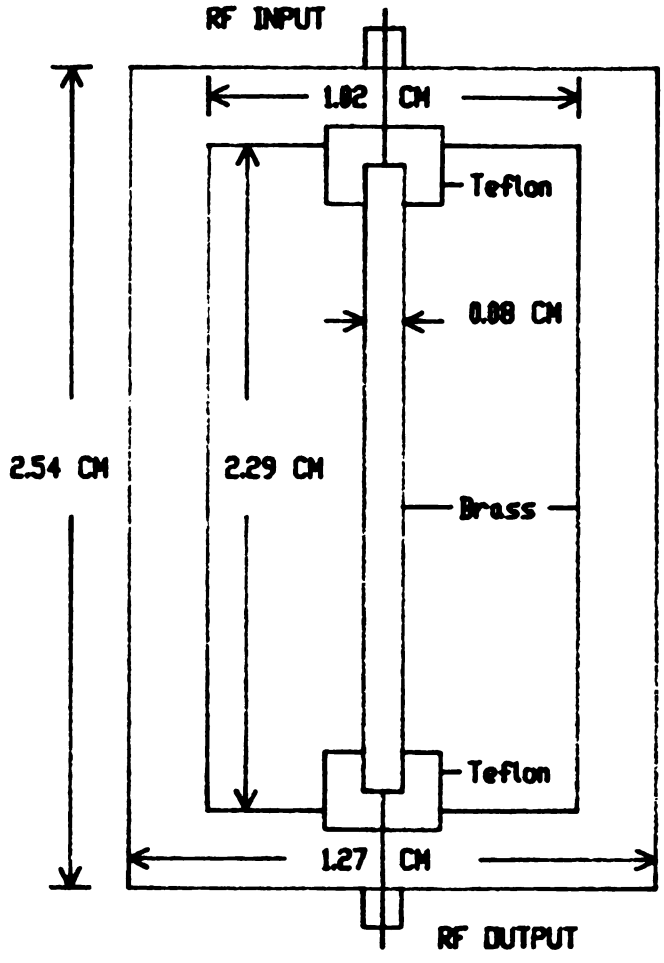

Figure 8. A cross section of the stripline radio frequency sample cell.

photoconductive detector is used to detect the intensity of infrared radiation. The output of the infrared detector is processed at the modulation frequency by a lock-in amplifier whose output is recorded by the personal computer that is programmed to sweep the radio frequency. In this way the single resonance absorption at either frequency is suppressed and only the double resonance effect is recorded.

For the IR-MW double resonance measurement, a similar experimental setup is used except for the microwave generation scheme [Figure 9]. Since our only P-band (12.4 - 18.0 GHz) BWO was used for the generation of the infrared laser sideband, it was necessary to use our X-band (8.2 - 12.4 GHz) BWO for the microwave source. For either source the microwave frequency is phase locked by means of a synchronizer to 20 MHz above a harmonic of the output of a radio frequency synthesizer. A harmonic mixer is used to create the beat frequencies between the microwave frequency and the harmonics of the reference frequency which have been mentioned in Part I of this dissertation. The microwave radiation for the double resonacne is then 100% amplitude modulated by a PIN diode switch. The 100% amplitude modulated microwaves are sent to a 1-meter long X-band waveguide with a 45^{o} E-plane bend at each end. The bends each have a 5 mm hole drilled in them for infrared access; the optical ports have NaCl windows whereas the microwave ports have mica windows. After leaving the sample cell, the

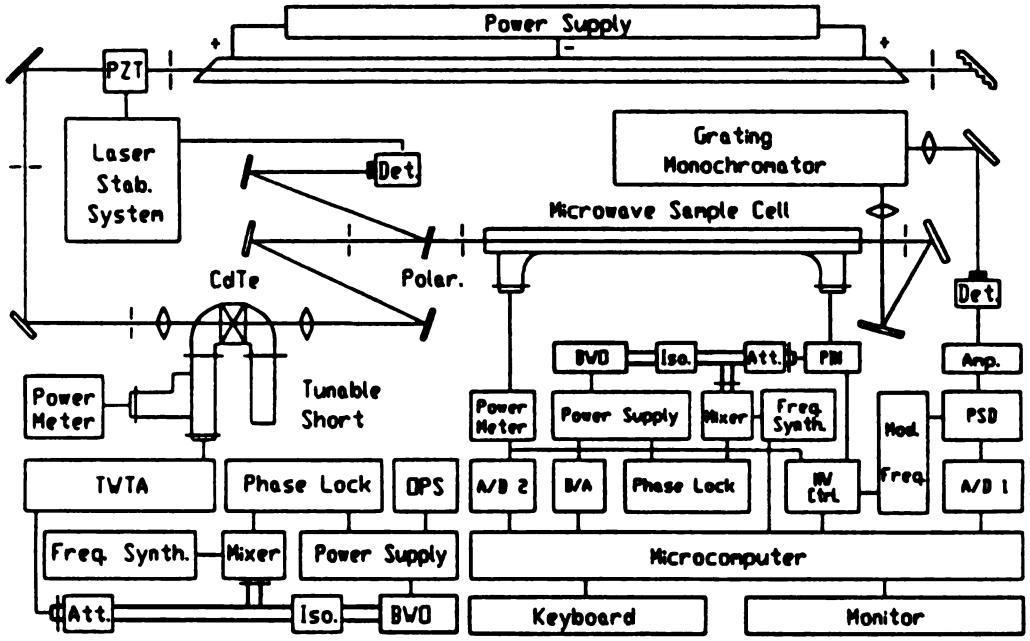

Figure 9. Instrument block diagram for the infrared microwave double resonance experiment.

microwave power is measured by a power meter; the microwave power normally used in our IR-MW double resonance experiments is ~15 mW.

Although both sample cells have adequate transmission across the desired frequency bands (1-500 MHz for the RF cell and 8-26 GHz for the microwave cell), neither of these cells has especially smooth transmission as a function of frequency. For the purposes of the spectra reported here, nothing was done to level the RF or microwave power as a function of frequency. However, we have developed a system for simultaneous amplitude modulation and control for microwave sources [33] and our computer program is fitted with provision for using the output of a power meter to control the output amplitude of the PTS radio frequency synthesizer.

The sample pressure is measured by a Hastings-type thermocouple gauge or by a capacitance manometer. Since the IR-RF and IR-MW double resonance signal is dependent on the sample pressure in the sample cell, the pressure is usually decreased from ~30 mTorr step by step in order to obtain the largest double resonance signal. The final sample pressure was normally ~7 mTorr. After the double resonance signal is obtained, a Lorentzian profile is used to fit the lineshape of the transition numerically by the least squares method to obtain the center frequency of the transition.

4. Results and discussion

Figure 10 shows an energy level diagram for two three-level double resonance measurements with the same infrared pumped transition; radio frequency transitions for both the ground vibrational state [Figure 11] and $v_2 = 1$ excited state [Figure 12] were observed. They belong to the (a) and (d) type three-level double resonance schemes shown in Figure 6, respectively. Figure 13 shows the corresponding energy level diagram for examples of (b) and (c) type three-level double resonance schemes; the respective double resonance signals are shown in Figures 14 and 15. First of all, according to Eqs. (10) and (11), if the $\Delta P^{(0)}$ term dominates, then the ΔP in the (a) type will have a positive value and in the (d) type will have a negative value. Since we measured both transitions without changing the phase of the lock-in amplifier, these (a) and (d) type double resonance signals all show an increase in absorption. The same situation occurs for the (b) and (c) pair. The results suggest that for these IR-RF double resonance experiments the $\Delta P^{(1)}$ x^2 term plays an important role, probably because $| N_1^o - N_2^o |$ is $\sim 10^5$ times smaller than $| N_2^o - N_3^o |$.

Further evidence for this argument is shown in Figures 17 and 18. The difference between these two figures is the applied radio frequency power only. In Figure 18, a larger

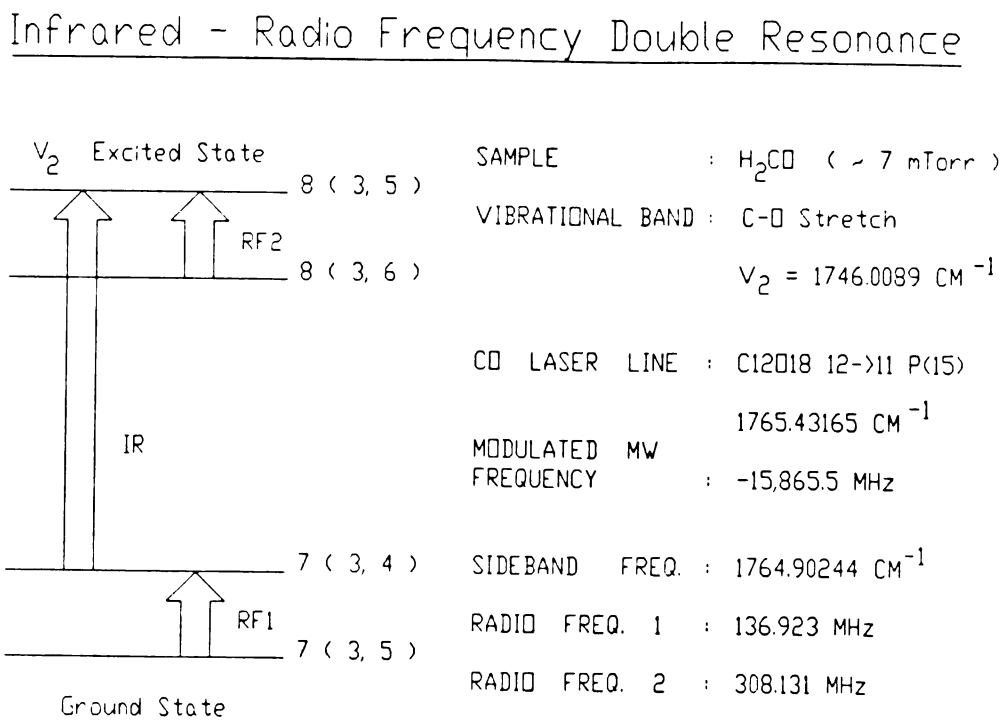

Figure 10. Energy level diagram for a pair of three-level IR-RF double resonance measurements. The ν_2 band transition, $8_{3,5} \leftarrow 7_{3,4}$, of H_2CO was partially saturated by the tunable CO-MW sideband laser operating in the resonant cavity mode with ν = 1764.90244 cm^{-1}. The RF transitions in the ground and v_2 = 1 vibrational states were observed and belong to (a) and (d) type three-level double resonance systems, respectively, as defined in Figure 6. The measured frequencies for RF1 and RF2 are also given.

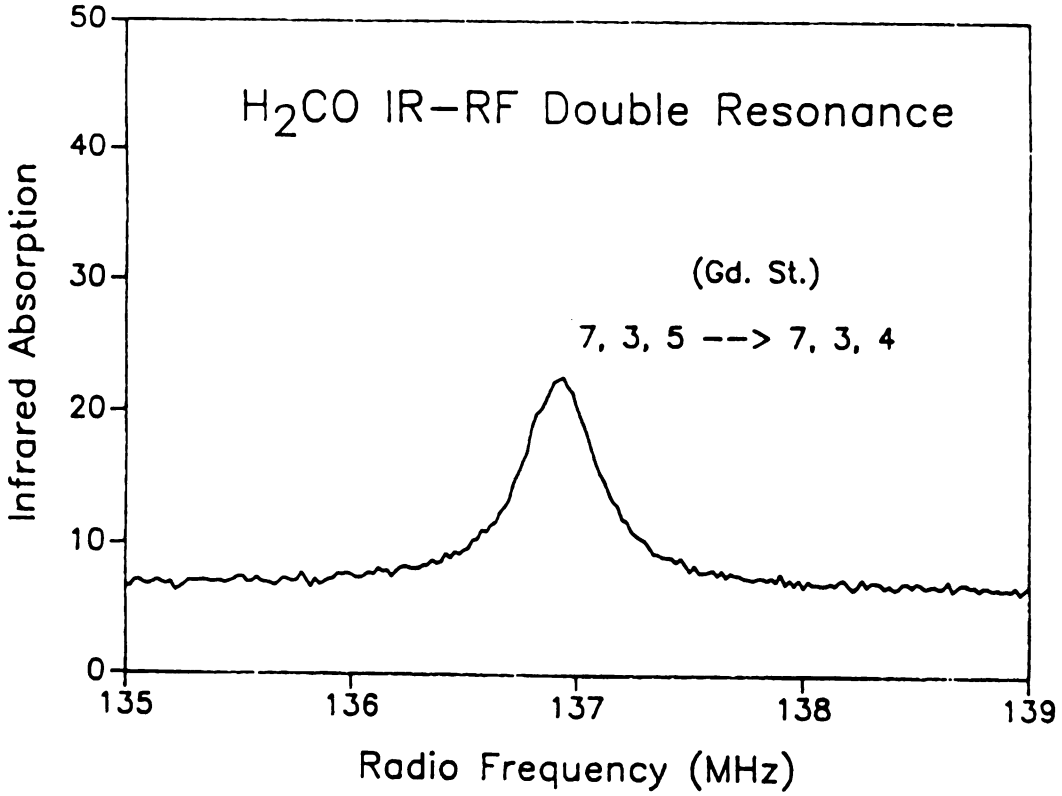

Figure 11. Plot of a ground state K-type doublet $7_{3,4} \leftarrow 7_{3,5}$ transition of H_2CO observed by the three level IR-RF double resonance method. The CO sideband laser was used to obtain partial saturation of the ν_2 band transition, $8_{3,5} \leftarrow 7_{3,4}$, at a pressure of ~7 mTorr; an energy level diagram is in Figure 10. In this plot the applied radio frequency is on the horizontal axis and the IR absorption is on the vertical axis.

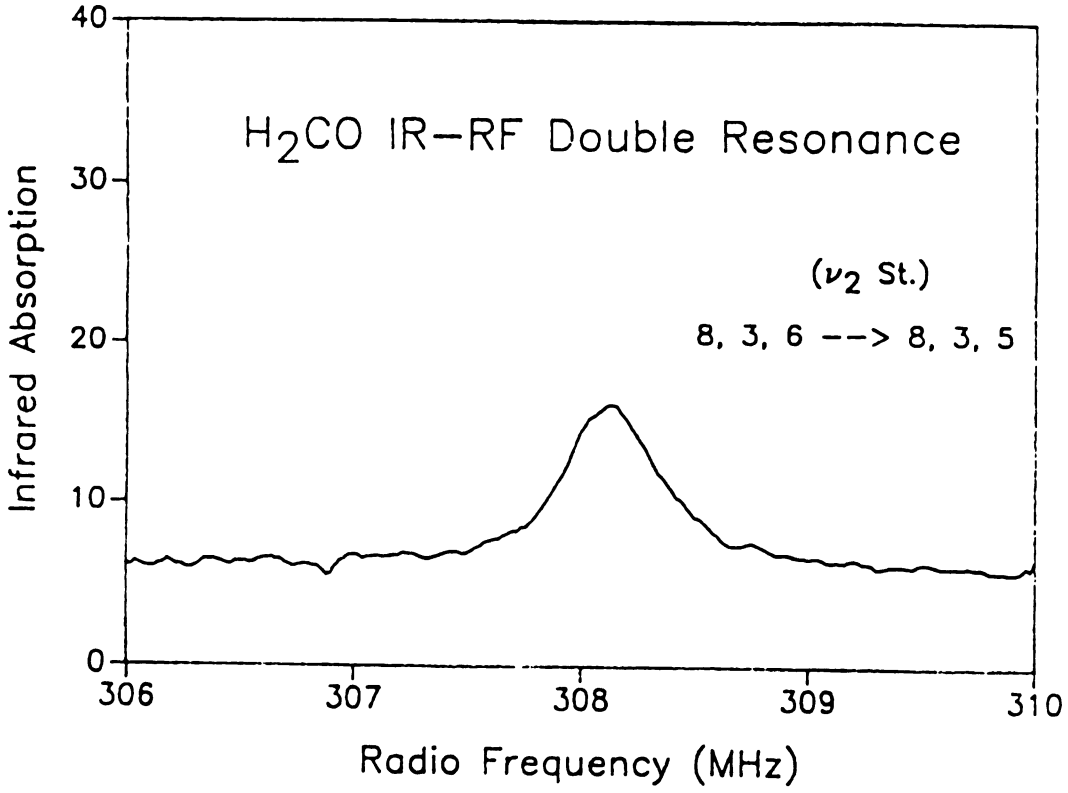

Figure 12. Plot of a ν_2 excited state K-type doublet $8_{3,5} \leftarrow 8_{3,6}$ transition of H_2CO observed by the three-level IR-RF double resonance method. The CO sideband laser was used to obtain partial saturation of the ν_2 band transition, $8_{3,5} \leftarrow 7_{3,4}$ at a pressure of ~7 mTorr; an energy level diagram is in Figure 10. In this plot the applied radio frquency is on the horizontal axis and the IR absorption is on the vertical axis.

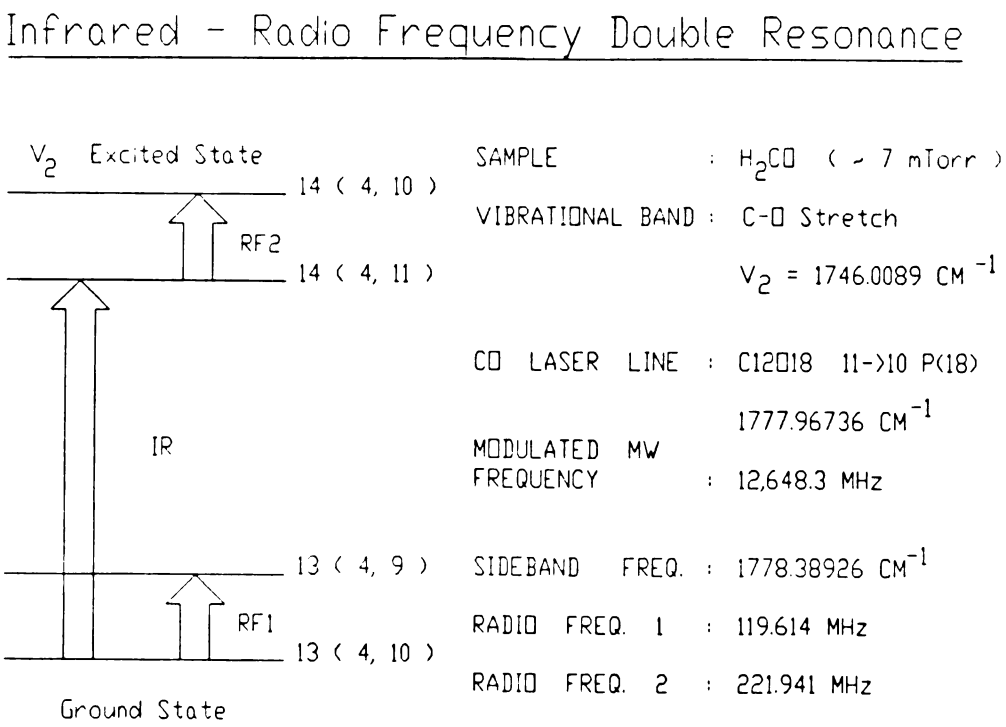

Figure 13. Energy level diagram for a pair of three-level IR-RF double resonance measurements. The ν_2 band transition, $^{14}_{4,11} \leftarrow {}^{13}_{4,10}$, of H_2CO was partially saturated by the tunable CO-MW sideband laser operating in the resonant cavity mode with ν = 1778.38926 cm^{-1}. The RF transitions in the ground and v_2 = 1 vibrational states were observed and belong to (b) and (c) type three-level double resonance systems, respectively, as defined in Figure 6. The measured frequencies for RF1 and RF2 are also given.

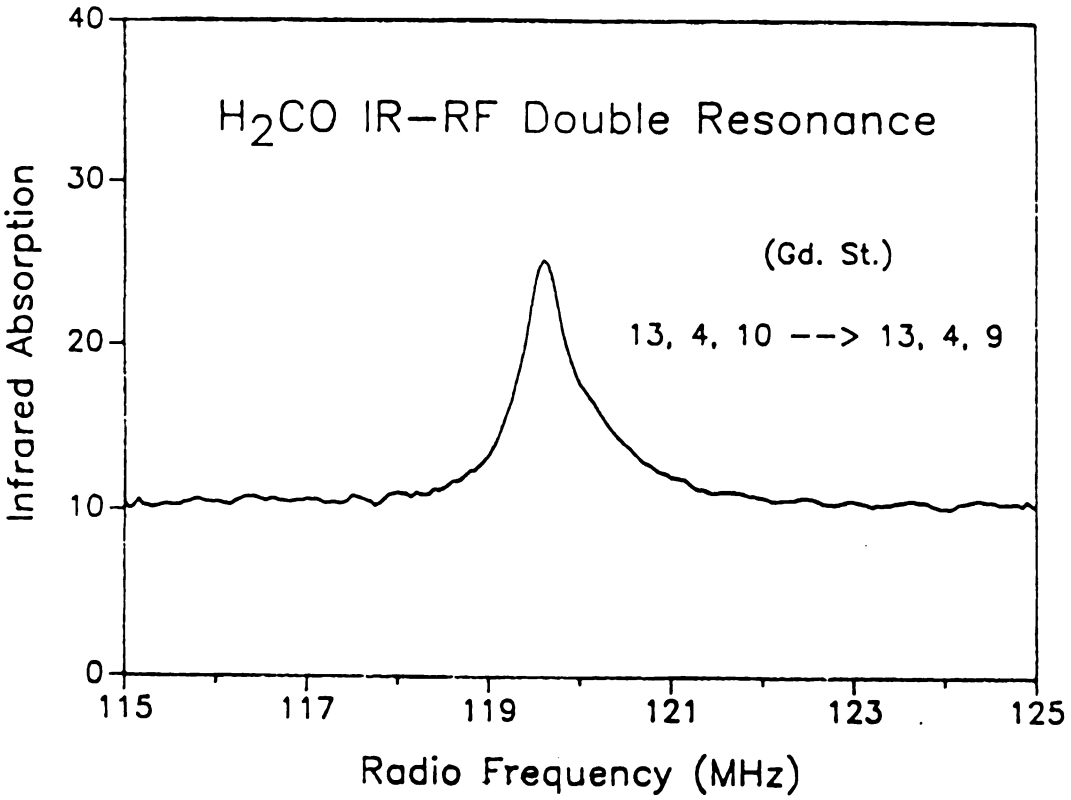

Figure 14. Plot of a ground state K-type doublet $13_{4,9} \leftarrow 13_{4,10}$ transition of H_2CO observed by the three level IR-RF double resonance method. The CO sideband laser was used to obtain partial saturation of the ν_2 band transition, $14_{4,11} \leftarrow 13_{4,10}$ at a pressure of ~7 mTorr; an energy level diagram is shown in Figure 13. In this plot the applied radio frequency is on the horizontal axis and the IR absorption is on the vertical axis.

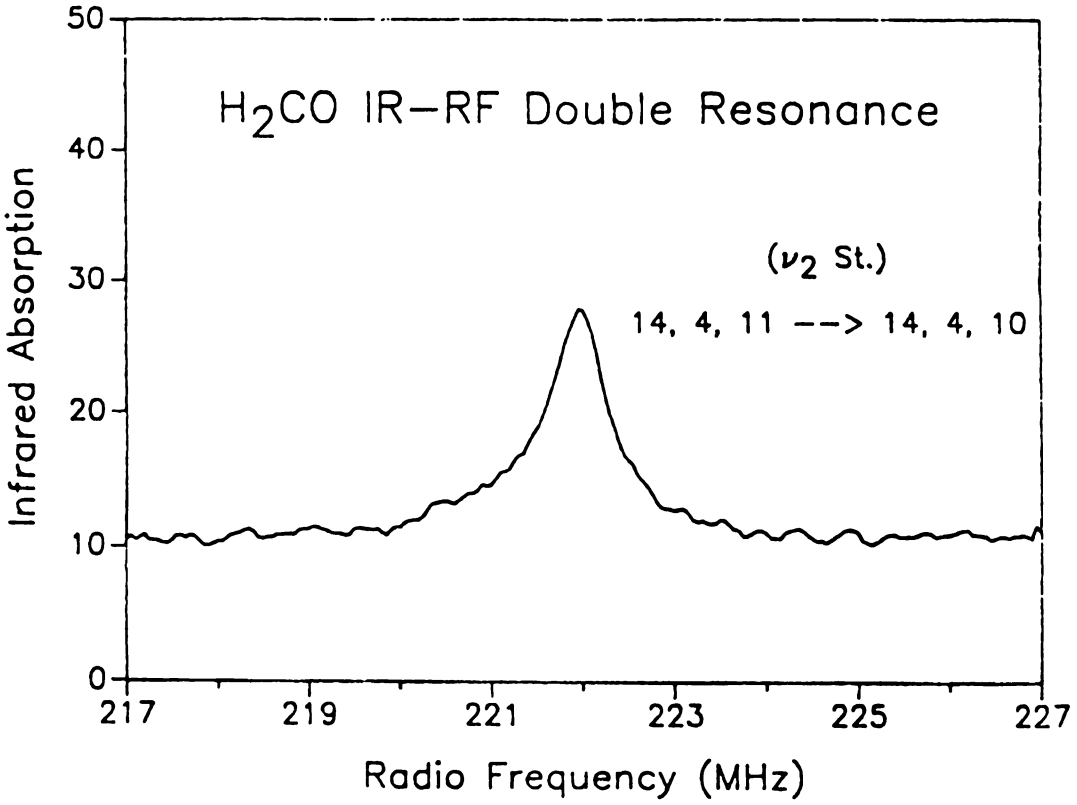

Figure 15. Plot of a ν_2 excited state K-type doublet $^{14}_{4,10}$ ← $^{14}_{4,11}$ transition of H_2CO observed by the three level IR-RF double resonance method. The CO sideband laser was used to obtain partial saturation of the ν_2 band transition, $^{14}_{4,11}$ ← $^{13}_{4,10}$ at a pressure of ~7 mTorr; an energy level diagram is shown in Figure 13. In this plot the applied radio frequency is on the horizontal axis and the IR absorption is on the vertical axis.

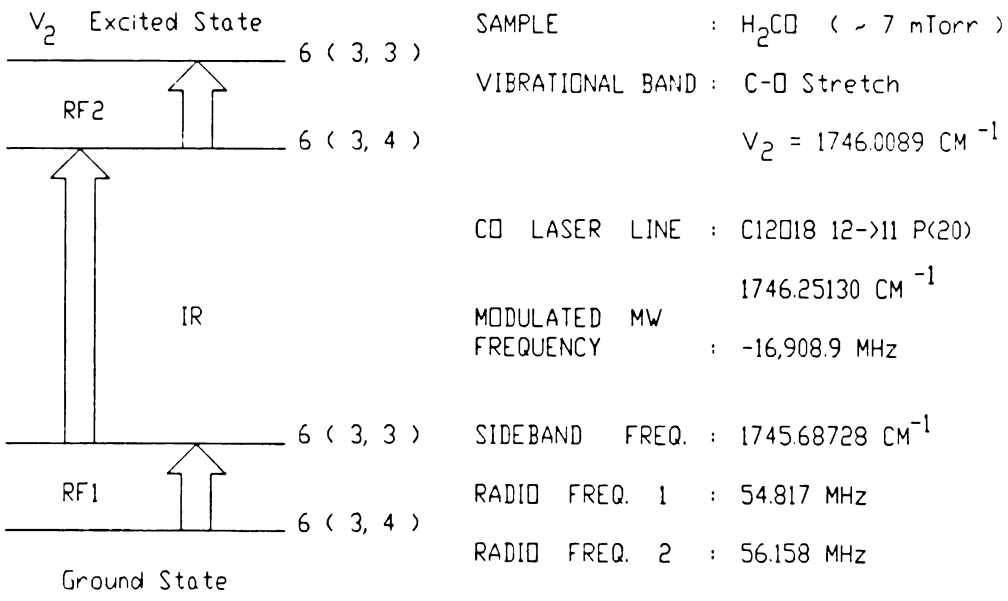

Figure 16. Energy level diagram for the three level IR-RF double resonance spectra shown in Figures 17 and 18. The ν_2 band transition, $6_{3,4} \leftarrow 6_{3,3}$, of H_2CO was partially saturated by the tunable CO-MW sideband laser operating in the resonant cavity mode with ν = 1745.68728 cm^{-1}. Radio frequency transitions in the ground and v_2 = 1 vibrational states were observed and they belong to (a)- and (c)-type three level double resonance systems as defined in Figure 6, respectively. The measured frequencies for RF1 and RF2 are also given.

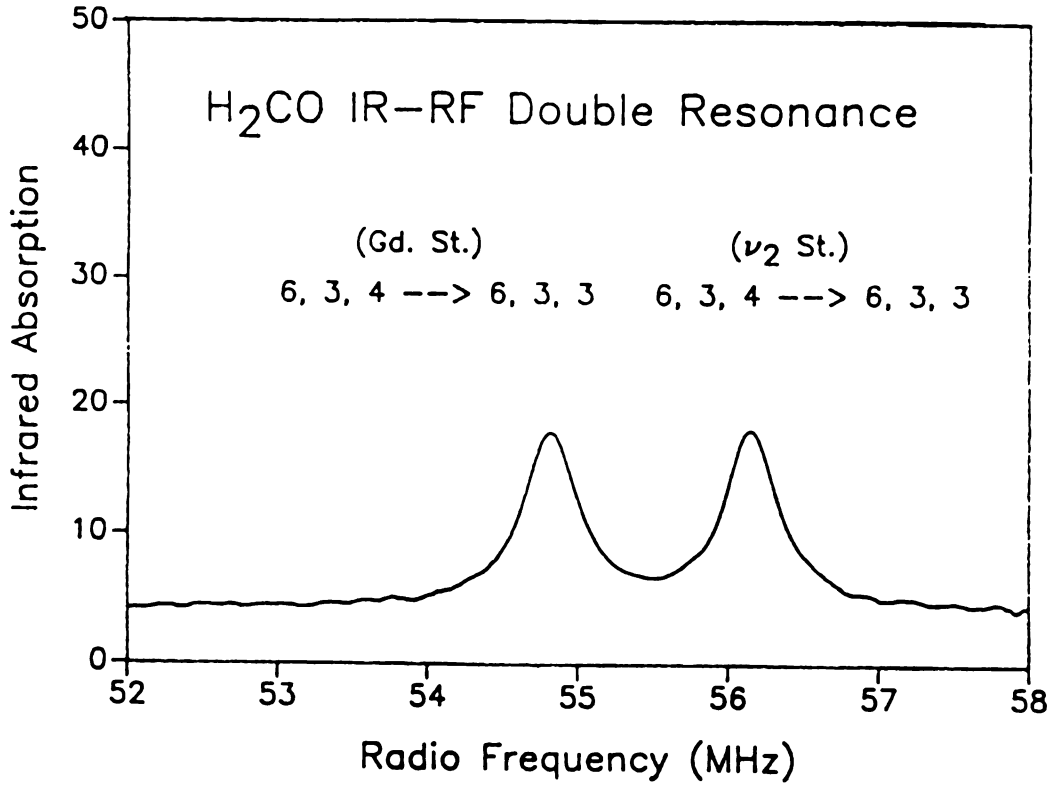

Figure 17. Plot of a ground vibrational state K-type doublet $6_{3,3} \leftarrow 6_{3,4}$ transition and a ν_2 excited vibrational state K-type doublet transition $6_{3,3} \leftarrow 6_{3,4}$ of H_2CO observed by the three level IR-RF double resonance method. The CO sideband laser was used to obtain partial saturation of the ν_2 band transition, $6_{3,4} \leftarrow 6_{3,3}$ at a pressure of ~7 mTorr; an energy level diagram is shown in Figure 16. In this plot the applied radio frequency is on the horizontal axis and the IR absorption is on the vertical axis. The applied radio frequency power is ~10 mW.

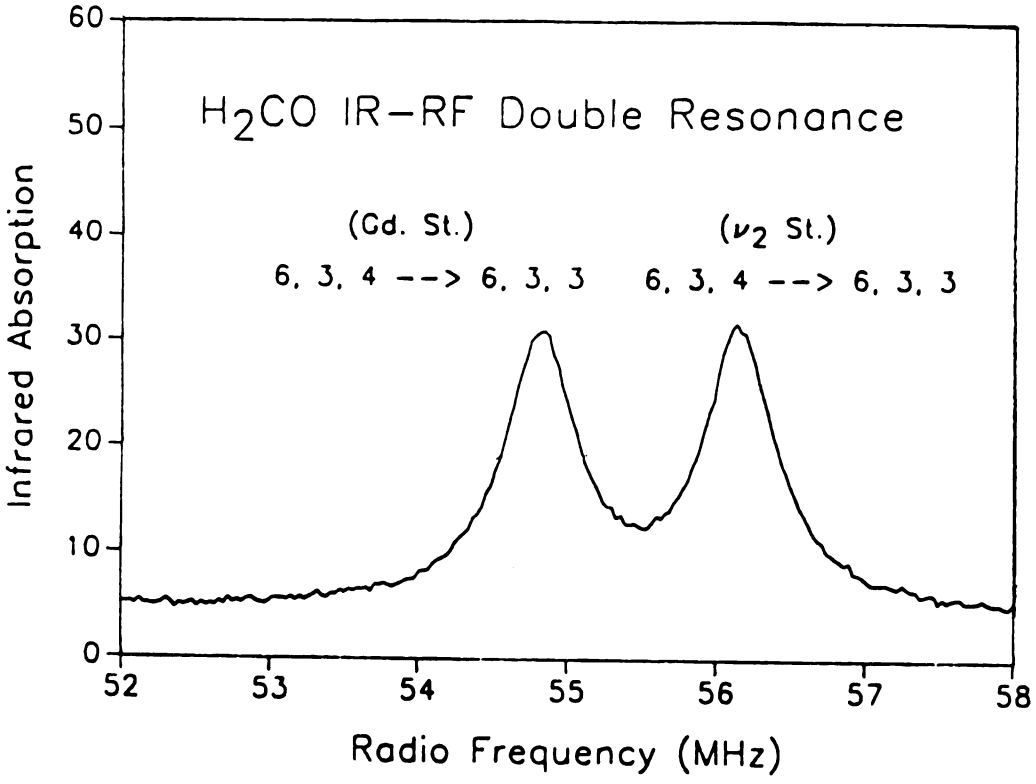

Figure 18. Plot of a ground vibrational state K-type doublet $6_{3,3} \leftarrow 6_{3,4}$ transition and a ν_2 excited vibrational state K-type double $6_{3,3} \leftarrow 6_{3,4}$ transition of H_2CO observed by the three level IR-RF double resonance method. The CO sideband laser was used to obtain partial saturation of the ν_2 band transition, $6_{3,4} \leftarrow 6_{3,3}$ at a pressure of ~7 mTorr; an energy level diagram is shown in Figure 16. In this plot the applied radio frequency is on the horizontal axis and the IR absorption is on the vertical axis. The applied radio frequency power is ~30 mW.

RF power is applied to obtain the double resonance signal. This pair of double resonance signals follows the (a) and (c) type three level double resonance schemes, respectively [Figure 16], and the ΔP of both are always positive. Upon increasing the RF power the height and width of these double resonance signals increase accordingly. This result is predicted by the theoretical calculation shown in the previous section. In the $\Delta P^{(1)}$ x^2 term the width and the height of the signal increases with x_m.

For the IR-MW double resonance experiment, because of the limitations in frequency range of the microwave source, only a ground vibrational state K-type doublet of H_2CO [Figure 20] with an (a)-type scheme [Figure 19] and a K-type doublet of D_2CO in the ν_2 vibrationally excited state [Figure 22] with a (c)-type scheme [Figure 21] were observed. Since both (a)- and (c)-type schemes have positive ΔP, these results are not sufficient to determine whether $\Delta P^{(0)}$ or $\Delta P^{(1)}$ dominates the double resonance signal. In the IR-MW double resonance experiment done by Takami et al. [31] with a Zeeman-tuned He-Xe laser as the laser source, a (b) type double resonance signal was observed. In that experiment a change in sign of ΔP was observed by decreasing the sample pressure; this suggests that the $\Delta P^{(0)}$ term can be important for an IR-MW double resonance experiment. This is consistant with Eq. (12) since in the (b) type IR-MW double resonance measurement the

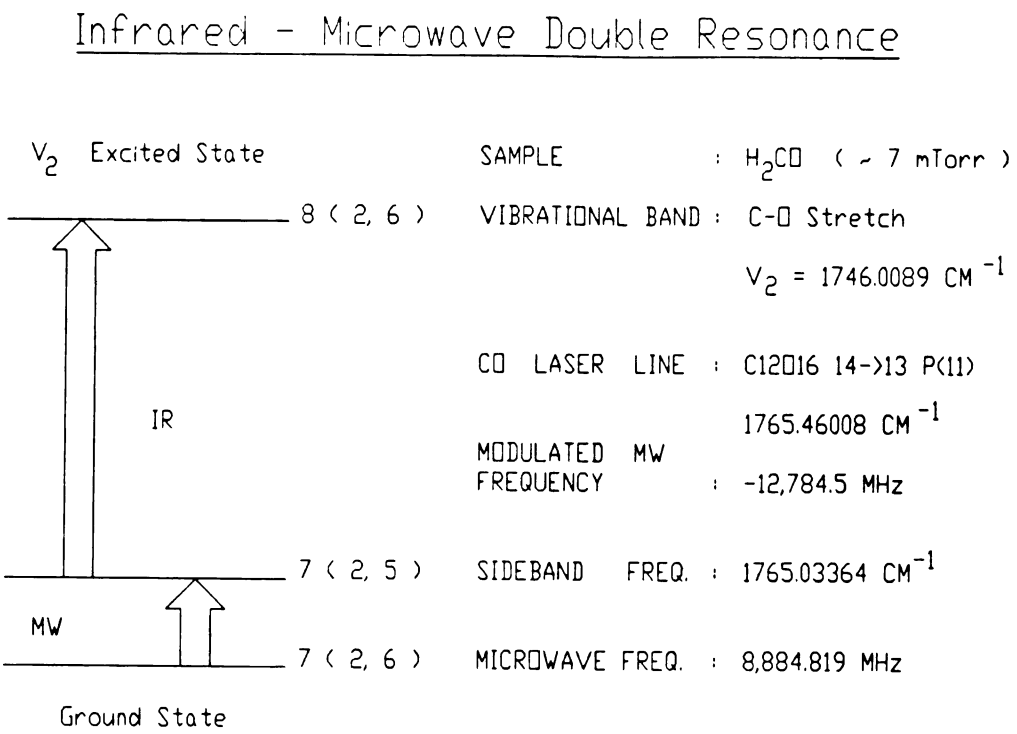

Figure 19. Energy level diagram for the three level IR-MW double resonance measurements shown in Figure 20. The ν_2 band transition, $8_{2,6} \leftarrow 7_{2,5}$, of H_2CO was partially saturated by the tunable CO-MW sideband laser operating in the resonant cavity mode with ν = 1765.03364 cm^{-1}. The microwave transition in the ground state is observed and is an (a)-type three level double resonance system as defined in Figure 6. The measured frequency for the microwave transition is given.

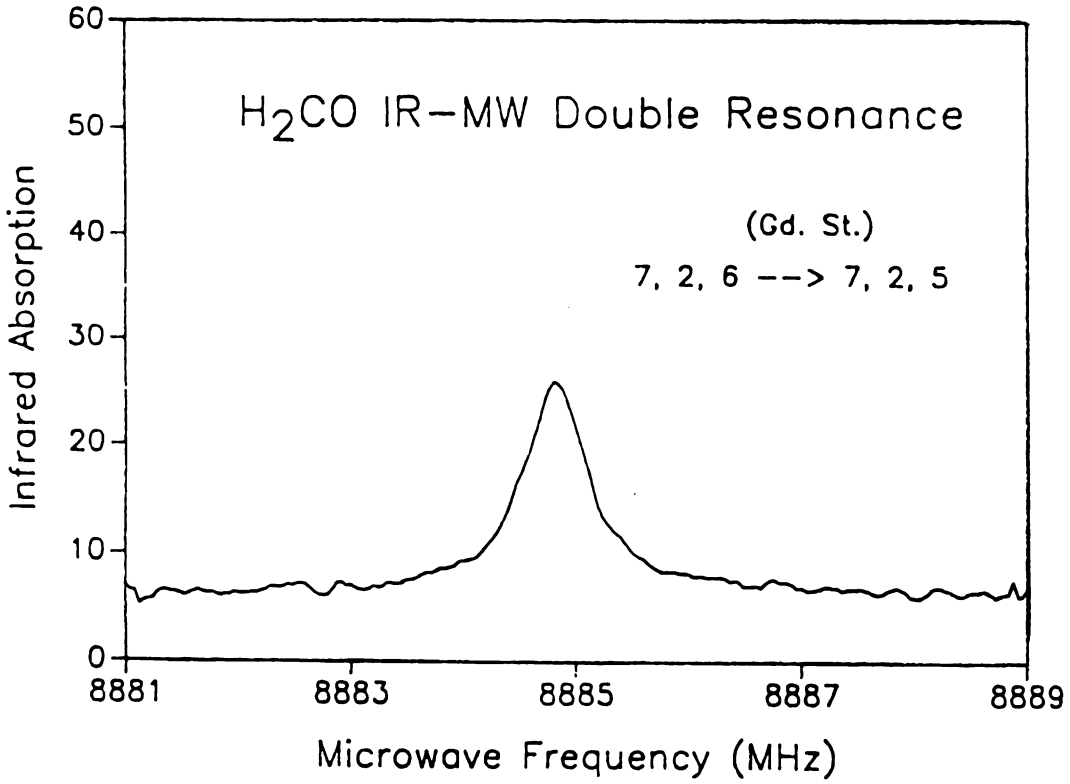

Figure 20. Plot of a ground vibrational state K-type doublet $^{7}_{2,5} \leftarrow {}^{7}_{2,6}$ transition of H_2CO observed by the three level IR-MW double resonance method. The CO sideband laser was used to obtain partial saturation of the ν_2 band transition, $^{8}_{2,6} \leftarrow {}^{7}_{2,5}$, at a pressure of ~7 mTorr; an energy level diagram is shown in Figure 19. In this plot the applied microwave frequency is on the horizontal axis and the IR absorption is on the vertical axis.

Infrared - Microwave Double Resonance

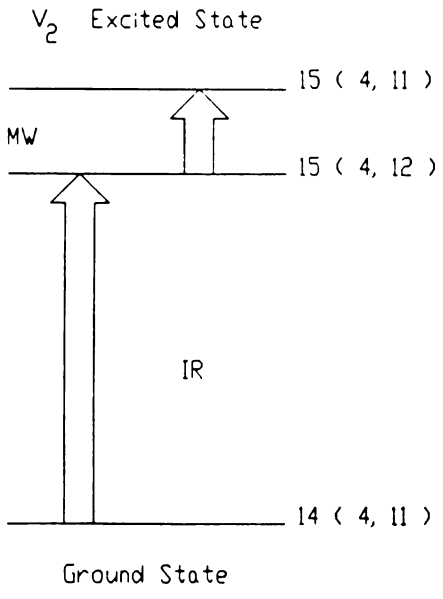

SAMPLE : D_2CO (~ 7mTorr)

VIBRATIONAL BAND : C-O Stretch

ν_2 = 1701.6192 CM^{-1}

CO LASER LINE : C12O16 15->14 P(14)

1729.05659 CM^{-1}

MODULATED MW FREQUENCY : 16,816.5 MHz

SIDEBAND FREQ. : 1729.61753 CM^{-1}

MICROWAVE FREQ. : 9,011.758 MHz

Figure 21. Energy level diagram for the three level IR-MW double resonance measurement shown in Figure 22. The ν_2 band transition, $15_{4,12} \leftarrow 14_{4,11}$, of D_2CO was partially saturated by the tunable CO-MW sideband laser operating in the resonant cavity mode with ν = 1729.61753 cm^{-1}. the microwave transition in the ν_2 = 1 state is observed and is a (c)-type three level double resonance system as defined in Figure 6. The measured frequency for the microwave transition is given.

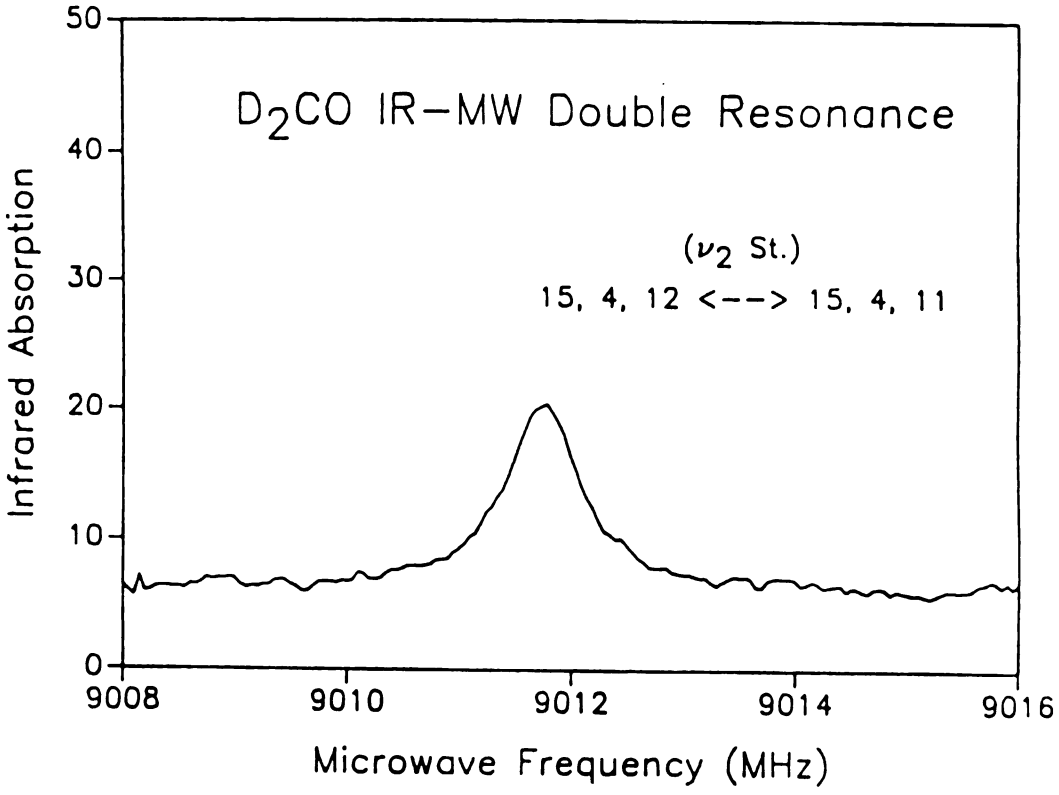

Figure 22. Plot of a ν_2 excited state K-type doublet $15_{4,11} \leftarrow 15_{4,12}$ transition of D_2CO observed by the three level IR-MW double resonance method. The CO sideband laser was used to obtain partial saturation of the ν_2 band transition, $15_{4,12} \leftarrow 14_{4,11}$, at a pressure of ~7 mTorr; an energy level diagram is in Figure 21. In this plot the applied microwave frequency is on the horizontal axis and the IR absorption is on the vertical axis.

value $| N_1^o - N_2^o |$ is only ~500 times smaller than the value $| N_2^o - N_3^o |$, whereas it is 10^5 times smaller in the IR-RF double resonance experiment.

Tables V and VI show a comparison of our measurements with the best calculated frequencies. The ground state rotational structure of H_2CO has been studied extensively by single resonance microwave measurements and the calculated results match our double resonance results within the experimental error. But in the ν_2 excited state for both H_2CO and D_2CO, the double resonance measurements indicate that a systematic double resonance study would lead to improved values of the rotational parameters.

5. Conclusion

The newly-developed CO-MW sideband laser operated in the resonant cavity mode has been sucessfully applied to saturation spectroscopic studies by both IR-MW and IR-RF double resonance experiments. In order to extend this work to Lamb dip measurements, a laser frequency that is stabilized to within several hundred kHz must be available. This difficulty could be overcome by using a laser Stark Lamb dip signal for stabilization [36]. However, lengthy calibration for the absolute frequency and a tedious optical alignment procedure will be required and is still to be worked out in our laboratory.

Table V.

Comparison of Observed and Calculated Infrared Radio Frequency Double Resonance Results for H_2CO

Sample	Infrared[a]	Radio Frequency[b]	Obs./MHz[c]	Calc./MHz[d]	O.-C.[e]
H_2CO	$14_{4,11} \leftarrow 13_{4,10}$	$13_{4,9} - 13_{4,10}(0)$	119.614(2)	119.615	-0.001
	1778.38926	$14_{4,10} - 14_{4,11}(1)$	221.941(5)	221.992	-0.051
H_2CO	$8_{3,5} \leftarrow 7_{3,4}$	$7_{3,4} - 7_{3,5}$ (0)	136.923(1)	136.926	-0.003
	1764.90244	$8_{3,5} - 8_{3,6}$ (1)	308.131(2)	308.120	0.011
H_2CO	$6_{3,4} \leftarrow 6_{3,3}$	$6_{3,3} - 6_{3,4}$ (0)	54.817(1)	54.818	-0.001
	1745.68728	$6_{3,3} - 6_{3,4}$ (1)	56.158(1)	56.133	0.025

a. Quantum numbers are in the form $J_{Ka,Kc}$. Values under the infrared transitions are the infrared wavenumbers in cm^{-1}. The combinations of CO lasers and microwave frequencies used for the three infrared pumping frequencies are as follows: $^{12}C^{18}O$ 11 → 10 P(18), 12648.3 MHz; $^{12}C^{18}O$ 12 → 11 P(15), -15865.5 MHz; $^{12}C^{18}O$ 12 → 11 P(20), -16908.9 MHz.

b. Numbers in parentheses after the radio frequency transitions are the values of v_2.

c. This work. Numbers in parentheses are standard errors in kHz.

d. H_2CO data from Ref. 35.

e. In MHz.

Table VI.

Comparison of Observed and Calculated Infrared Microwave Double Resonance Results for H_2CO & D_2CO

Sample	Infrared[a]	Microwave[b]	Obs./MHz[c]	Calc./MHz[d]	O.-C.[e]
H_2CO	$8_{2,6} \leftarrow 7_{2,5}$ 1765.03364	$7_{2,5} - 7_{2,6}$ (0)	8884.819(3)	8884.831	-0.012
D_2CO	$15_{4,12} \leftarrow 14_{4,11}$ 1729.61753	$15_{4,11} - 15_{4,12}$ (1)	9011.758(8)	9011.850	-0.092

a. Quantum numbers are in the form $J_{Ka,Kc}$. Values under the infrared transitions are the infrared wavenumbers in cm^{-1}. The combinations of CO lasers and microwave frequencies used for the two infrared pumping frequencies are as follows: $^{12}C^{16}O$ 14 → 13 P(11), -12784.5 MHz; $^{12}C^{16}O$ 15 → 14 P(14), 16816.5 MHz.

b. Numbers in parentheses after the microwave transitions are the values of v_2.

c. This work. Numbers in parentheses are standard errors in kHz.

d. H_2CO data from Ref. 35. D_2CO data from Ref. 34.

e. In MHz.

References

1. G. Magerl, W. Schupita, and E. Bonek, IEEE J. Quantum Electron., vol. QE-18, pp. 1214-1220 (1982).

2. S.-C. Hsu, R. H. Schwendeman, and G. Magerl, IEEE J. Quantum Electron., in press.

3. J. W. C. Johns and A. R. W. McKellar, J. Mol. Spectrosc.,vol. 48, pp. 354-371 (1973).

4. T. Oka, K. Takagi, and Y. Morino, J. Mol. Spectrosc., vol. 14, pp. 27-52 (1964).

5. F. Y. Chu, S. M. Freund, J. W. C. Johns, and T. Oka, J. Mol. Spectrosc., vol. 48, pp. 328-335 (1973).

6. E. S. Ebers and H. H. Nielsen, J. Chem. Phys., vol. 5, pp. 822-827 (1937).

7. E. S. Ebers and H. H. Nielsen, J. Chem. Phys. vol. 6, pp. 311-315 (1938).

8. S. Tatematsu, T. Nakagawa, K. Kuchitsu, and J. Overend, Spectrochimica Acta, vol. 30A, pp. 1585-1604 (1974).

9. T. Oka, H. Hirakawa, and K. Shimoda, J. Phys. Soc. Japan, vol. 15, pp. 2265-2273 (1960).

10. K. Takagi and T. Oka, J. Phys. Soc. Japan, vol. 18, pp. 1174-1180 (1963).

11. D. Dangoisse, E. Willemot, and J. Bellet, J. Mol. Spectrosc., vol. 71, pp. 414-429 (1978).

12. K. Nakagawa, R. H. Schwendeman, and J. W. C. Johns, J. Mol. Spectrosc., vol. 122, pp. 462-476 (1987).

13. H.-J. Clar, K. Yamada, F. W. Birss, G. Winnewisser, and H. P. Gush, Canad. J. Phys. 62, 1834-1843 (1984).

14. G. Guelachvili, D. de Villeneuve, R. Farrenq, W. Urban, and J. Verges, J. Mol. Spectrosc., vol. 98, pp. 64-79 (1983).

15. J. K. G. Watson, in "Vibrational Spectra and Structure" (J. R. Durig, Ed.), vol. 6, pp. 1-89, Elsevier, New York/ Amsterdam, (1977).

16. G. Magerl, J. M. Frye, W. A. Kreiner, and T. Oka, Appl. Phys. Lett., vol. 42(8), pp. 656-658 (1983).

17. G. Magerl, W. Schupita, J. M. Frye, W. A. Kriener, and T. Oka, J. Mol. Spectrosc., vol. 107, pp. 72-83 (1984).

18. Y.-T. Chen, J. M. Frye, and T. Oka, J. Opt. Soc. Am. B, vol. 3(7), pp. 935-939 (1986)..

19. F. Scappini, W. A. Kreiner, J. M. Frye, and T. Oka, J. Mol. Spectrosc., vol. 106, pp. 436-440 (1984).

20. L. Jörissen, W. A. Kreiner, Y.-T. Chen, and T. Oka, J. Mol. Spectrosc., vol. 120, pp. 233-235 (1986).

21. C. H. Townes and A. L. Schawlow, "Microwave Spectroscopy", Dover Publications, Inc. (1955)

22. P. Glorieux, E. Arimondo, and T. Oka, J. Phys. Chem., vol. 87, pp. 2133-2141 (1983).

23. P. Glorieux and G. W. Hills, J. Mol. Spectrosc., vol. 70, pp. 459-468 (1978)

24. M. Takami and K. Shimoda, J. Appl. Phys., vol. 12(4), pp. 603-604 (1973).

25. M. Takami and K. Shimoda, J. Appl. Phys., vol. 10, pp. 658 (1971).

26. K. Shimoda and M. Takami, Optics communications, vol. 4(6), 388-391 (1972).

27. M. Takami and K. Shimoda, Japanese J. Appl. Phys., vol. 11(11), pp. 1648-1656 (1972).

28. K. Tanaka, A. Inayoshi, K. Kiima, and T. Tanaka, J. Mol. Spectrosc., vol. 95, pp. 182-193 (1982).

29. T. Oka, in "Frontiers in Laser Spectroscopy", (R. G. Brewer and A. Mooradian, eds.), North-Holland, Amsterdam, (1977).

30. M. Takami, Japanese J. Appl. Phys., vol. 15(6), pp. 1063-1071 (1976).

31. M. Takami, Japanese J. Appl. Phys., vol. 15(10), pp. 1889-1897 (1976).

32. H. Dreizler, W. Schrepp, and R. Schwarz, A. Naturforsch., vol. 34a, pp. 571-574 (1979).

33. M. Rabb, S.-C. Hsu, and R. H. Schwendeman, to be published.

34. S.-C. Hsu, R. H. Schwendeman, and G. Magerl, J. Mol. Spectrosc., in press.

35. J. W. C. Johns, A. R. W. McKellar, and M. Wong, J. Mol. Spectrosc., vol. 96, pp.353-361 (1982).

36. W. H. Weber, J. Opt. Soc. Am. B, vol. 2(5) pp. 829-836 (1985).